Alexander Melischnig, BSc

DC Magnetron Sputtered Metallic Thin Films for High Resolution Scanning Electron Microscopy

MASTER THESIS

for obtaining the academic degree
Diplom-Ingenieur

Master Programme of Technical Physics

Graz University of Technology

Supervisor:
Ao. Univ.-Prof. Dipl.-Ing. Dr.techn. Werner Grogger
Institute of Electron Microscopy and Nanoanalysis

Graz, March 2015

EIDESSTATTLICHE ERKLÄRUNG

AFFIDAVIT

Ich erkläre an Eides statt, dass ich die vorliegende Arbeit selbstständig verfasst, andere als die angegebenen Quellen/Hilfsmittel nicht benutzt, und die den benutzten Quellen wörtlich und inhaltlich entnommenen Stellen als solche kenntlich gemacht habe. Das in TUGRAZonline hochgeladene Textdokument ist mit der vorliegenden Masterarbeit/Diplomarbeit/Dissertation identisch.

I declare that I have authored this thesis independently, that I have not used other than the declared sources/resources, and that I have explicitly indicated all material which has been quoted either literally or by content from the sources used. The text document uploaded to TUGRAZonline is identical to the present master's thesis/diploma thesis/doctoral dissertation.

30.03.2015

Datum / Date

Unterschrift / Signature

ABSTRACT

Scanning electron microscopy (SEM) is of great importance in the field of material characterisation as the interest of structures which have dimensions of several hundreds of nanometres and smaller increases continuously. Up to now the resolution of SEM has been increasing in such an extent that nanoparticles with diameter below 10 nanometres are able to be depicted sharply. As a consequence of such high magnifications the sample has to fulfil special requirements. To make non-conductive samples suitable for an SEM investigation, one opportunity is to coat the surface with a metallic film. There are several methods for doing this kind of preparation - one of the most commonly used techniques is a physical vapour deposition technique, called DC magnetron sputtering.
This master thesis deals with the improvement of such kind of metal films which have to be applicable for High Resolution SEM (i.e. super fine grain structure, continuous film etc.). Therefore the physical process of the sputter coating and also the elementary processes of the formation of thin films were observed to understand the basic deposition physics of this film growth. DC magnetron sputter coaters of Leica Microsystems and also other competitors generate films where micro structures occur which make the usage for HR-SEM impossible. In order to characterise the films, SEM was complemented by other measurement techniques like transmission electron microscopy (TEM) and atomic force microscopy (AFM). Furthermore numerical and image processing tools were evaluated to quantify the quality of the deposited films, like the power spectral density function, the autocorrelation function or the watershed algorithm.
All in all, the findings allowed for a significant improvement of the metal films of different materials making them suitable for HR-SEM. The number of ditches in the films was minimised and the quality of the thin film was quantified for the most used materials.

CONTENTS

Part I

THEORETICAL PART

1 BASICS OF SPUTTERING

Thin films can be generated by several kinds of physical vapour deposition (PVD) techniques. It is useful to understand how thin films are produced to find out which parameters influence the growth or the formation of micro structures. In this case *physical* means that these coating methods use mainly physical processes to evaporate a substrate with the coated material. In contrast, chemical vapour deposition involves mainly chemical reactions to generate films.
PVD has a lot of advantages like a wide range of coating materials, like metals, alloys and even insulators. But the main aspect why PVD is more interesting than other methods for generating thin films is that a slight change of the process parameters can lead to a dramatically changed behaviour of the film like morphological or optical and magnetic properties [4].
Especially the morphology change by variation of the process parameters is the aim topic of this master thesis and has to be discussed in a scientific way. First of all the understanding of the device which generates the film is necessary. The device produced from Leica Microsystems is a DC magnetron sputter coater. Before this slightly more complex method will be described the basics of a conventional sputter coater will be explained more in detail.

1.1 DC SPUTTERING PROCESSES

As the name of the section let already assume, a stationary electromagnetic field is applied between an anode, where the sample can be mounted, and a cathode. The target material, for instance gold or an alloy of gold-palladium, represents the cathode.

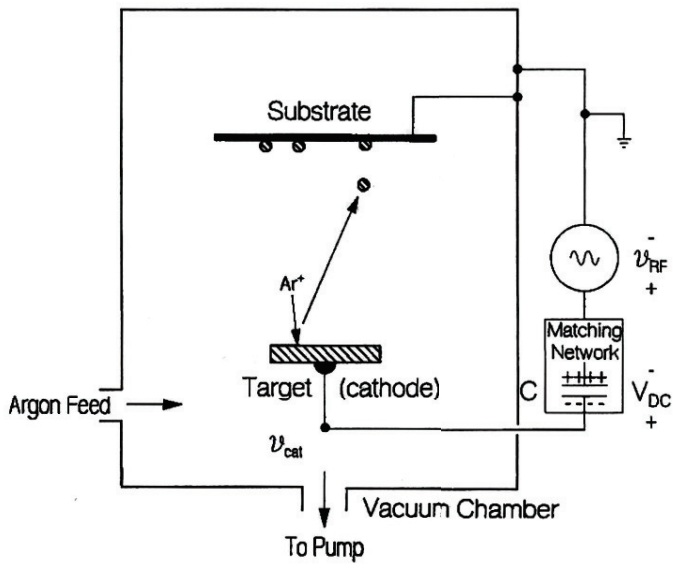

Figure 1: Schematic of a conventional dc sputter coater [16]

The environment around this circuit is well-defined through a chamber in which the pressure can be set to an arbitrary value in a mid-vacuum range ($3 \cdot 10^{-3}$ Pa to $1 \cdot 10^{-1}$ Pa).

Figure 1 shows the schematic arrangement of a conventional DC sputter coater. By funneling an inert gas into the chamber, i.e argon, some already generated Ar^+-ions, which stem from the cosmic radiation, accelerate to the negatively charged cathode and hit the target material. If the kinetic energy of the ion is higher than the binding energy between the atoms inside the solid some target atoms eject from the material with a certain energy distribution and a certain angular distribution, respectively. Apart from ion emission, secondary electrons are ejected too. These negatively charged particles, which are approximately ten thousand times lighter than ions, move to the substrate due to the positive potential.
The neutral target atoms form the film and the electrons with their high kinetic energy heat the substrate on one hand and collide with the atmosphere inside the chamber on the other hand. A collision between secondary electrons with a kinetic energy above the first ionisation energy leads to ionisation of the noble gas. Due to the fact that always more than one secondary electron per target atom ejects from the target leads to an avalanche-like production of Ar^+-ions. The higher the amount of the ions the higher the yield of target atoms and the deposition rate increases. But the likelihood of ionisation of an argon atom is quite small. The ionisation probability depends on the propagation way of the secondary electrons through the argon atmosphere. The way, the electron is able to collide, goes from the cathode where it is generated to the substrate. It is necessary to get a high yield of target atoms to reach the critical deposition rate, where a homogeneous film can be formed. A high yield by a low propagation path of the electrons will just appear, if the number of argon atoms inside the chamber has increased. Then the mean free path of the electrons is short and the ionisation probability rises.
Nevertheless a high ionisation probability by increasing the argon pressure leads to a high collision rate and also a high loss of kinetic energy of the target atoms. Not only electrons have to move to the substrate, the neutral target atoms collide with the argon atmosphere, too. Also the film growth depends on the kinetic energy of the target atoms when they get adsorbed on the surface of the sample.
Companies, which build sputter coaters, offer some changeable parameter to the user interface of their products. This makes it possible to adapt the quality and different properties of the sputtered thin film to the requirements of the sample or the further analysis procedure. But the question is: What is the physical effect behind some parameters? A short summery of the most important parameters should establish clarity:

- The **working distance** describes the distance between substrate and cathode. The higher the distance the higher is the collision rate between target atoms and argon atoms, but also between electrons and argon atoms.

- The strength of the electric field can be varied by the **applied voltage** between target and substrate. Increasing the field strength leads to faster ion projectiles which are accelerated to the target. A higher yield of target atoms will arise. The amount of the kinetic energy is not as much affected as assumed intuitively because the argon atmosphere thermalises the energy of the faster target atoms.
  Goehlich et al. [10] dealt with the subject of energy distribution of the ejected atoms and described the behaviour with the Thompson energy distribution in Equation 1

$$f(E) \propto \frac{E}{(E + E_b)^3} \tag{1}$$

  E is the energy of the ejected atoms in [eV] and E_b defines the surface binding energy in [eV] of the target material. But this formalism is just valid, if the sputtered

atoms get a much smaller energy than the argon ions. The energy distribution is described in Figure 2.
Stuat et al. investigates the energy distribution of sputtered copper atoms by different ion energies of krypton [29]. The detailed description of this process follows in Section 1.2.3. Beforehand, the result is shown in Figure 11. With higher kinetic energy of the projectiles, the number of target atoms with higher kinetic energy increases but the position of the maximum of the energy distribution does not change.

- The **argon pressure** represents a leading parameter for the morphology of the sputtered thin film [27]. It depends on the number of argon atoms inside the chamber. Low argon pressure reduces the collision rate, hence the yield of target atoms decreases and also the kinetic energy per adsorbed target atom falls down through the missing thermalisation process. This parameter influences the size of grains and islands which interacts with the film growth.

- Not only the target atoms are adsorbed on the surface of the substrate. Also residual gases inside the chamber can be adsorbed on the substrate. This leads to built-in impurities in the film. Therefore the **vacuum pressure** before the sputtering process determines the quality and also the electric behaviour of the sputtered film.

- The sputtering rate, which will be discussed in detail at the next chapter, describes the number per time of deposited target atoms on the substrate. But the yield of target atoms depends also on the geometry. Hence, next to the energy distribution an angular distribution of the sputtered atoms occurs. There are some parameters which are changeable to optimise the angle and the homogeneous film growth. These are called **tilt** and **rotation** and can change the angle of the substrate to the target and the rotation speed perpendicular to the substrate plain, respectively.

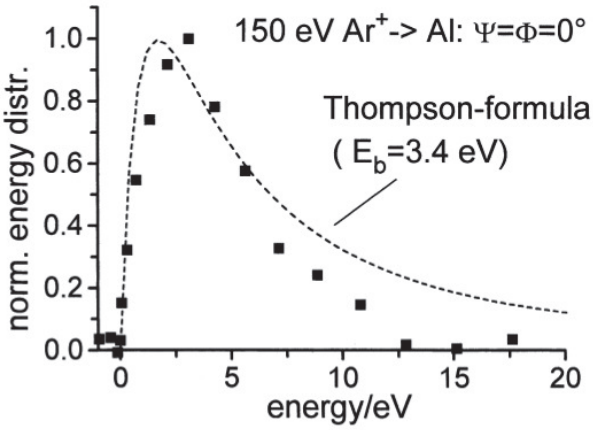

Figure 2: Thompson energy distribution of sputtered Al-atoms [10].

The big disadvantage of an conventional DC sputter coater is obviously the low sputtering rate and also the bombardment of electrons to the sample which leads to a rise of temperature on the substrate. Therefore, a more complex method was invented to remedy these shortcomings, called DC magnetron sputtering. This method is applied in the device LEICA EM ACE 600 which is mainly used during this master thesis to investigate the influence of different parameters on the sputtered film.

1.2 DC MAGNETRON SPUTTERING

The enhancement from the DC sputtering to the DC magnetron sputtering contributes a lot of advantages with regard to the efficiency of producing target atoms and the introduction of temperature into the sample. The main difference is the additional magnetic field surrounding the target.

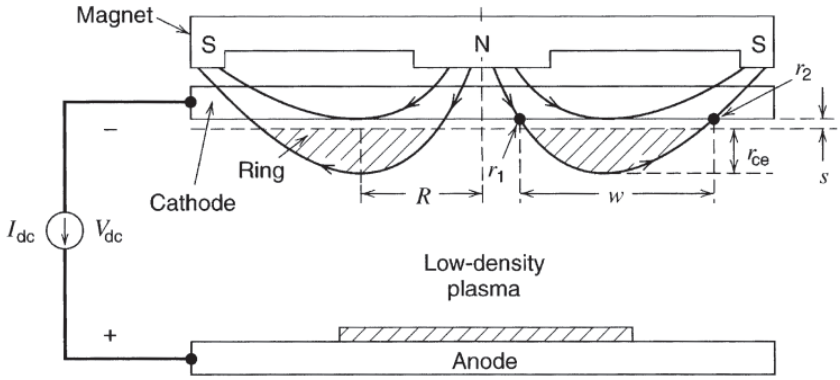

Figure 3: Schematic of DC magnetron sputtering [15]

In most cases the magnetic field is implemented by a permanent magnet which is located behind the target (see Figure 3). The reason why a magnetic field is used is that it traps the produced secondary electrons near the target through the Lorentz force like a magnetic bottle. In this way, the much heavier ions are widely unaffected due to the low field strength. The magnetic field lines form an annularly closed flux of the secondary electrons. In comparison to the section before, the maximum path of the electrons inside a conventional dc sputter coater stretches from the target to the substrate by a very low argon density. The closed circular motion of the electrons with the aim of the magnet field leads to a high enlargement of the propagation path. Thus, the larger the way of the electrons the higher the probability of argon ionisations. Therefore, a lower density of the argon atmosphere lasts to generate enough projectiles for a high sputtering rate. But low density of Ar reduces the scattering events between the argon atmosphere and the produced target atoms. A low number of scattering events carries the disadvantage that the sputtered atoms are more non-uniformly impacted to the substrate, but with higher kinetic energy [15].
On the other side, there are several kinds of DC magnetron sputter coaters. Kelly et al. published an overview article about different kinds of magnetron coaters [14]. The principles are always the same, but there are different arrangements of the magnetic field which have consequences on impacting particels to the sample. Therefore the film growth will be changed. Leica uses a balanced magnetic field between the inner and outer permanent magnets. An unbalanced magnetic field means unclosed field lines between the poles. This affects the ion current to the substrate without biasing. The unclosed field lines lead to extracting electrons from the plasma directed to the substrate. The strength and the formation of the magnetic field lines of the outer permanent magnet varies the ion current.

1.2.1 *Plasma Confinement*

A glow discharge is necessary to emit particles from the target surface. A low gaseous environment decreases the efficiency of particle emission, hence developing a more effi-

cient way to generate target atoms is required. Trapping particles within a plasma ring offer a possibility.
Typical plasma temperatures are about 10000 K and more. This thermal energy leads to delocating the electrons from their atomic cores. Free positively charged ions and free negatively charged electrons interact through the Coulomb force among themselves. The motion of particles can be described by following equation of motion:

$$m\frac{dv}{dt} = q(\vec{E} + \vec{v} \times \vec{B}) + \vec{F}, \tag{2}$$

where m is the mass of the accelerated particle in [kg] which acceleration is $[dv/dt]$ in $\left[m/s^2\right]$. $q\vec{v} \times \vec{B}$ is the Lorentz force, where q is the electrical charge of the particle in $[As]$ and $\vec{B}$ is the necessary magnetic field vector in [T], E is the applied electrical in $[V/m]$ and $\vec{F}$ defines all other external forces in [N]. This mathematical formalism describes the motion of particles within an environment where an electric field and a magnetic field is applied, which is directed perpendicular to the electric field. To get a solution for the velocity out of the equation of motion, a splitting of the velocity into two parts, an electric and a magnetic part, is necessary to get a better illustration of the problem.

- If $\vec{F} = 0$, $\vec{B} = 0$ and $\vec{E} = const.$, where the electrical field lines of $\vec{E}$ are linear and parallel, the particles move along a linear trajectory with the velocity v in $[m/s]$ and their starting velocity (including the direction) $\vec{v_0}$ in $[m/s]$.

  $$\vec{v} = \frac{q}{m}\vec{E} \cdot t + \vec{v_0} \tag{3}$$

- If $\vec{F} = 0$, $\vec{B} = const.$ and $\vec{E} = 0$, where the magnetic field lines of $\vec{B}$ are linear and parallel, the particles are accelerated perpendicular to the direction of $\vec{v}$ and $\vec{B}$ (right-hand rule). And $\vec{v}$ can be written as $\vec{v} = \vec{v_\parallel} + \vec{v_\perp}$ to the direction of the magnetic field lines $\vec{B}$.
  In first approximation, to be able to understand the motion easier, the parallel component of the particle velocity will be set to zero $\vec{v_\parallel} = 0$. The particle moves along a circular trajectory with the gyroradius r_g in $[m]$, or also known as Lamor radius. The centrifugal force and the Lorentz force balance each other.

  $$\vec{r_g} = \frac{mv_\perp}{eB} \tag{4}$$

  How fast particles move within the circle depends just on the type of the particle and not on the velocity $\vec{v_\perp}$. The angular velocity ω_g in $[rad/s]$, or also called Lamor frequency, is defined as

  $$\omega_g = \frac{v_\perp}{r_g} = \frac{e}{m}B \tag{5}$$

  In general, ions move along a bigger gyroradius, but with much slower (smaller ω_g) velocity than a thousand times lighter electrons.

The combination of these two special cases is a motion of a particle with a velocity with a parallel and a perpendicularly directed amount within an applied electrical and magnetic field. This general case leads to an overlap of the particular solutions. The particles move along a circular path perpendicular to $\vec{B}$ with an overlapped linearly translational movement along the direction of the magnetic field. The direction along the magnetic field lines is the same for all particles, but the direction of motion of the gyration depends

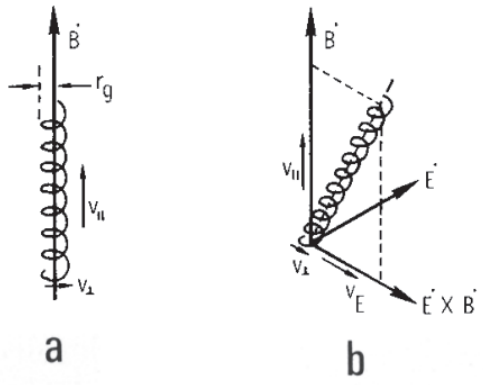

Figure 4: E × B drift leads to a changing of the particle motion [30].

on the sign of the charge carrier. The combination of these two solutions has another consequence on the motion of particles.

The presence of a magnetic field perpendicular to the electric field causes a shift of the gyration orbit. On one hand the circular path changes to a cycloid path and on the other hand a shift of the resulting direction occurs. Figure 4 shows the change of the direction of the resulting velocity. Like the special case before, a magnetic field forces charged particles along a circular path. On one hand the additional electric field slows the particle at the movement against the field lines, and on the other hand it will accelerate the particles during the the motion along the electric field lines. The resulting motion is a cycloid orbit, which is directed perpendicular to the magnetic field and perpendicular to the electric field. An example how an electron moves in this environment is shown in Figure 5.

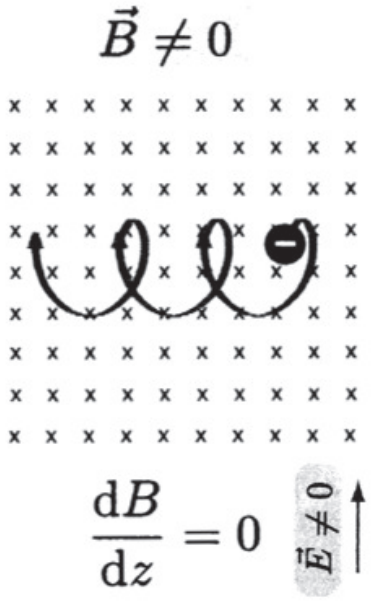

Figure 5: Cycloid orbit by presence of a planar homogeneous magnetic and electric field [22].

But the magnetic arrangement, which has been discussed, is just a simplification of the real configuration of a planar DC magnetron sputter coater. The curved magnetic field lines, which are hinted in Figure 3, differ from the assumption of Figure 5. There two spatial gradients of the magnetic field lines occur, due to the special form of the field, which looks like Figure 6. The $\nabla B_{||}$ and $\nabla B_{\perp}$ change the motion of the particles in a

more complex way. But this changes can also be simplified, if the relative field gradient fulfil the following condition:

$$\frac{|\nabla B|}{B} \ll \frac{1}{r_g} \tag{6}$$

Equation 6 means that the relative field gradient has to be much smaller than the reciprocal gyration radius. If this is the case, the variation of the motion is a change of the radius and an additional drift velocity. Generally, a concretion of the field lines leads

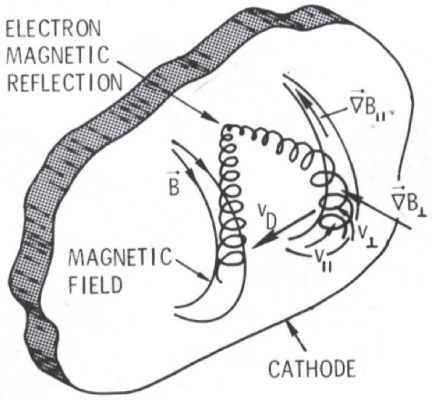

Figure 6: Illustration of a magnetic mirror [30].

to a smaller gyroradius. If the density of the field lines drops it has the opposite effect. If the $\nabla B_{\parallel}$ reaches its maximum and the amount of $\nabla B_{\perp}$ falls down to the minimum a further effect takes into account. The place, where this happens, is at the inner and outer radius of the plasma ring, due to the fact that the magnetic moment of the particles is constant. The particles, which are moved to the inner or outer radius, are reflected. Figure 6 illustrates the effect of a magnetic mirror, which occurs, when the ∇B reaches its maximum. These discussed phenomena leads to trapping of the electrons inside an dc magnetron sputter coater. The $E \times B$ drift is the main reason why a closed plasma ring exists and the theory of a magnetic mirror explains, how electrons are able to be trapped inside a plasma.

1.2.2 *Ejection of Atoms from a Solid*

Now it is already considered how a plasma is formed. The collision inside the plasma with the argon atmosphere in the chamber generates ions. These ions are accelerated to the target, a solid metallic material which acts as donor for the film generating atoms. When particles impinge on matter they interact. Especially for well-defined structures, like a solid, the physics behind these processes can be written in a mathematical formula. G. M. McCracken [20] showed a summary about all relevant interactions between ions and a solid metal in different range of energies of the incident particles in his report. In general, Figure 7 depicts all kinds of relevant interactions.
McCracken [20] also regards the difference between the physical behaviour between bulk and surface states. Thus the mathematical description at surfaces is distinguished from formulas, which can be applied for regular solutions inside the bulk. The bulk consists of infinity bread lattice, even known as periodic boundary conditions. It does not consider any appearance of finite states.
The main difference between surface and bulk relating to the bonding energy of atoms is the missing of at least one neighbour atom. An absent atom reduces the bonding energy

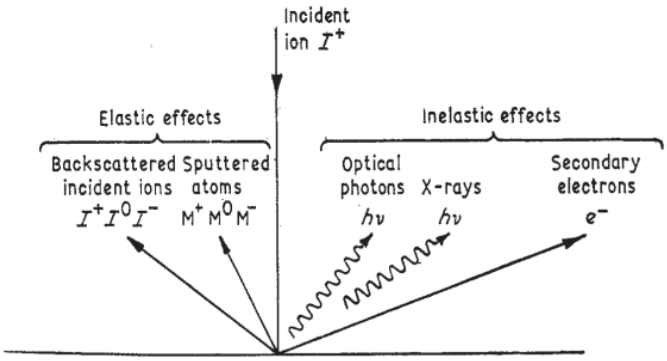

Figure 7: Processes occurring on surfaces. [20]

and leads to a loosely bound surface atom which ejects as easy as an bulk atom. So topography and surface defects of the target material become more important. For this reason, many experimental work and also theoretical work has been done since the early seventies to conclude measurements into a close mathematical formula. McCracken [20] did a lot of experiments, which led to a better physical understanding of the occurred behaviour.

Interactions can be divided into two main parts. Those, which transfer energy, are called inelastic interactions and those interactions where no energy transfer occurs are called elastic interactions. In cases of ionic particles arriving at surfaces, which are generated within the LEICA Sputter Coater, just particles in low energy range around 200 eV are of interest. Therefore, not all showed interactions of Figure 7 are considered. Mainly elastic effects are dominant, but also some inelastic interactions, especially for a magnetron sputter coater, take place. If an ion of the plasma comes near the metallic surface, it has a certain probability that it will be backscattered if it collides with the electron cloud or the lattice atoms, respectively. Due to the collisions the incident ion will decelerate to thermal velocities and gets trapped into the lattice. The amount of electronic collision is high compared to collisions with the lattice atoms and will numerically be defined as a continuous energy loss. In contrast, the amount of nuclear collisions are rare and can be described by two-body collisions, where energy and momentum are conserved. These different types of energy loss lead to different particle emission from the surface. An electronic collision generates excitations and ionisation. At higher energy of the ion, ionisation effects lead to emission from high energetic photons, like x-rays. But this part will be neglected because ion energies of a few hundred electron-volt will just knock out electrons from the outer shell of the lattice atom. No x-ray emission occurs. Photons can be ejected if the collision appears near the surface, otherwise the quasi-particle will be absorbed from another lattice atom. The ejection of photon results from the de-excitation of an excited lattice atom on the surface. As seen in Figure 7, secondary electrons have also left the solid. They are generated in the conduction band of the solid and are emitted directly, if they have sufficient energy. Otherwise they recombine with lattice defects.

For efficient magnetron sputtering the emission of neutral target atoms and secondary electrons are of peculiar interest. In 1960 reports about sputtering theories described the phenomena with theories based on cascades of atomic collision due to kinetic energy of the incident projectiles, like in Figure 8(a). These theories can't be held, since preferential directions of ejection of atoms from single crystals were observed. Late 1969, Sigmund published a theory, which is based on random collision processes too, but he calculated with Boltzmann's equation and general transport theory. As a consequence, the experimental measurement overlaps with Sigmund's theoretical prediction. The effect of eject-

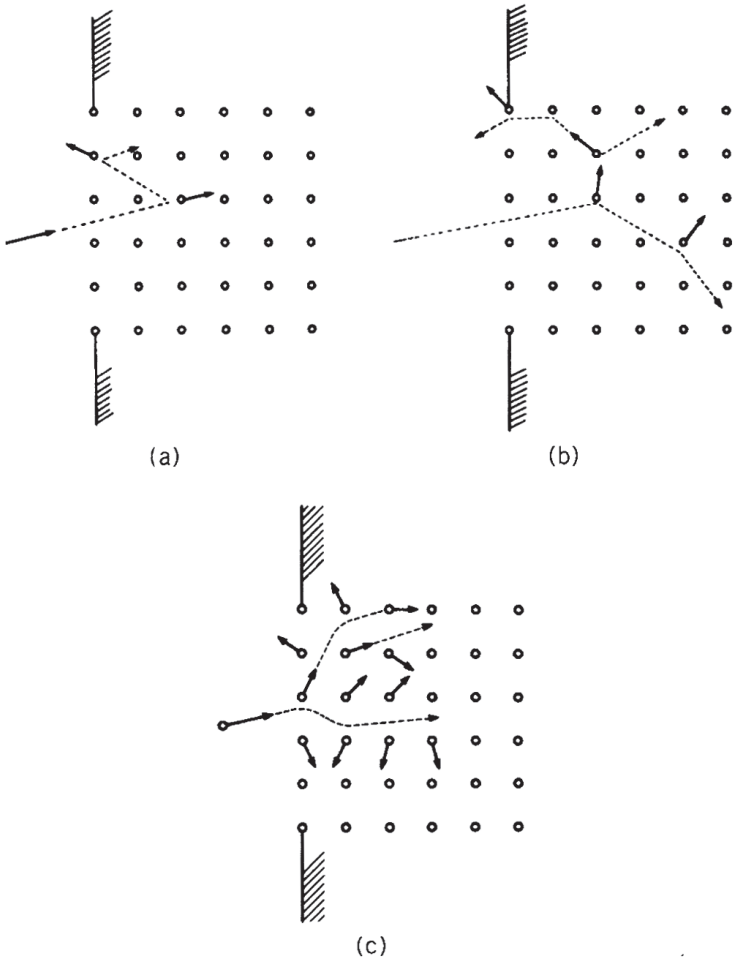

Figure 8: Sigmund's Energy Regimes: (a) single-knockon regime - for slow and low mass ions; (b) linear cascade regime - $S(E)$ according to Equation 7; (c) thermal-spike regime - the high energy regime with evaporation characteristic.

ing target atoms from a solid, called sputtering, occurs according to [20]: *When the energy of the primary ion is sufficient to transfer an energy greater then a displacement energy of a lattice atom, then a collision cascade can be initiated. If this cascade intersects the surface with atoms whose energy is greater then the surface binding energy, then sputtering takes place.*
How much neutral target atoms, which are able to produce metallic thin films, emit of the surface per incident ion is described by the sputtering yield. For low energetic ions (where $E_{ion} = 0.1 - 1$ keV) the quantity depends mainly on the ratio of masses between the incident ion an the lattice atom and their kinetic energy. It can be written as

$$S(E) = \alpha \frac{3}{4\pi^2} \frac{4 m_1 m_2}{(m_1 + m_2)^2} \cdot \frac{E}{U_0}, \tag{7}$$

where m_1 is the atomic mass of the incident particle in $[\text{amu} = 1.6 \cdot 10^{-27}\text{kg}]$, m_2 is the atomic mass of the lattice atom in [amu], α is a dimensionless quantity depending on the ratio $\frac{m_2}{m_1}$ and U_0 is the surface binding energy in [eV].

The formula above is not accurate for light ions which are impinged a target with lattice atoms with high atomic mass. $S(E)$ is quite constant for a mass ratio of $\frac{m_1}{m_2} \approx 1$. The mass dependence of the sputtering yield is shown in Figure 9 and illustrates the above formula of Sigmund. For argon ions with a kinetic energy of 400 eV a periodicity along the transition metal can be observed for the sputtering yield. But sputtering occurs just above a characteristic threshold energy E_{th}. This energy lies between 10 and 30 eV, which

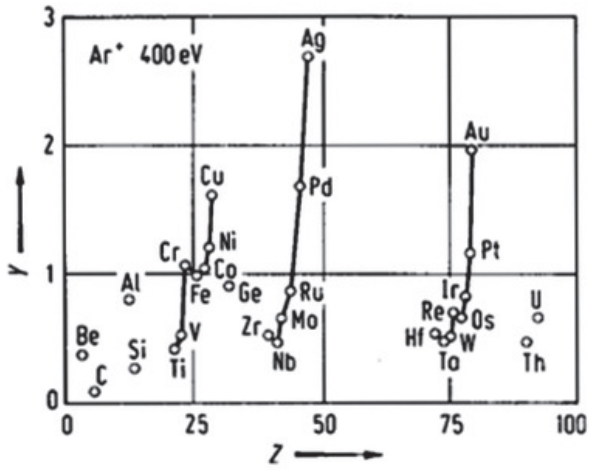

Figure 9: Sputtering Yield by different target materials [5].

depends on the combination of the incident ion and the used target (the ratio of masses). If the incident ion bombardment impinges perpendicularly on the surface, the sputtering yield increases nearly linear, like in Figure 10 (left). If the kinetic energy increases further to about 10 keV, the thermal-spike regime will overcome and implantation effects appear. Implantation means that ions stick deeply in the solid and the whole kinetic energy is transferred to the lattice.
Geometric effects lead to variation of the sputtering yield too. According to [5], it was observed that the yield of target atoms does not reach a maximum when ions bombard a solid perpendicularly to his surface plane. If the angle changes slightly a maximum occurs by about 60 degree, which is shown in Figure 10 (right). The essential change of the direction of the momentum is much smaller at 60 degree and more kinetic energy can be used to eject target atoms. At higher angles the sputtering yield increases again due to the reflexion of the ions at the surface.
In summary, it can be stated that the maximum sputtering yield will get with a mass ratio between ions and target atoms about 1, at an incident angle about 60 degrees and with energies within the linear range between 100 and 1000 eV.

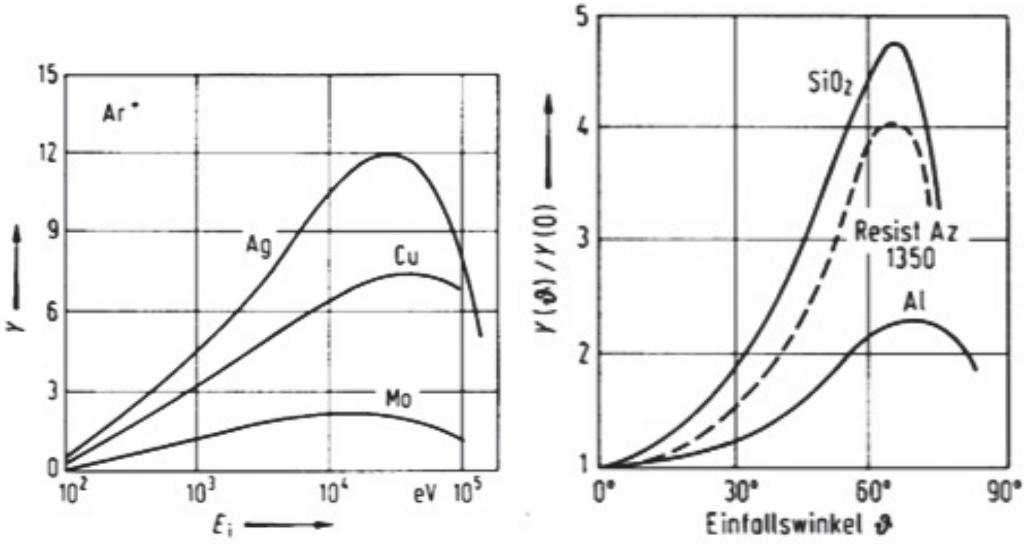

Figure 10: Energy (left) and angle (right) dependence of sputtering yield [5].

1.2.3 *Energy Distribution of Sputtered Atoms*

Sigmund and Thomson [16] deduced a theory, how sputtered atoms emit from a surface of a solid. Especially Sigmund showed that emission of atoms of a single crystal target prefer a certain direction. In most cases, for generating thin films for instance, it is necessary to produce a homogeneous film. Therefore, an ideal sputter coater emits target atoms uniformly over the whole solid angle. This ideal state is just possible, if the emission is randomly distributed at the beginning of the sputtering process. A single crystal cannot fulfil this condition. Today one reason why target material is as much expensive as conventional metal, is the amorphous/polycrystalline state. Complex cooling processes are invented to fabricate such materials. Another important reason for the high costs is certainly the grade of purity. In Section 1.1, where the principle of a sput-

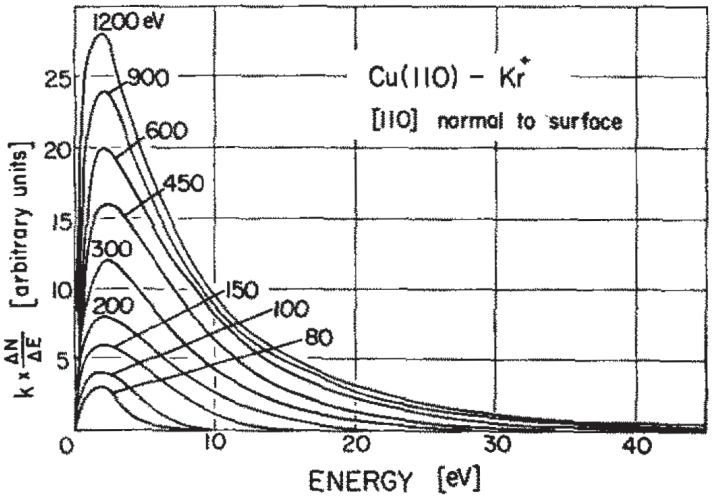

Figure 11: Energy distribution of sputtered Cu-atoms by different ion energies [29].

ter coater is described, a short outline about energy distribution of sputtered atoms is given. It is known that the sputtered atoms follow the Thomson distribution as long as the linear cascade regime is effective. Within this range the relative shape of the energy distribution is independent of the ion energy and the angle which the ions impinge the target surface. The maximum peak (sputtering yield increase during the linear cascade regime) becomes higher, but the value of the energy is still the same, like Figure 11 shows. Stuat and Wehner were concerned with the energy distribution of sputtered atoms from crystalline and also polycrystalline copper surfaces in their report [29]. But at the lower threshold of the energy range deviations of the predicted Thomson distribution are expected. In Figure 11 a lightly shift of the maximum peak towards lower energies can be seen on the graph at an ion energy of 80 eV. Goehlich et al. observed also a steeper fall-off of the energy distribution and an angular dependence and reports about the results in [10].

By using a magnetron sputter coater both regimes are of interest depending on the parameter for the voltage and on the chamber atmosphere. On one hand a high argon pressure leads to many projectiles but on the other hand it slows the ions and also their kinetic energy for the impinge at the target surface. If the linear cascade regime is abandoned it has a bearing on the thin film growth due to the changed sputter rate.

1.2.4 *Secondary Electron Emission*

Mainly elastic interactions between ions and surface were discussed. An important role plays the emission of secondary electrons as consequence for inelastic interactions. The emission of secondary electrons is a theoretically understood effect and it applies in many analytically scientific devices, like in the scanning electron microscopy. The total yield of electrons per incident ion γ is proportional to the continuous energy loss of the incoming ions and is independent from the used target material.

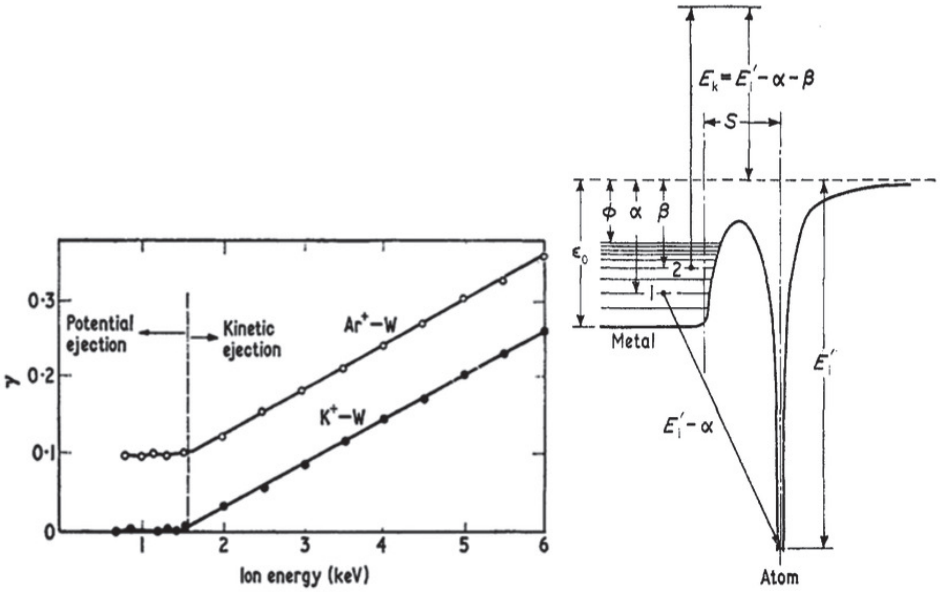

Figure 12: Yield of secondary electron emission [20] (left). And on the right the Banddiagram of the Auger neutralisation by emission of a secondary electron [20]. Where φ is the work function, ε_0 is the Fermi energy, α is the energy level of the tunnelled electron, β the energy level of the Auger electron and E_1' the ionisation potential of the ion modified by the surface.

Figure 12 (left) depicts γ respect to the kinetic energy of the incident ion by two different types of ions. The energies extend over ranges of several keV. It can also be seen that there will be two kinds of ejections. The potential ejection, which applies just in the low energy range, and the kinetic ejection, which rises linearly for both argon and krypton ions. The slope of the kinetic part is always the same for all metallic materials, just the y interception of the linear function varies.
This shift towards the y-axis is explainable with neutralisation effects of the incoming ion. If the neutralised ion is in the ground state no potential emission occurs and therefore $\gamma = 0$ at low energies. Till a certain threshold energy is reached, the emission of secondary electrons starts and increases linearly. The neutralisation is mainly caused by Auger neutralisation. An electron from the Fermi gas inside the metal tunnels through the potential barrier and fills the missing place of the incoming ion shell to form a neutral atom, see Figure 12 (right). The remaining energy of the electron releases and transfers to an electron of the Fermi gas. This energy is sufficient to emit this electron as secondary electron.
The energy [20] which gets the released electron is then given by

$$E_k = E_1' - \alpha - \beta. \tag{8}$$

Secondary electrons release the surface with a few eV and will accelerate towards the plasma ring inside the sputter coater , which needs the electrons to produce as much

ion projectiles as possible due to collisions with electrons. This process enhances the ion bombardment and therefore the sputtering yield increases dramatically.

1.2.5 *Thermalisation*

Afterwards a significant amount of sputtered neutral atoms has been ejected from the target by a constant environmental atmosphere, argon for instance. The atoms fly through the chamber towards the substrate through this atmosphere and collide with the argon gas. The atoms loose kinetic energy continuously, till they arrive at the substrate. Meyer et al. calculated a model, how this energy loss occurs by the thermalisation process in [21]. Especially they are considered with the energy distribution on the substrate by sputtering niobium and copper in low energy regime.
They started with particles which follow the Thompson distribution as the initial energy distribution. These particles are able to interact with the argon sputtering gas, which is Maxwell-Boltzmann distributed inside the chamber. Main parameters for the energy loss are the distance between target and substrate, called working distance, and the sputtering gas pressure, which determines the atmosphere. Meyer [21] found an expression, of which behaviour is in good agreement with experimental results and is given by

$$E_F = (E_0 - k_B T_G) \cdot \exp\left[n \ln\left(\frac{E_f}{E_i}\right)\right] + k_B T_G, \tag{9}$$

where E_0 is the initial energy of the sputtered atoms in [eV], T_G is the sputtering gas temperature in [K], $\frac{E_f}{E_i}$ is the ratio of energies before and after a collision and n is the number of collisions.
The number of collisions [21] is expressed by

$$n = \frac{d \cdot p \cdot \sigma}{k_B T_G}, \tag{10}$$

where d is the distance in [m], p is the sputtering gas pressure in [Pa] and σ the collision cross section in $\left[m^2\right]$ (assumption of hard core interaction) and k_B is the Boltzmann factor in [J/K]. With the formula of Equation 9 a discrete evolution of the energy distribution can be calculated by various working distances and various pressure settings. The results of Meyer are shown in Figure 13.

The evolution of the energy distribution shows that a small change of distances at macroscopic dimensions leads to a rough change of the energy distribution, which implies a large change at microscopic dimensions. A complete thermalisation of copper and niobium atoms is fulfilled at about $d = 20\,\text{cm}$. This means that the sputtered atoms near the substrate adopt the Maxwell-Boltzmann distribution from the surrounding atmosphere. Graphs between $d = 0\,\text{cm}$ and $d = 20\,\text{cm}$ depict a sharp cut-off at certain energies, which changes continuously to smaller energy values. So, the initial high-energy tail transforms to a cut-off drastically. Just slow particles impinge the sample after an collision-full way to the substrate.

1.2.6 *Surface Damaging Effects*

For sure, ejection of atoms causes a damage of surfaces of a target material. The topography of a target in its ideal state should be planar and totally free of dislocations and vacancies. As a consequence, deviations from this state lead to different sputtering parameters and a strongly angular dependency of the incident ions.

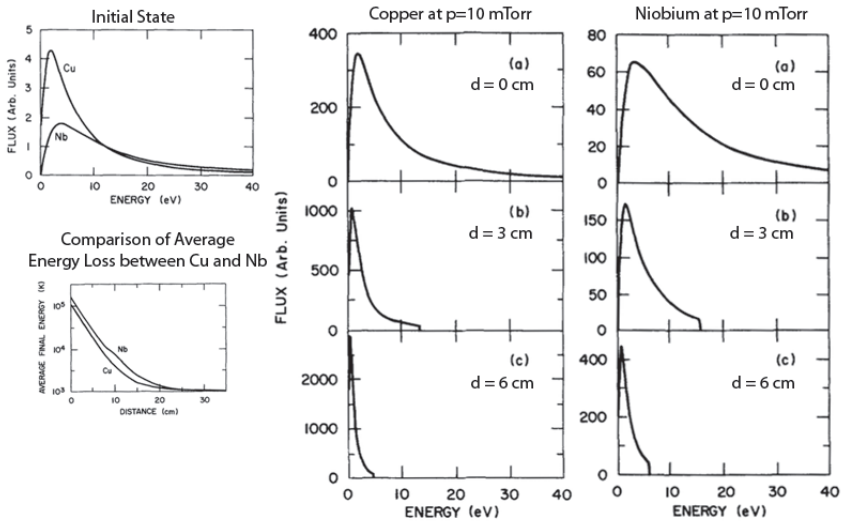

Figure 13: Energy distributions before (left upper corner) and after thermalisation by various distances between target and substrate [21].

By generating low energy projectiles the transferred momentum is quite small in comparison to high energetic particles. Due to this fact the change of topography is also relatively little, but non-zero. The sputtering coefficient S, which is just proportional to the ratio of masses along the linear cascade regime, gets to an angular dependent quantity $S = S(\theta)$. Hence, the rate of erosion is then given by

$$R = \phi \cdot n \cos\theta \cdot S(\theta), \tag{11}$$

where ϕ is the incident flux density and n is the atomic density of the surface.
Typically no material is really totally free of impurities, therefore it always exists a small amount of angular dependence and deviation of the theoretically calculated sputtering coefficient, but at the low energy regime about a few hundreds of eV those effects keep within limits. According to this approach it will be marked that surface damaging effects leads to deviation of the sputtering coefficient. This will be neglected because the quantity is too small to quantify it experimentally.

2

BASICS OF THIN FILM GROWTH

Sputtered atoms fly toward a substrate, where they transfer their whole kinetic energy to the surface. At certain environmental or certain surface conditions many of these atoms stick at the surface. They are now called *adatoms*. The term adatom means a bounded particle on a surface through adsorption effects. In some letters you will read monomers instead of adatoms. This means still the same, but comes from the idea that monomers form the smallest basis of a whole film. These kinds of particles interact with the surface of the substrate naturally. Historically E. Bauer was a German physicist and a pioneer for the theoretical understanding of film growth and published his theory in [2] . In the first assumption the problem was described by macroscopic quantities like surface energy σ inspired by the surface tension, like a droplet falling on a substrate. Atoms or molecules interact with themselves, with the substrate and the interface between atoms and substrate. This energy transfer is summarised by their specific surface energies and can be written as:

$$\Delta = \sigma_{adatoms} + \sigma_{interface} - \sigma_{substrate} \tag{12}$$

Depending on whether the sign of Δ is positive or negative, the growth and therefore the morphology becomes different and several growth modes can be observed. Assuming Δ

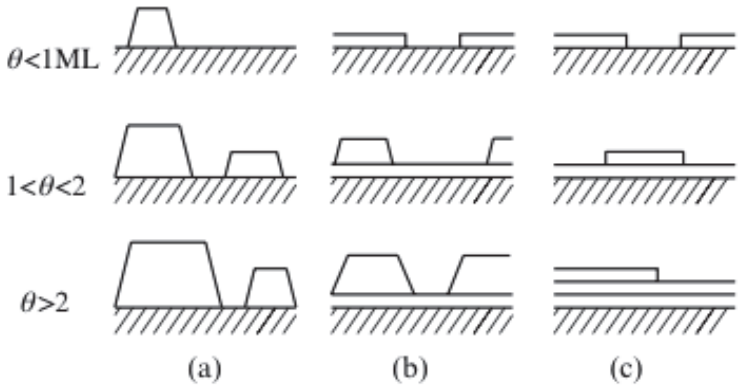

Figure 14: Three growth modes as function of coverage θ [32]: (a) Volmer-Weber mode; (b) Stranski-Krastanov mode; (c) Frank-van der Merwe mode

becomes zero or negative, on one hand it is possible that a layer by layer growth, also called Frank-van der Merwe (FM) growth, appears and on the the other hand a layer and island growth, called Stranski-Krastanov (SK) growth, grows. At both modes a full wetting of the substrate follows. At FM growth the first monolayer wets the substrate as the interaction between substrate and film is stronger than the interaction between the adatoms. $\sigma_{substrate}$ is the dominant part of the whole energy term. The difference between FM and SK is that the surface energy term of the substrate is quite lower and therefore every new grown monolayer screens the range of the interaction of the substrate. If $\sigma_{substrate}$ becomes smaller, the surface energy of the interface dominates the energy transfer and islands rise up. That is still the same like a water droplet on a rough surface, the surface energy of the interface is too high for wetting the substrate. The surface tension of the water droplet will minimise and a sphere is formed. In nature the

lotus flower uses this effect to clear its leafs by the so called lotus effect.
The third growth mode is the Volmer-Weber (VM) growth. No complete wetting of the substrate can be observed and just islands rise up. VM growth appears, if the $\sigma_{substrate}$ is not really existing and $\sigma_{interface}$ dominates the energy transfer from the beginning of the growth. Figure 14 shows the described film growth modes schematically based on Bauer's theory.
If the material of substrate and sputtered atoms differs, many kinds of additional effects occur, which are not regarded in the strongly simplified theory of Bauer. There are several diffusion processes, which arise between adatoms and substrate and are also lateral to the substrate plane. However, a macroscopic view of film growth is not enough to understand the whole physic behind. An atomistic point of view is used by the kinetic gas theory and the resulting rate equation which leads to a bit more realistic conditions for predicting film growth on different behaviour of the sputtered atoms and the properties of the substrate.

2.1 ATOMISTIC ELEMENTARY PROCESSES DURING FILM GROWTH

Bauer [2] recognised that the film growth depends on the sticking adatom at the beginning of the sputter processes. These adatoms are near the surface and interact strongly with the substrate. The later the evolution of the film the lower is the influence of the substrate. This makes it clear that the change of the growth mode lies at the early stage of the film formation. But the macroscopic quantities cannot describe processes on atomic dimensions.

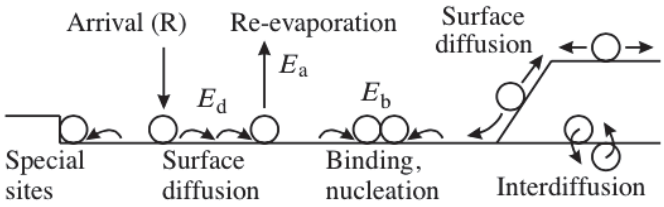

Figure 15: Most important surface processes and characteristic energies in nucleation and film growth [32].

Therefore, Venables [32] dealt especially with the diffusion processes at the beginning situation of sputtered atoms impinging on the substrate. Figure 15 summarises the most important processes. The main difference of Bauer's and Venable's [32] theory is that Bauer assumed that the sputter processes occur mainly in thermodynamic equilibrium. But it was shown that this assumption is wrong, because sputtered atoms arrive at the surface far away from thermal equilibrium almost entirely. Thus, a lot of kinetic effects appear which have to be considered in a closed mathematical theory.
Venables [32] used the kinetic gas theory to express the rate equation which describes the amount of sputtered atoms after the thermalisation process through the chamber atmosphere. This represents the first atomic process - arrival of a sputtered atom on the surface. Near the surface the incident atom interacts with surface atoms. The atoms feel a potential on every randomly arrived position, but they seek being in a local minimum around the impinged position. The kinetic energy of the particle transfers to the lattice of the substrate by a few jumps from site to site. If the kinetic energy of the moving atom is too low to jump to the next side, it gets bonded on the surface. The process of bonding an atom at the surface is called adsorption. E_a the adsorption energy is about a few eV $\approx 1-2$ eV.

The energy transfer from the atom to the substrate is another atomic process. But if the threshold energy is transferred, it does not mean that the atom sticks rigid on its last position. The adatom gets thermal energy of the solid by the phonons to leave the current position and is able to move easily a few steps. This behaviour is described by the mobility.

The most important process is the lateral surface diffusion. The diffusion along the substrate plane is responsible for many followup effects like nucleation, grain size, etc. This diffusion depends on the mobility of the adatoms on the surface. An atomic quantity describing the mobility is the diffusion coefficent D, which is based on the remained kinetic energy of the adatom and the temperature of the substrate. The way how the atom jumps from lattice site to lattice site can be seen theoretically as random walk. The distance between starting point and end point is the effective waylength l in [m]. l is given by the Einstein's relation [32]

$$l = \sqrt{D\tau} \tag{13}$$

where D describes the diffusion coefficient in $\left[m^2/s\right]$ and τ the time for a jumping event in [s]. And D is defined as

$$D = a^2 \nu_0 \cdot \exp\left(-\frac{E_d}{k_B T_S}\right) \tag{14}$$

where a is the lattice constant in [m], ν_0 is the amplitude of the diffusion frequency in [1/s], E_d is the diffusion energy in [eV] and T_S is the substrate temperature in [K]. The probability to leave the bonded state of an atom is low, but still there. The so called desorption process appears for single loosely bound adatoms. The desorption energy is the same as the adsorption energy, but with opposite sign. Thus, the transferred energy from the phonon reservoir of the lattice suffices that the adatom leaves the surface and becomes a free atom again. The probability for doing this kind of atomic process drops if more adatoms come close together to form a grain.

2.2 FURTHER EFFECTS BASED ON ATOMISTIC PROCESSES

The discussed processes lead to different growth modes, depending on which single process is dominant. There are two main effects which can occur, if some behaviour of the substrate or the impinged atom will be changed.

2.2.1 *Condensation*

In general, the condensation effect describes the sticking probability on the substrate. It mainly depends on the substrate temperature and can be divided into two regimes - the complete condensation and the incomplete condensation regime. To differ which regime is accurate, there is a ratio defined by $r = \frac{\tau_{des}}{\tau_d}$. This indicates the complete condensation if, $r > 1$, and otherwise the incomplete condensation, if $r < 1$. This ratio compares the different time-scales. That is the duration which atoms need to desorb and need to stick rigidly on the substrate, respectively.
Complete condensation appears at very low substrate temperature or at very high deposition rate. In this case τ_{des} is small and τ_d grows rapidly. That means that the probability of desorption is quite low because it needs as much steps as τ_{des} is over. At this time the likelihood of capturing an another atom is much bigger and the adatom is bonded on the surface. The material which forms the films rises nearly linear.

An incomplete condensation describes a regime at very high substrate temperature, where the desorption probability is not quite low. This means that every atom which arrives at the surface condenses immediately. Therefore τ_{des} has a high value and τ_d is quite low.
A single regime does not have to persist during the whole sputter process. It is also possible to begin with an incomplete condensation, which changes into the complete condensation after a certain time. And the time-scales vary during the process, too. Thus, after the transition to complete condensation an equilibrium state between both time-scales will appear. Afterwards the desorption and adsorption balance each other and another effect begins to build up the thin film.

2.2.2 *Nucleation*

If a balance exists between adsorption rate and desorption rate, a critical point is reached. A thin film growth begins when the adsorption effect prevails. At the atomistic point of view nucleation takes place at that point. Nucleation means that more than one adatom forms a bond by movement of the adatom along the substrate. These groups of adatoms are called grains. A grain is energetically more favourable than a single adatom. But a certain probability persists that a adatom of the grain desorbs again.

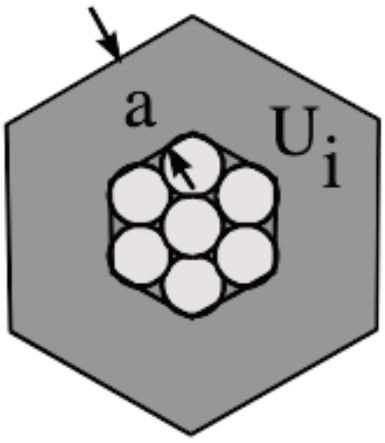

Figure 16: Grain with surrounding capture zone [5].

Whether an adatom leaves the grain or not depends on the size of the grain. The bigger the grain size, the smaller the amount of desorption. The reason for that is a certain grain radius, the bonds inside the aggregate are too strong to let an atom fly away. The grain grows further. The transition size between a stable and an unstable grain is called critical size of a grain, or it is simply called critical grain. The grain which size is lower and therefore the desorption is non zero, is called under critical grain and vice versa over critical grain.
A grain consisting of some adatoms grows further favourably and therefore it needs more and more atoms. There are two mechanisms to get these atoms. The first one is that the sputtered atoms are adsorbed at the grain directly. But there has to be a high sputtering yield for dominating this mechanism. Another possibility to catch atoms is given by diffusion processes. Adatoms around the grain move to the grouped atoms favourably.
Figure 16 shows a group of adatoms (light grey). Around the group there is a dark grey area which is called capture zone with width a which is typically the size of one

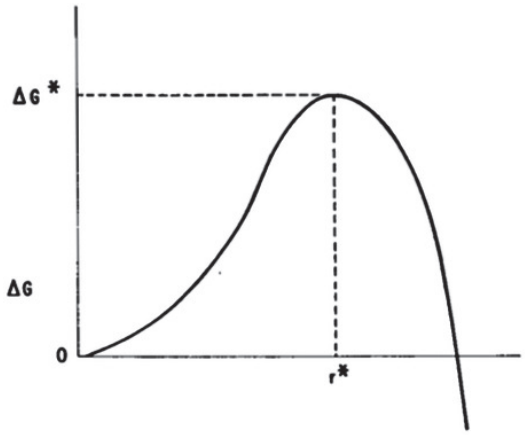

Figure 17: Free energy vs. grain radius (droplet model) to estimate r^* [5].

lattice constant. It is a depletion region where no adatom can be observed, because all atoms within this region are caught by the grain.
How big the critical radius is, depends on several quantities. There are two models, which describe the nucleation phenomena, the droplet model and the particle model. They estimate the critical radius by the free energy ΔG. The exact formula is not as important as the resulting graph of ΔG versus the radius which is shown in Figure 17. As it can be seen, the critical radius lies at the maximum of ΔG and represents the minimal stability size of a grain. For $r > r^*$ the free energy falls rapidly. Over critical grains are the basis for growing a film. Therefore the number of critical grains can play an important role for growing a film with certain properties. The rate of forming a grain [5] is roughly given by

$$I = U_i \cdot a \cdot n_i \cdot n_1 \cdot \nu_d, \tag{15}$$

where U_i is the circumstance of the critical grain which consists of i atoms in [m], a is the width of the capture zone (typically one lattice constant) in [m], n_1 is the number of a single adatom which is not already nucleated, n_i is a grain including i atoms and ν_d is the hopping frequency of the diffusion process in [1/s].

2.3 FILM GROWTH

Now the single atomistic processes and effects were considered. The resulting film growth involves all discussed phenomena during the different growth processes. The morphology differs from every stadium of the film growth and can help to indicate the current step. The desirable end stadium of a continuous film is often the aim of some applications.

Figure 18 shows the single states which passed through. The time of being in a certain state depends on a lot of parameters, but the most important ones are the adsorption rate, substrate temperature and of course the type of substrate. The first state where the film growth begins is the creation of grains. Depending on the above parameter a single grain can include at least one single adatom. But in general, if the mean diffusion way l is long enough more than one atom forms a grain by nucleation effects.
If the grain is formed and the sputtering yield is quite constant the grain grows till it reaches the critical radius where it is stable. A stable grain can also be grown further but after a certain time a equilibrium number of grains including the volume of the capture zone covers the whole substrate.

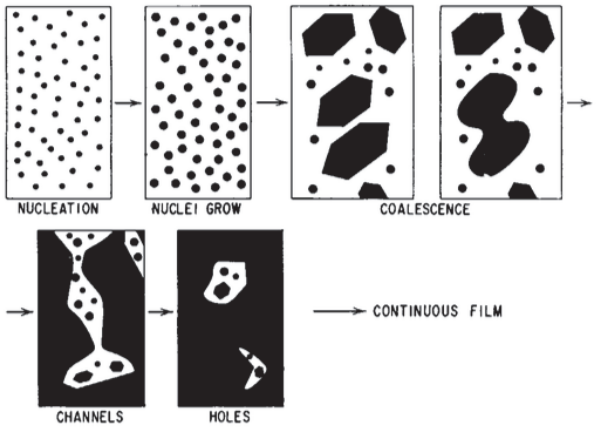

Figure 18: All stadiums which are passing through the way from adsorption of an single atom to the continuous film [5].

Diffusion processes never stop excepting at really cold temperatures. It is possible to move whole groups of atoms along the substrate plane to form bigger clusters consisting of more than one grain. The hopping frequency of whole grains is still lower than a single atom, but it is non-zero. This state is the third stadium of the film growth and the phenomena, where grains bond favourably together, is called coalescence.

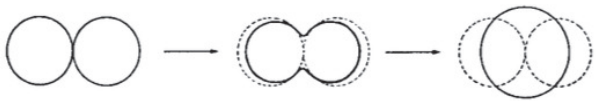

Figure 19: Connecting of two grains to reduce the surface tension [5].

Coalescence is a similar process as nucleation but at bigger dimensions. It is not an atomistic process and can be described with surface tension without great simplifications of the physics behind. Figure 19 depicts the effect in detail and visualises, that two single grains need more coverage area than a newly formed grain with a greater radius. But the newly formed grain needs less space than the sum of two single grains. Thus, bonding and forming of aggregates of more than one grain is energetically more favourable.
At the time, more and more grains form aggregates, or so called islands. Islands in turn prefer to coalescent again. As written before nucleation is a similar effect to coalescence and therefore similar behaviours are expected at greater dimensions. This means that forming of aggregates evokes a depletion zone of grains around the island.
At these positions, which have become available after the coalescence, new sputtered atoms get adsorbed and they are also able to form new grains again. This process is called secondary nucleation.
Then islands are also able to diffuse and connect to another islands, which represent the nearly last step before a continuous film grows together. But before a certain amount of stress causes formations of channels and holes occasionally. The last step will be the filling of these holes and channels by the grains which grow further by the secondary nucleation effect. Now if this is done, a continuous film covers the whole substrate.

2.4 INFLUENCE OF THE SUBSTRATE

The adatom arrangement of the first mono layer depends strongly on the substrate. If the substrate is an ideal crystal, the interaction differs from a real crystal where surface defects (e.g. dislocations, impurities, steps, etc.) are available. Single atoms and grains

collect themselves on defects preferably. [32]
Which kind of single crystal is used, plays also an important role. If the sputtered atom and the substrate is from the same material, the lattice constant is still the same at the interface and along the thin film, too. But if the lattice constant of both materials differs very strong, a misfit arises. The sputtered thin film asserts its own lattice constant excepting the interface between substrate and thin film. This misfit leads to built-in defects which affect the resulting morphology.
If a film grows on the same material the growth is called homoepitaxy. For different materials, the growth mode is called heteroepitaxy. If the substrate is not a crystal the behaviour of film growth changes slightly. An example of a substrate without crystal structure is amorphous glass like SiO. Many biological materials have not any certain crystal structure, therefore it is important to know how a thin film changes the properties if the substrate is amorphous.
Whether homoepitaxy or heteroepitaxy the crystal orientation of the substrate is forced on the film. If the substrate has no orientation the film grows polycrystalline - without preferred orientation. But Smith et al. showed in their report [28] that if a crystalline grid is embedded into an amorphous SiO substrate the film undertakes the orientation of the grid. That means that both situation are possible, but in general a amorphous substrate does not make out certain crystalline orientation - a polycrystalline thin film grows.

2.5 MEASUREMENT METHODS FOR CHARACTERISATION OF METALLIC THIN FILMS

As written in the motivation statement, the ideal thin film for high resolution scanning electron microscopy has to fulfil several requirements. Three common methods were used to investigate all important changes of the thin films until the best solution was found.

2.5.1 *High Resolution Scanning Electron Microscopy*

The metallic thin film is mainly used for SEM, therefore the simplest way for checking, if the properties of the sputtered films are good enough, is the device itself. This method takes advantage of analysing more than one property at the same time. It can especially be performed in a really short time without costly and time-consuming preparation techniques.
Two properties play an important role for the quality of the thin film and the further usability - conductivity (or the opposite is called resistivity) and the morphology of the surface.
The device ZEISS ULTRA 55 is a High Resolution-SEM which is used with the GEMINI In-lens SE detector at very low acceleration voltage U_B around 3 kV. The In-lens detector with low U_B and a very small working distance $WD \approx 2-3\,\mathrm{mm}$ detects secondary electrons of type SE1, which lead to the best resolutions, from a few-nanometres-deep area. The resulting signal generates an image of the surface with such a high resolution that the own structure of the film can be depicted. The device is specified by Zeiss with resolutions of 1.0 nm@15 kV, 1.7 nm@1 kV and 4.0 nm@0.1 kV (featured with a Thermal Field Emission Gun (FEG), stability $> 0.2\,\%$).
The conductivity of the surface can be visualised in the SEM image qualitatively. If the image brightness becomes much greater by the same electron current, the conductivity gets worse. A bad conductivity is distinguished also through bright areas induced by the electron beam. More detailed information can be found in [11].

2.5.2 *Atomic Force Microscopy*

Another method which characterises the surface quality of thin films is Atomic Force Microscopy (AFM). SEM leads to good results for films with high structures and a high surface topography. But it reaches its limits for smooth films with less topography. Therefore, AFM offers an alternative way to characterise the topography without electron induced charging effects. The attractive or repulsive atomic forces of the atoms is used, which form the film. Therefore, higher resolution can be reached. These forces are detected with a needle tip by scanning the surface of the sample and recognising the displacement of the tip along the z axis. An image of the z values which are dedicated to a colour value of each position of the tip, represents the surface quality. With further software tools, grain sizes and grain heights can be determined.
The used device is the AFM Bruker Dimension Fastscan Bio, which resolution depends on the used type of needle tip. As the name let already assume, the measurement time is decreased very strong to make it possible to observe structure changes in nearly real-time (3 frames per seconds). Besides the fast scan rate, the microscope reaches high resolution by using the Fastscan C needles. The tip which shape is rotational symmetric and triangular and it consists of silicon nitride. The radius of one single tip is 5 nm. More detailed information can be found in [8].

2.5.3 *Transmission Electron Microscopy*

By using Transmission Electron Microscopy thin films can be analysed at highest resolutions, higher then AFM or SEM. But there is a not negligible disadvantage - this method is time-consuming during the measurement and also the preparation techniques are challenging.
Analysis with TEM leads to information about the chemical composition, the morphology and crystallographic structure. The charging effect is quite low through high electron energy and the preparation technique. Samples which are analysed within the TEM must be electron transparent (i.e. 100 nm or less).
In addition, it is also possible to get more information about the crystallographic structure by using electron diffraction.
A thickness distribution is estimated by the $\frac{t}{\lambda}$ parameter. This parameter defines the change of the intensity of the electron beam through the sample in comparison to the zero loss peak, which is the measured intensity of the elastic contribution. The absolute thickness value is a really rough estimation, but the relative thickness distribution along the sample plane leads to a good overview of the uniformity of sputtered thin film.
The used device is the FEI Tecnai 20, which maximum acceleration voltage is 200 kV. The electrons are generated by a Schottky Field Emitter including a monochromator unit. The reachable point resolution is 0.24 nm specified by FEI. More detailed information about TEM can be found in [34].

Part II

EXPERIMENTAL PART

3

DETAILED MOTIVATION

As written in the short abstract in the introduction, micro structures of sputtered metallic thin films can be observed which influence the imaging quality of a High Resolution SEM negatively.
The Institute of Electron Microscopy and Nanoanalysis at the Graz University of Technologies used a RF sputter coater for sputtering non-conductive samples with a metallic film. A considerable disadvantage of this method to get a conductive layer is a high temperature impact due to the missing magnetic field. The influence of the magnetic field is described in Chapter Section 1.1 precisely, which is a good way of making the evaporation process more efficient, but the most important point is that the magnetic field traps the electrons. The generated electrons in a RF sputter coater impinge also on the substrate which has to be coated. These electrons cause interaction with the substrate material and heat up the sample. The higher the sputtering yield the higher is the amount of electrons and therefore the temperature increases.
In modern High Resolution SEM biological samples like membranes which respond sensitively to a slightly change in temperature can be investigated. A deposition of a conductive film on the surface of such temperature sensitive samples is impossible. Therefore, alternative ways of sputtering are necessary. The LEICA sputter coater fulfils some of these criteria, but this device and also devices from competitors form micro-structured thin films which decrease the image quality in High Resolution SEM.
A comparison of sputtered thin gold palladium films of the old RF-sputter coater and the Leica DC magnetron sputter coater can be seen in Figure 20. The ditches between the

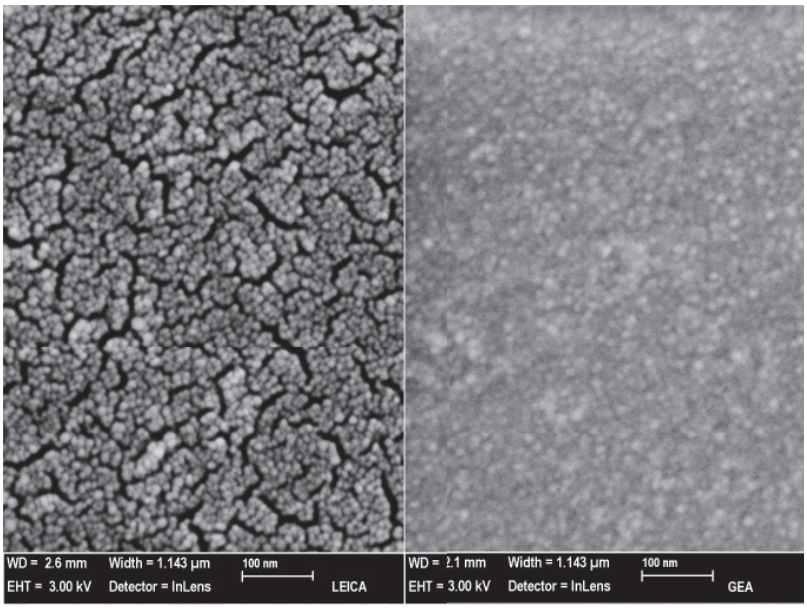

Figure 20: Au/Pd thin film sputtered with Leica DC Magnetron Sputter Coater (left) and with the RF Sputter Coater, called GEA (right) by a magnification of 150,000 times.

agglomerated grains decrease the conductivity drastically and make the usage of this kind of thin film unsuitable. Beside the high resistivity, another point limits the usability of the thin film strongly. The dominant micro-structure will cover any micro and nano

structures of the sample itself.
Leica offers many opportunities to change the film growth by different parameters which are available in the user interface. The task to get a thin film without ditches has to be done in a most scientific way to avoid loosing the overview. The first approach will be to determine all observable quantities of the device, before the systematic variation of the parameters begins.

4

CHARACTERISATION OF LEICA ACE 600 SPUTTER COATER

As it is shown in Chapter 2, the complex growth process of films by PVD techniques has a lot of parameters which can change the properties of the film. Leica used a touch screen with a simple and easy understandable graphical interface to change many parameters and to follow up the current status during the sputtering process.
Three main quantities which also appear during the chapter of the basics are temperature of the substrate, thickness and the pressure. All these parameter can be changed directly or indirectly, but how the values fit to reality will be described inside this chapter.
In most cases it is common practise to verify parameters by another independent measurement method and to compare the results. To get a significant result with a meaningful statistic a sufficient number of measurements is necessary and it has to be considered how the new method is prone to error.

4.1 TEMPERATURE IMPACT DURING THE SPUTTER PROCESS ON THE SURFACE

The temperature on the substrate is the only parameter which cannot be changed directly and which has no output field at the software of the sputter coater. There are two ways to generate heat on the surface of the sample. On one hand an indirect parameter for temperature is the working distance and on the other hand the sputtering current. For the working distance counts that the nearer the sample stands to the plasma, the hotter gets the surface. Fast target atoms produce phonons in the solid and heat up the sample. The sputtering current, in turn, leads to a higher amount of target atoms which are able to impinge at the surface.
The temperature of the substrate is an important parameter for the growth of the metallic film because many diffusion processes depend on it. But there is another reason, too. The metallic film should fulfil several requirements to make it usable for *High Resolution Electron Microscopy*. One of these is a low temperature impact during the sputter process. A lot of biological samples which can be observed with high resolution are high temperature sensitive. But there are two types of temperatures which influence the sample. The global temperature which is represented as the mean value of the whole surface and the local temperature of the region where an accelerated particle impinges the surface. The kinetic energy of the particle is transferred totally to a small local volume and leads to a high increase of the temperature, much higher than the global temperature. Especially membranes which functions are based on very small structures, called fibrils, will be damaged through a drastically increase of the local temperature.

4.1.1 *Measurement Method*

The measurement method itself is quite simple. A thermocouple of type K (model: 5SC) and a four channel thermometer (HH147U) both from Omega were used and the thermocouple was located directly at the substrate. Inside the chamber vacuum prevails and a connection from the thermocouple to the measurement device can be implemented with a special designed flange. Now it was possible to measure the temperature at different working distances and sputter currents.

4.1.2 *Results and Error Analysis*

According to the data sheet, the Omega thermometer with the used thermocouple yields a accuracy of $\pm 0.1\%$ of the value of the display plus 0.7°C. This detail is very precise, but it implies that the cable between thermocouple and the measurement unit has no disconnection. The modification of the cable by soldering to the flange, leads to a transition between two different kinds of metals. Such a transition causes an additional voltage and a higher error has to be assumed. A common used material for conducting an insulated material for electron microscopy is an alloy of gold-palladium (AuPd). The concentration of AuPd is 80:20. Leica offers a set of default recipes for different kinds of sputter targets. Now, the starting point of the measurement will be begun at the default settings for the common used AuPd target:

Table 1: Default sputtering parameters of Leica

sputter current $I_{sputter}$	[mA]	30	working distance WD	[mm]	50
pre-vacuum $p_{pre-vac}$	[mbar]	$5e-5$	sputter-vacuum p_{Ar}	[mbar]	$5e-2$
rotation rot	[-]	3	tilt t	[–]	0
thickness d	[nm]	10			
substrate material	[–]	soda-lime glass	target material	[–]	AuPd

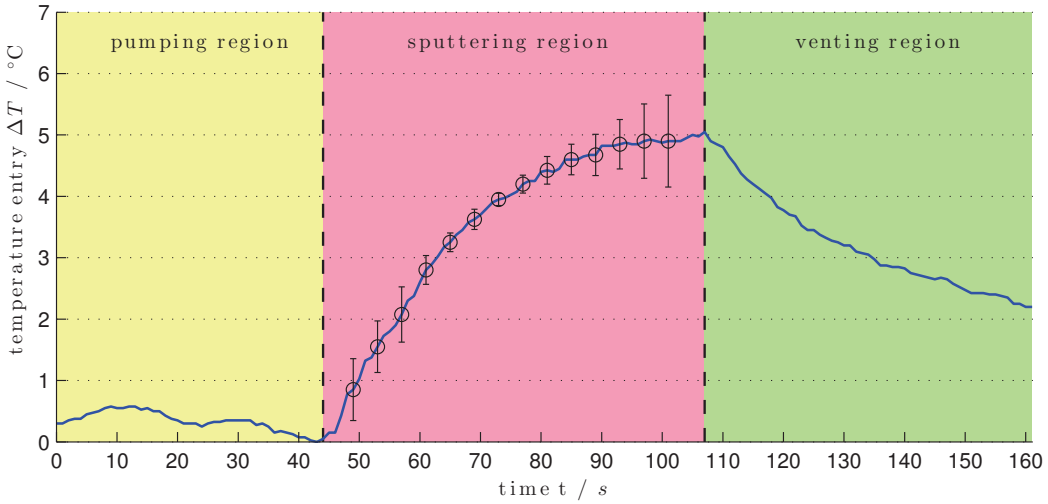

Figure 21: Temperature impact as function of time during the sputter process with default settings, which are tabulated at Table 1. Overlaid regions show the status of the sputtering. Error bars were added, the mean deviation is ± 0.6°C.

To get a precise result, the measurement was repeated four times. The mean value of all four graphs results in Figure 21 with drawn errorbars. The error bars are calculated from the standard deviation of the mean value. As it is shown in the figure, the values are irregular within the sputtering region. The reason for that is the response time of the measurement device. The device sweeps the temperature value of the thermocouple every second. If the temperature gradient is very high, the error gets higher due to the dead time between the time where the thermometer gets the value and saves it into the internal storage. The mean deviation is 0.6°C and has to be summed up to the error of the thermometer.
In addition, different regions are drawn in the figure. The first one is the pumping region. The vacuum pump of the sputter coater pumps to the set pre-vacuum value and purges

the chamber by flooding it with argon gas. Afterwards the pressure of the set sputter-vacuum value adjusts - nearly no temperature impact occurs inside the chamber. The next step is the ignition of the plasma and the beginning of the sputtering process, if the desired atmosphere is reached - temperature impact increases at the substrate. Now, the sputter process is finished because the thickness, which is measured by a quartz, is reached. The venting process starts immediately to cool down the chamber and to reach the ambient pressure for getting access to the sample.

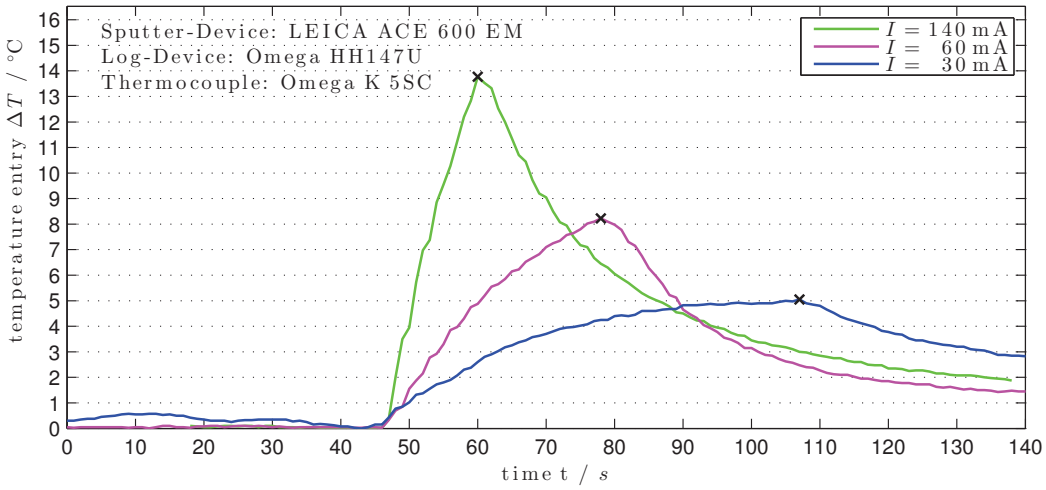

Figure 22: Temperature impact as function of time during the sputter process with different sputter current. Other parameters are set like in Table 1.

Based on the default settings, different values for the current are applied to show an increasing temperature impact due to the higher sputtering yield. The thickness of d = 10 nm is held constant, because thicker thin films are not suitable for High Resolution SEM. Therefore, the sputter region in Figure 22 becomes smaller and smaller, because a higher sputtering yield increases the deposition rate of target atoms, too. But a higher deposition rate, in turn, leads to a higher temperature impact. The maximum temperature impact of $\Delta T_{max,10nm} = (14 \pm 2)°C$ appears at modified default settings with a sputter current of I = 140 mA. The temperature impact is a relative value related to the ambient temperature and defines a quantity for describing the added heat to the substrate. Therefore, the higher the sputtering yield, quantified by the sputter current, the higher gets the temperature at the substrate.

The next modification of the default settings was used for visualising the changing of the temperature by different working distances. First of all, a change of the WD has more effect than a change of the sputter current. Hence, the thickness of the deposited film was held constant again, but not at d = 10 nm. The thickness is changed to d = 4 nm as a practicable approach to reduce the sputter time and getting a comparable dataset. Figure 23 depicts two measurements, which represent on one hand the lowest possible WD (green graph) and on the other hand the highest possible WD (blue graph).
At $WD = 97$ mm, the temperature impact is around 0.5°C with the error of ±2°C, the impact to the substrate is virtually non-existent, but at $WD = 30$ mm the substrate is very close to the plasma ring and reaches the maximum at $\Delta T_{max,4nm} = (13 \pm 2)°C$. It would increase further if the sputter process did not stop.
A common used device for sputtering thin films on samples, which has to be prepared for SEM, is a RF sputter coater. This type of coater produces thin films with smooth surfaces and without micro structures. Therefore, a measurement of the temperature impact was done to visualise the main difference between both devices. Fig-

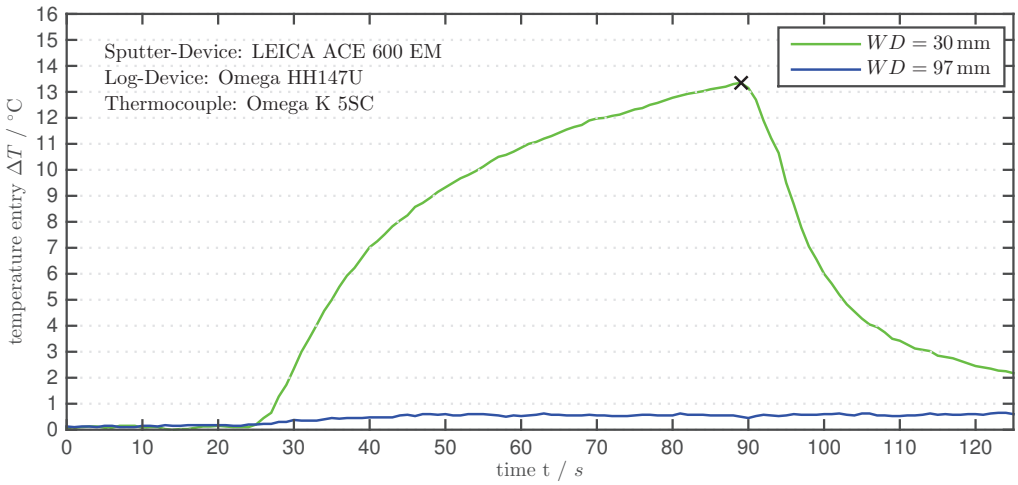

Figure 23: Temperature impact as function of time during the sputter process with different working distances.

ure 24 shows the temperature impacts of the different types of coaters as function of time. The maximum relative temperature impact of GEA for a 10-nanometre-thin film reaches $\Delta T_{max,10nm} = (26 \pm 2)°C$ and is much higher as the temperature impact of the Leica sputter coater at $WD = 97\,\mathrm{mm}$.

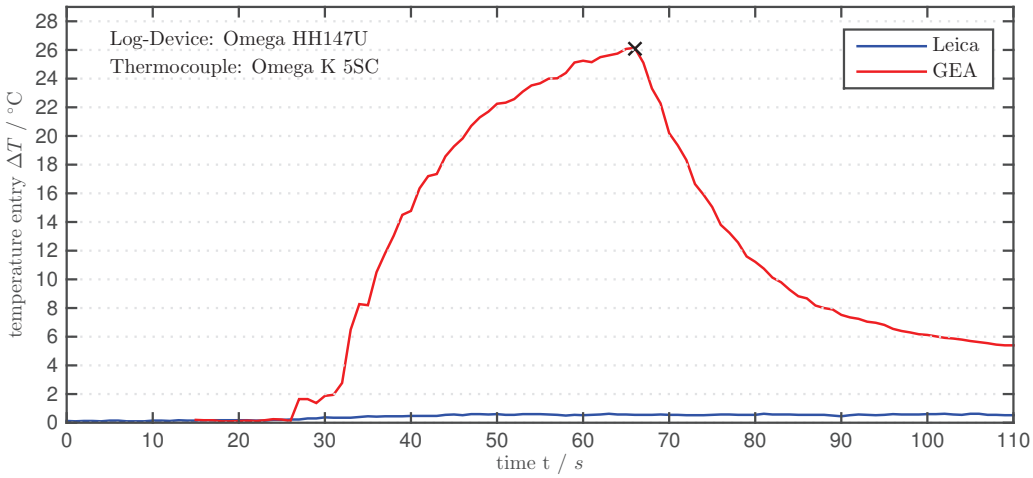

Figure 24: The comparison of the temperature impact as function of time between a RF Sputter Coater, called GEA, and the Leica DC Magnetron sputter coater.

The working distance of the RF sputter coater is nearly the same like the used working distance at the Leica. The reason for the much higher temperature impact is that an electron trap is missing. This electrons change their direction continuously between target and sample due to the applied alternating electric field. This alternating pole change leads to a movement of the electrons through the sample which causes an interaction between the electrons and the sample. Hence, this kind of interaction provokes the rising of the temperature.
In addition to the difference in temperature, a higher sputtering rate of the GEA was noticed, which could also play a role for a continuously grown film. Therefore, the comparison between GEA and Leica can be useful to get a hint which parameters are more important than others.

4.2 THICKNESS OF SPUTTERED THIN FILMS

The thickness of a sputtered film with the Leica sputter coater is measured by a quartz crystal. It measures a mass per unit area by changing its frequency, if sputtered atoms arrive at the quartz resonator.
Leica uses different mass coefficients for different materials to calibrate the quartz measurement unit in the user interface. The question is how precisely this kind of measurement works at really thin films of about 10 nm or less. There are several factors which have to be taken into account. One of these is the fact that the ideal position of the crystal should be directly next to the substrate. This is not really suitable on the engineering point of view, therefore shadowing effects are one of the side effects which influence the accuracy of the thickness measurement.
Another effect will be the ability to rotate the table, where the sample can be mounted, during the sputter process. The quartz is located in the rotation centre. Hence, the sample is half-time during the sputter process out of the region of the sputter deposition. However, the quartz located in the centre is almost always inside the region, where sputtered atoms impinge the surface of the resonator.
Now, it is necessary to quantize the error. A comparison of different sputtered films is impossible, if no facts about the accuracy of the thickness are known. Two methods were applied to measure the thickness independently from the quartz measurements.

4.2.1 *Measurement Method 1: Wedge Cleavage*

The *Wedge Cleavage Technique* (WCT) is a well-known preparation technique, illustrated in [1], for generating electron transparent substrates for transmission electron microscopy (TEM). These substrates have to be consisted of materials, which have oriented braking directions.

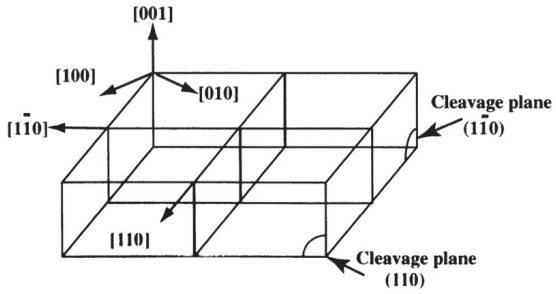

Figure 25: Prepared sample with two perfect edges [1].

The directions are oriented because the bonding energy between the atoms perpendicular to this directions is very weak and will be preferred for a break through. A common example for such a material is silicon or GaAs, which is used for microchips. They are processed as wafers, a round, thin, monocrystalline disc, which forms the base where structures were applied by e.g. lithography processes.
Out of a wafer an approximately 0.6 mm^2 thin sample is broken with at least one perfect edge. Figure 25 shows the resulting sample and marks both perfect edges with arrows.
The reason why this kind of edges will be striven is the fact that the tip of a perfect edge is just a few monolayers thick. Therefore, electron transparency is generated by mechanical fracturing.
This preparation technique in combination with a sample holder, which allows the sample to rotate along certain directions relative to the electron beam. With this technique, it

is possible to adjust the sample like in Figure 26 to get a projection of the cross section of the substrate.

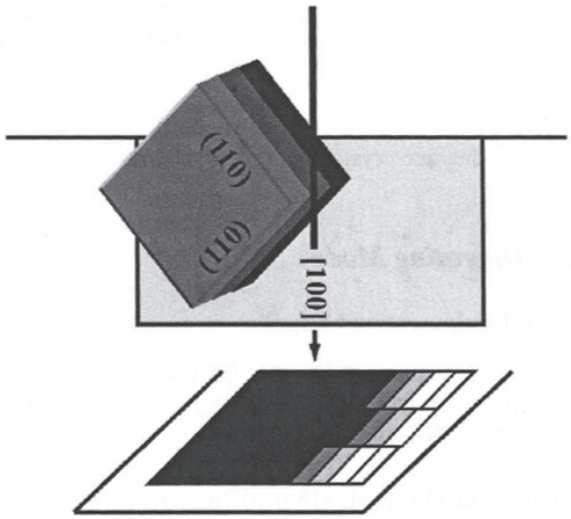

Figure 26: Usage of the perfect edge to get a projection of the cross section [1].

The idea is to sputter the film on the substrate, which is prepared by mechanical fractioning to get an electron transparent edge with the thin film on it. With the cross section, the mean thickness of the film can be measured. A thickness of a single edge is not representative to estimate a mean value for the whole substrate, but if more measurements are taken a sufficient statistic can be reached. Therefore, more than ten samples out of a 0.6 mm^2 Si area can be prepared.
To evaluate the thickness, thin films with different sputter conditions were produced, like variation of current, working distance, and argon pressure.

4.2.2 *Measurement Method 1: Results and Error Analysis*

Analysing the almost perfect edge with the TEM leads to the result in Figure 27. The sputtered thin film which is marked with a white rectangle is deposited on substrate consisting of a broken silicon wafer. The surrounding white area is vacuum on the bright field image. No energy loss occurs and the electrons are directed towards the detector directly. The figure depicts the cross section of the film and it can be shown that the film does not grow densely. White spaces in between can be observed. A fluffy growth, where no densely packed film results, rises to a challenge with the preparation method more than expected. The mechanical cohesion at the substrate is quite low and leads to crumbling of the film during the preparation. This made it difficult to analyse further samples with different kinds of deposited thin films. At the important range, where the substrate has the thinnest thickness about some sub nanometres, no AuPd can be found. When the substrate gets thicker, the AuPd film can be seen, like in Figure 27. The problem, which occurs at the analysis was that the substrate and the deposited layers could not be distinguished from each other. An assumption about the thickness cannot be made either.
One opportunity is that the substrate is responsible for the low cohesion. Another material with a property, which sticks better on Si than AuPd has to be found. A material, which is known for its high cohesion value, is chromium [12]. It will be used to build up an interface between Si and AuPd to stick the film to be measured on the substrate.

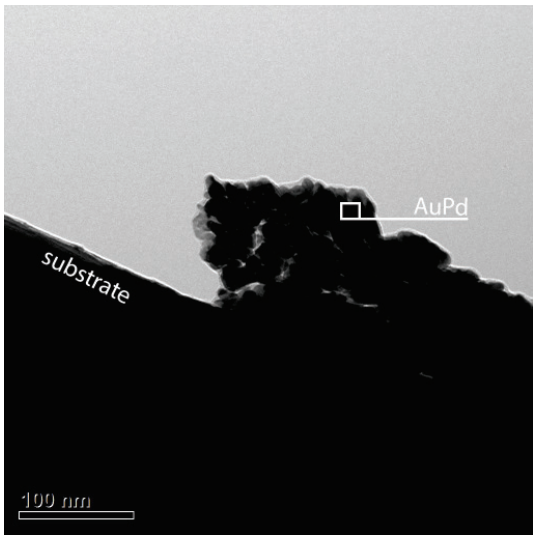

Figure 27: TEM image of AuPd film deposited with parameters of Table 1

Therefore, another experiment was made to deposit a 2 nm Cr layer before the important film was deposited.

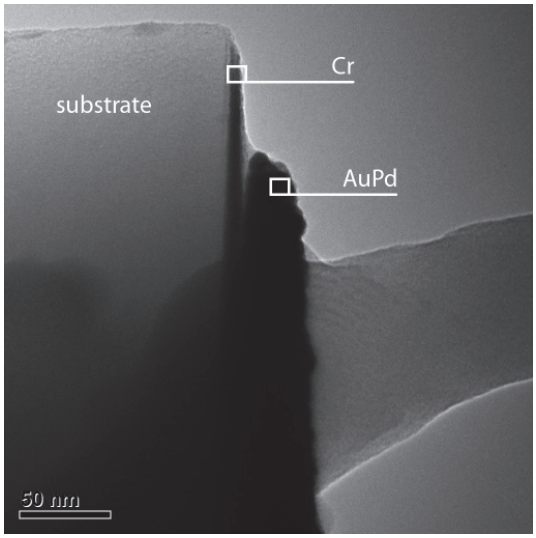

Figure 28: TEM image of a AuPd film deposited on a Cr layer.

The result is depicted in Figure 28, where the Cr layer sticks perfectly along the whole breaking edge in contrast to AuPd, which crumbles again. Therefore, the experiment by measuring the thickness of different deposited gold palladium films was stopped and had to be taken back on another technique for evaluating the thickness of the metallic thin films.

4.2.3 *Measurement Method 2: Focussed Ion Beam Lamella*

The second method to measure thickness is simpler, but it is more time-consuming and costly. Ten or more samples cannot be prepared as fast as using the WCT. Therefore, a multilayer of two materials with different thicknesses has to be deposited on a substrate based on a nickel alloy. It is useful to choose two materials, which have a big difference between their atomic numbers. In the TEM the High Angle Annular Dark Field (HAADF) detector was used mainly to get material contrast between those layers. Materials which lie next to each other in the periodic table have less contrast differences and therefore a higher error occurs by separating the interfaces manually. The combination of gold and tungsten as target material was the best choice. There are other materials, which can be used, i.e. aluminium, because the difference of the atomic number is bigger, but the much lighter aluminium forms aluminium-oxide on its surface quite easily.

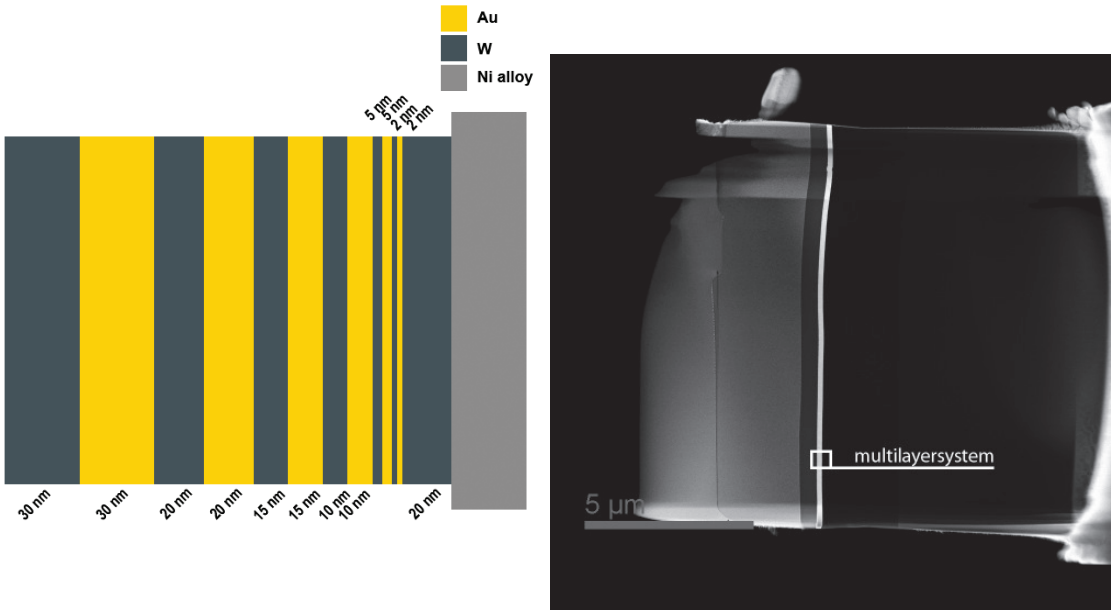

Figure 29: Schematic of sputtered multilayer film on a nickel based alloy substrate (left) and a Darkfield TEM image of the FIB lamella (right).

After the film was deposited, a small part of the substrate was cut by the *Focused Ion Beam Microscope* and afterwards it was thinned to make it electron transparent. The resulting object was now a cross section of the multilayer Au-W film system, called lamella, and could be observed in the TEM to measure the thickness of the single layers. Due to the disadvantages of the method, significant statistics cannot be reached, but it is possible to observe different materials with different thickness with just one sample. The width of the lamella is also bigger than the dimensions of a single edge, therefore a statement about the homogeneity of the deposited film system can be determined.

4.2.4 *Measurement Method 2: Results and Error Analysis*

The TEM image of the FIB lamella, which is shown in Figure 29 (right) looks different than the schematic in Figure 29 (left). The white area in the middle of the lamella is the film which has to be measured and which has the structure of the drawn schematic above. The sputtered multilayersystem is embedded on the left side in a platinum (Pt) deposition of about five micrometres and on the right side in the substrate.
Deposition of platinum on a surface which has to be cut out by a high energetic ion beam

is a common procedure [23] to protect regions of interest from process artefacts, like in Figure 29 (right) at the upper side of the lamella. If the FIB cut was done without Pt, the layer on the upper side of the image could not be analysed. Now, two technical solutions are available to determine the thickness out of the TEM analyses.

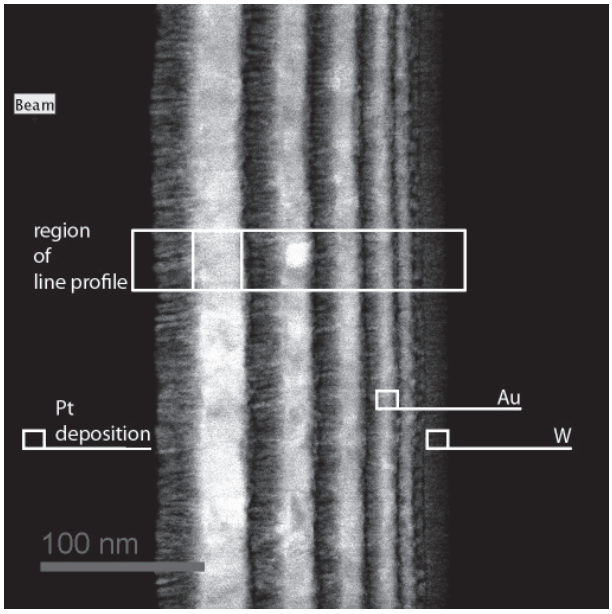

Figure 30: Darkfield TEM image of multilayersystem measured by FEI detector.

On one hand an analysis by the grey values of the dark field image like in Figure 30 leads to an estimation of the thickness value and on the other hand an analysis by the countrate of an EDX measurement which can be performed along the region of the line profile of the DF image is also possible. Both methods were performed to get a set of values for each layer. The estimation is calculated by the mean value and the standard deviation of both methods on five different positions along the lamella. This region marked with an big white rectangular is used to calculate the line profile. The wider the width of the rectangular the more single lines are included into the mean value of the line profile. The following analysis performed by the line profile is averaged by 100 lines which are equivalent to 100 pixels in the TEM image. The resulting line profile is shown in Figure 31. With the help of this graph, the limits for the single films can be determined easily by measuring the distance between the half height of the maximum values of the peaks.

The error analysis of the single method is quite difficult to determine because the error depends on the accuracy of the experimentalist and the arrangement of the sample inside the TEM. If the surface lamella does not lie exactly perpendicular to the electron beam, one will measure a projection of the cross-section, which differs slightly from the original value.

The second analysis procedure uses the characteristic x-ray radiation. The value of a certain characteristic peak position of one material is tracked during a single line scan along the multilayer system. Therefore, it is necessary that both materials, which have to be analysed, have either characteristic x-ray peaks which do not lie too close to each other and a high intensity for a significant change for an easy determination of the film limits.

Figure 32 shows the individual line profile for each material. Most important for determining the thickness of the sputtered films are tungsten (red graph) and gold (blue graph). The other materials occur from the substrate - a nickel based alloy. Oxygen (black

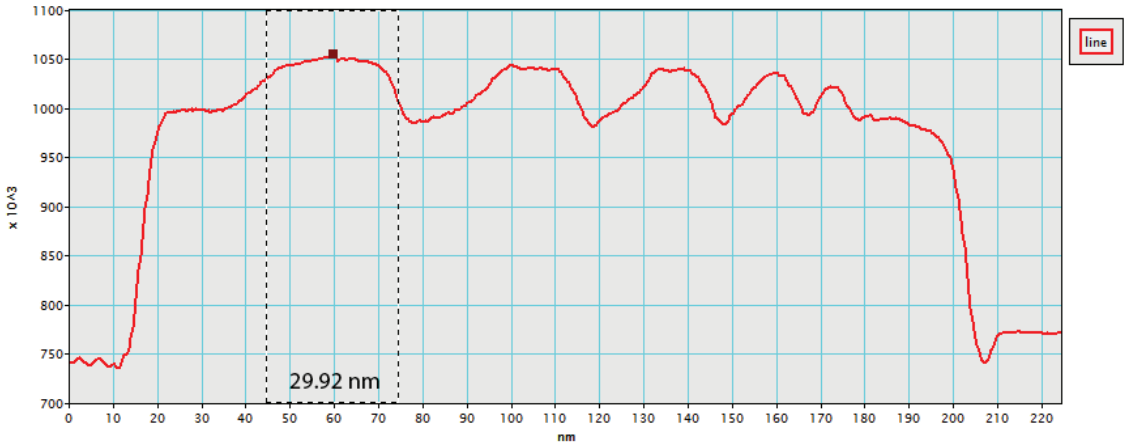

Figure 31: Line profile with 100 px in width of the darkfield TEM image.

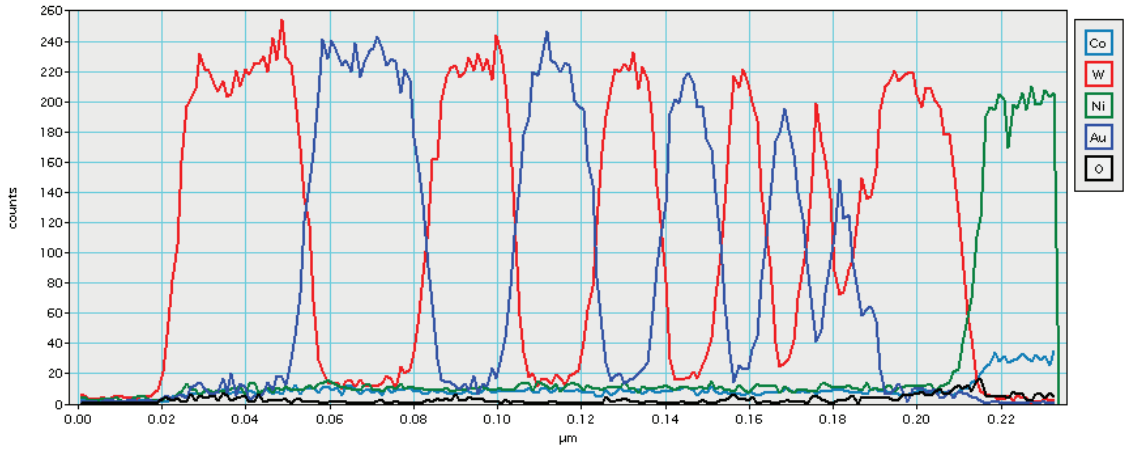

Figure 32: EDX line profile along the same position as marked in Figure 30.

graph) is also depicted in the figure because it rises significantly during detecting of the characteristic x-ray peak of tungsten. Thus, it can be assumed that tungsten prefers the bonding with oxygen atoms and therefore a better pre-vacuum is sufficient for getting a pure metal layer without build-in oxygen atoms.
Both methods lead to a good analysis of the cross-sectional view of the sputtered metal films. To evaluate the deviation from the expectation value, the lines profile and the EDX profile are taken three times at three different positions.
But both methods are limited. Thin films, which are equal or thinner than 2 nm cannot be evaluated. At the line profile the thermal drift of the device is to big to depict a clear, noise-free image from the thinnest layer. The other method is limited by the size of interaction volume, in which x-rays are generated. This volume size depends on the material, too. For tungsten or gold the diameter of the volume is obviously the width between 2 nm and 5 nm, because the count rate of the x-ray detection decreases. An evaluation of the thinnest films is not possible with these kinds of methods. Following, the comparison of the expectation value which is set by the Leica sputter coater, the measured thickness values and the standard deviations from the average of the three measurements are shown in Table 2.

The comparison between expectation values and measured thickness values shows that the difference is quite low. It differs between 0.0 % - 22 % as relative values. The maximum, absolute value for the difference in thickness from the expected value is 3.1 nm at the 30 nm tungsten layer. This value has also the highest deviation value and let suppose

Table 2: Comparison of the measured thickness and the expectation value

d_{Leica}	...	setted thickness, whereat the sputter process will stop in nm
$\overline{d_{measured}}$	...	arithmetic averaged thickness value of all measurement methods in nm
$\Delta\overline{d_{measured}}$	...	standard deviation of the averaged value in nm
$\overline{d_{measured}} - d_{Leica}$	...	difference between expectation value and measured value in %
	...	difference between expectation value and measured value in nm

Material	d_{Leica} [nm]	$\overline{d_{measured}}$ [nm]	$\Delta\overline{d_{measured}}$ [nm]	$\overline{d_{measured}} - d_{Leica}$ [%]	[nm]
W	30.0	26.9	1.5	10.3	3.1
Au	30.0	28.5	0.8	5.0	1.5
W	20.0	20.7	0.4	3.5	0.7
Au	20.0	19.9	0.1	0.5	0.1
W	15.0	15.1	0.1	0.6	0.1
Au	15.0	14.5	0.3	3.3	0.5
W	10.0	10.5	0.3	5	0.5
Au	10.0	9.2	0.4	8	0.8
W	5.0	6.1	0.6	22	1.1
Au	5.0	5.0	0.0	0	0.0

that a systematic error could be the reason for the high standard deviation. The problem with the measurement at the thinnest layer arises from low contrast difference between tungsten and the deposited platinum and occurs in the line profile, like in Figure 31. The dotted rectangle in the figure marks the region of the last gold layer, which thickness is still determinable. Therefore, the high standard deviation shows that no clearly boundary between platinum and tungsten can be found, but all other thickness measurements are quite good and have an acceptable deviation for all upcoming measurements. Another difference is that tungsten got a continuously slightly higher measured thickness values than gold. The reason is possibly the build-in oxygen atoms, which change the material contrast. The boundaries of tungsten look blurred and not as clear as gold.

The first experiment of measuring the thickness by using a FIB cut and analysing it by TEM was unsuccessful because on one hand the target materials were chosen disadvantageously and on the other hand the measurements were performed by high thermal drifts. Gold and platinum were used for the first trial, but the atomic numbers are too near together to get a good material contrast and also the characteristic x-ray peaks overlaid partially each other. Hence, the analysis failed and the standard deviation rose highly due to the occurrence of a high systematic error. The boundaries of the layers became blurred by the thermal drift and the resulting error was integrated into the highly occurred error.

The build-in atoms form a no ideal basis for the measurement of the thickness value too, but it is a good compromise between the difference of the atomic numbers and the oxidation probability.

In summery, the measurement of the thickness by using a FIB cut of a Au-W multilayer system turns out to be a good method to get a value of the sputtered thickness. The quartz crystal is a common method for measuring real time sputtering processes, but different geometries of the coaters and different positions of the quartz lead to deviations. The best position of the sensor to capture every sputtered particle which impinges the surface of the target would be next to the substrate directly. But from the engineering point of view this solution is quite impossible. Unless the sensor is covered from the

substrate or anything else, it yields a good approximation for the thickness value of the sputtered film. The sputtering atoms of the target material are evenly distributed inside the chamber that the error from the detection of the atoms is acceptable.
Now the thickness error and also the error of the temperature impact are quantified and form an important base for all further experiments. If different films will be compared, both parameters play key roles for the film characterisation. As written in Chapter 2 different growth states appear and depend from the temperature and the deposition rate. If the growth is onward, the thickness defines a good basis for comparing growth states with different set of parameters.

4.3 PRESSURE

The measurement unit for the pressure inside the Leica DC magnetron sputter coater is the Pfeiffer PKR 251 vacuum gauge. According to the data sheet [18] and the operating instruction [19], this vacuum gauge consists of two independent measurement systems for detecting the prevailing pressure of the atmosphere inside the chamber. One unit is a Pirani gauge and the other one is a kind of a cold cathode system which is based on the inverted magnetron principle. The measurements of both gauges are combined to get one signal which precision is increased of the current pressure during the sputter process.
The pressure range of the vacuum gauge lies between $5 \cdot 10^{-9}$ mbar and 1000 mbar at a temperature range of $5 - 55°C$.
The user interface of the sputter coater shows the currently prevailing pressure continuously at the main window as soon as the device is switched on. An additional experiment to evaluate the correctness of the pressure unit was not done, therefore the values and the exactness of the data sheet is used to get information about the error behaviour of the device.
The precision of the pressure is ±30% within the range of $10^{-8} - 10^{2}$ mbar. And the reproducibility is specified with ±5%. To express the precision in values the default setting for the pressure of AuPd is $p = (5 \pm 1.5) \cdot 10^{-2}$ mbar. Another parameter which is further specified is the response time of the Pfeiffer vacuum gauge with ≈ 10 ms for pressures which are greater than 10^{-6} mbar and ≈ 1 s for pressures equals to 10^{-8} mbar.

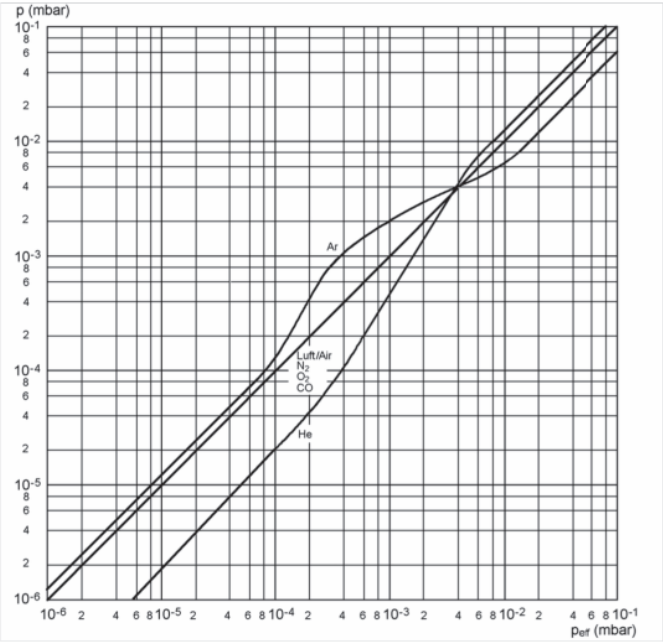

Figure 33: Pressure indication range between 10^{-6} to 10^{-1} mbar of Pfeiffer PKR 251 vacuum gauge calibrated for air.

Figure 33 shows the behaviour of the pressure detection for different gases inside the chamber. The gauge is calibrated for air, thus the effective pressure is the same as the measured one. In contrast, if the chamber is filled with argon the resulting signal differs from the reality. Therefore, a conversation formula is specified for different materials with $p_{eff,Ar} = 0.8 * p_{indicated}$. But in the range between 10^{-4} to 10^{-2} mbar this simple formalism cannot be held and the error of the indicated pressure increases.

5

MORPHOLOGICAL EFFECTS BY VARIATION OF SINGLE PARAMETERS

One aim of this work is to generate a film which contains as less as possible morphological irregularities as possible. First, it has to be considered which parameters influence the film growth and which method is going to be used to observe it in a mostly time-consuming way. There are many parameters which are changeable and therefore a good concept for the further measurements has to be introduced to separate each morphological effect from the cause from which it is stemming from.
The starting point will be the alloy AuPd as target material which is made of 80 % of gold and 20 % of palladium. In Scanning Electron Microscopy, AuPd or platinum-palladium (PtPd) is typically used for evaporating processes. The reason for this choice is on one hand the less interaction with other materials (inert behaviour) and the moderate costs in comparison to other targets. The oxidation resistance is also an important point. For this reason, chromium or aluminium make the experimental handling with these materials quite complicated.
Literature about generating thin films by DC magnetron techniques favours three parameters for changing the morphological behaviour [27], the power for the sputter process, the working distance and the argon pressure. The main difference of the thin films of literature and the thin films of this master thesis is the thickness. For instance Slavcheva et al. [27] investigated films with a thickness of about more than 100 µm. The thickness that is mainly used for electron microscopy is between 5 nm and 20 nm. Insulated materials having a surface structure, which have to be observed by SEM, are covered by a thin film which does not overlay this structure but has to be thick enough for draining the induced electrons. Therefore, the thickness plays an important role too and has to be observed besides the three parameters which are preferred from literature. The power of the sputter process is one of the parameters which is not changeable at the device of Leica. Power is defined as voltage multiplied by the current. The sputter coater of Leica has just the opportunity to change the current. But the current of the sputter process is no directly physical parameter - it is the current of a power supply, which is held constant to generate a constant electrical field between target and substrate. The reason for denoting the current instead of the voltage will be that current is easier to measure inside the high voltage supply and it is more stable for getting feedback about the plasma stability as if the voltage would be measured (information from R&D department of Leica Microsystems, personal correspondence with Dr. Wurzinger).
By generating thin films with low thickness another parameter has to be investigated - the substrate. As written in the theoretical part, the interaction between substrate atoms and target atoms can change the growth mode inside the first monolayers. Mostly biological samples have no certain crystalline orientation at theirs surfaces, but some alloys for the industrial use, which are also analysed, could have some preferred orientations. In this case, the striven thin film should also be free of ditches. Summarised, five parameters are of special interest for changing the surface morphology - thickness, working distance, current, argon pressure and the substrate.
It is unknown how these parameters interplay together for getting an improvement of the surface behaviour. Therefore, an analytically orientated concept is useful to reach the goal. The first assumption is the isolation of each effect from each cause. Later, if it is

necessary, combinations of some variations of parameters have to be considered. Starting with the default parameters of Leica in Table 1, every single parameter is varied to its limits and every effect of the surface gets recorded.
To detect the changes in a time-consuming and fast way the High Resolution SEM (ZEISS Ultra 55) is used. Besides the effect on the morphology the conductivity can also be detected qualitatively. More details about the device are written in Section 2.5.1.

5.1 THICKNESS

The first parameter, which was observed, was the influence of the thickness on the sputtered film. The line of reasoning was that the increasing of the thickness causes a coalescence of the aggregates of grains which are separated by deep ditches. The theoretical background of the growth in Chapter 2 shows that some characteristic modes exist through the growth process. One of the last growth modes is the formation of ditches or channels due to the fact that the minimal area of the surface is striven.
Based on the default parameters of Leica, four different samples were prepared with different thickness values.

Table 3: Sputtering parameters for varying the thickness parameter

sputter current $I_{sputter}$	[mA]	30	working distance WD	[mm]	50
pre-vacuum $p_{pre-vac}$	[mbar]	$8e-5$	sputter-vacuum p_{Ar}	[mbar]	$5e-2$
rotation rot	[-]	3	tilt t	[–]	0
thickness d	[nm]	2, 10, 20, 50			
substrate material	[–]	silicon	target material	[–]	AuPd

The sputtered thin film is evaporated on a substrate. The substrate should not influence the growth of the film, therefore a basis is chosen which has no crystal orientation. Surfaces with amorphous behaviour are especially suited for this, like glass-slides made of soda-lime glass, or silicon (Si) wafers. During producing a Si wafer, a thermal oxide with several 100 nm in height becomes processed on one side of the wafer which is not used for lithographing electrical devices like capacitors or transistors. This oxide surface is insulating and has an amorphous structure.
The resulting morphologies are depicted in Figure 34 and Figure 35. Especially between the 2-nanometre and 10-nanometre-thin film, a significant change of the morphology is observed. Besides both images, more investigations of less thickness values were performed, but the most meaningful images were used for further evaluations.
A less contrast change between ditches and grains lets assume that the 2-nanometre-thin film is smoother than the others. With increasing thickness the ditches become stronger and the contrast between ditches and grains is greater than in the first HR-SEM image. This result lets assume that the thinner the film is the smaller is the texture of the surface. But during the measurement with the scanning electron beam, it is observed that the resistance of the thin film which has 2 nanometres in height, is much higher than the other surfaces due to less discharge behaviour of the induced charged particles.
On a closer look at the surface of the upper image in Figure 34, the result of the higher resistance seems plausible. The reason for the less conductivity is that the grains are completely surrounded by the ditches. The difference in height between grains and ditches is not that high than on the other surfaces but it suffices to influence the movement of the electrons negatively.

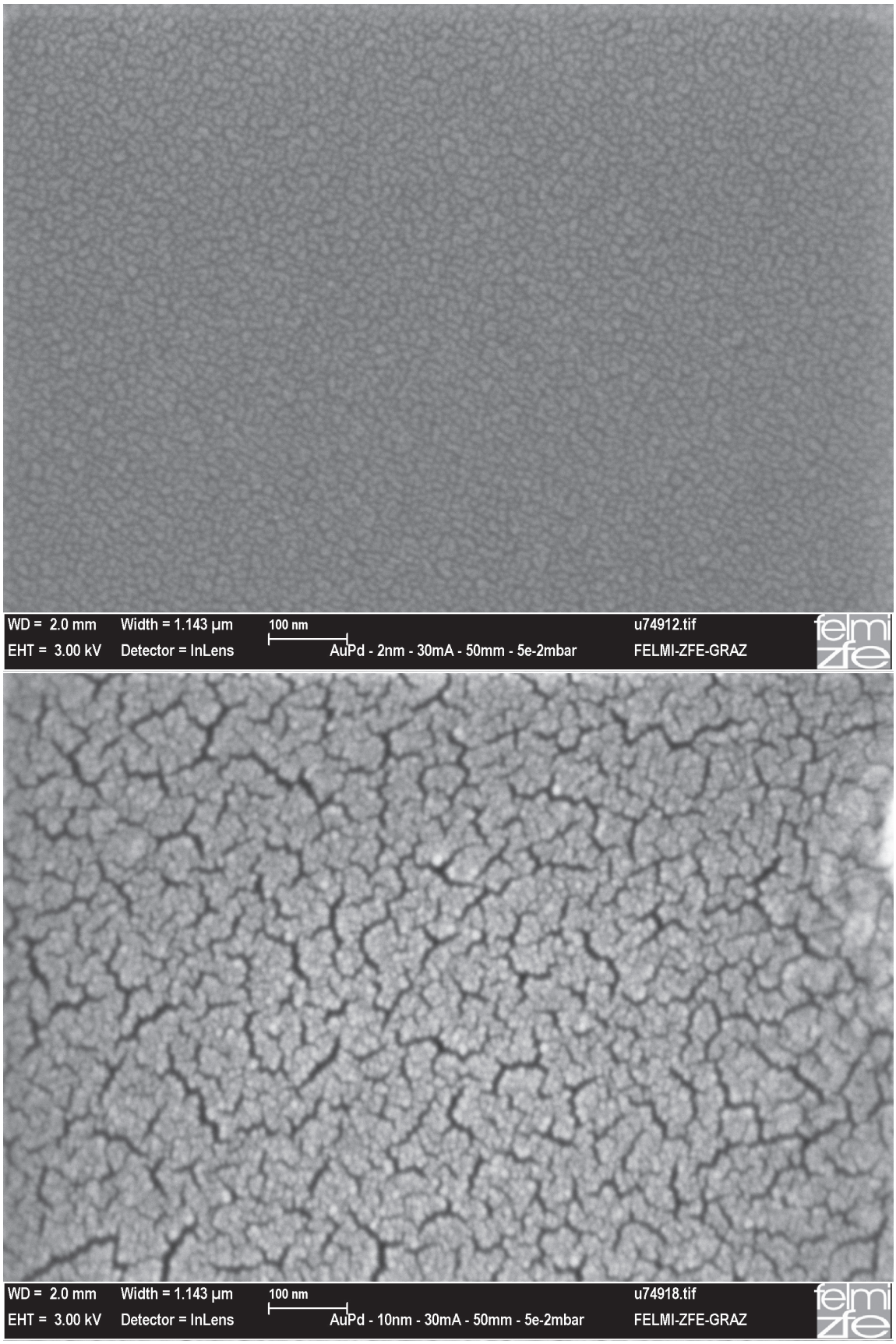

Figure 34: HR-SEM images (In-lens SE detector) with $100,000\times$ magnification based on a $10'' \times 10''$ Polaroid. AuPd films with 2 nm (upper) and 10 nm (lower) thickness.

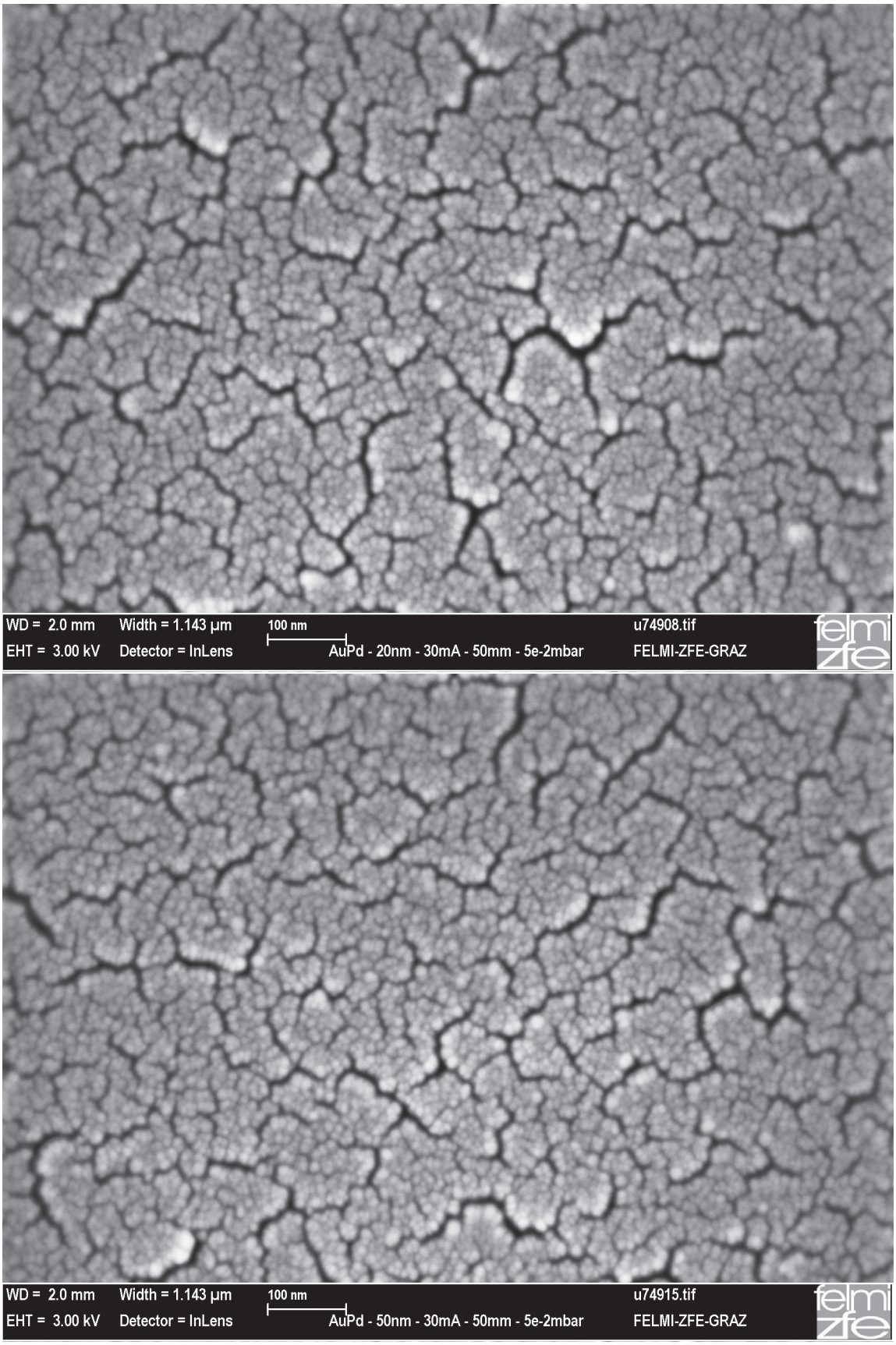

Figure 35: HR-SEM images (In-lens SE detector) with $100,000\times$ magnification based on a 10" $\times$ 10" Polaroid. AuPd films with 20 nm (upper) and 50 nm (lower) thickness.

The increase of the thickness does not lead to the coalescence effect. With a certain possibility the expected effect would appear at much higher values than 50 nm, but the experimental series is aborted at 50 nm because the usage of thicker films is not applicable anymore.
Qualitatively, the amount of the ditches and the dimensions changes slightly but not drastically. To get a quantitative statement, the amount of the dark area is related to the bright area and is expressed in percent. Analysing a characteristic length out of the fractal forms of the ditches is quite difficult. Therefore, the relation between the dark and the bright area is simple and applicable at these images to express a quantity. For sure, the value of pixel related to the dark area, for instance, depends on the threshold which is set, but if all data are compared with each other and the contrast and brightness adjustments are set to nearly the same value, a meaningful statement about the randomly distributed ditches can be made.
A method to analyse the upper threshold of the black ditches works by using the histogram. The histograms of all images are taken and compared with each other. Adjustment of brightness and contrast by using image processing tools changes just the curve shape of the number of pixels along the grey scale. This means a change of the brightness shifts the histogram along the grey scale and the contrast widens it. Now, the contrast settings have to be sufficed to get more than one single Gaussian curve in the histogram. In this case, the global maximum of the different distributions can be used as reference point for an overlay of the histograms. All histograms are shown in Figure 36 (right) with a common maximum at 182 of the grey scale. Afterwards, a Gaussian function

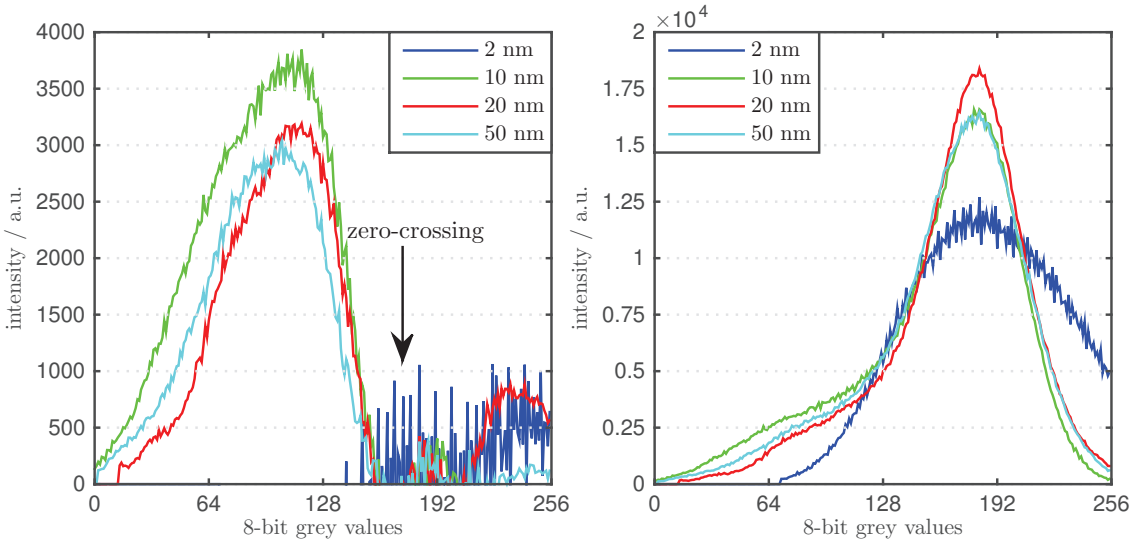

Figure 36: The histogram of the different HR-SEM images (right) and the resulting histogram after subtraction of the Gaussian fit (left).

is fitted around each global maximum of the histogram and the resulting Gaussian is subtracted from the data and leads to the graphs in Figure 36 (left). The area until the first zero-crossing is the number of pixels of the ditches and can be compared with the whole number of pixels to get the area in percent. The percentage of the ditches area in proportion to the grains of the HR-SEM images is shown in Table 4.

In Figure 36 (right), the histogram of the image with the 2-nanometre-thin film becomes noticeable by an insufficient contrast behaviour. The reason for the low contrast is the low height of the grains. Therefore, low secondary electron emission appears and the detectable signal is quite small.

Table 4: Fraction of ditches area in percent of the HR-SEM images of Figure 34 and Figure 35

analysis method	material	thickness d [nm]	sputter rate R [$\frac{nm}{s}$]	area of ditches $A_{ditches}$ [%]
HR-SEM	AuPd	2	0.064	-
HR-SEM	AuPd	10	0.060	23.8
HR-SEM	AuPd	10×1	–	20.1
HR-SEM	AuPd	20	0.057	16.8
HR-SEM	AuPd	50	0.064	17.2

But the other images exhibit a sufficient contrast and cause an acceptable result. The values of the ditches area lies between 23.8 % and 16.8 % with a decreasing behaviour. This decreasing of the ditches area supports the hypothesis that films with thickness above much more than 50 nm grow together to a continuously metallic film.
A further experiment was done to investigate the morphology in relation to the variation of the thickness parameter. The surface of AuPd films of which thickness is less or equal to 2 nm, looks smooth like in the upper image of Figure 34. Therefore a further step to decrease the ditches was, to build a 10-nanometre-thin film which is made of ten times a smoothly 1-nanometre-thin AuPd film.
The result is shown in Figure 37. The size and the percentage of ditches in comparison to the grains does not distinguish from the 10-nanometre-thin film sputtered before.

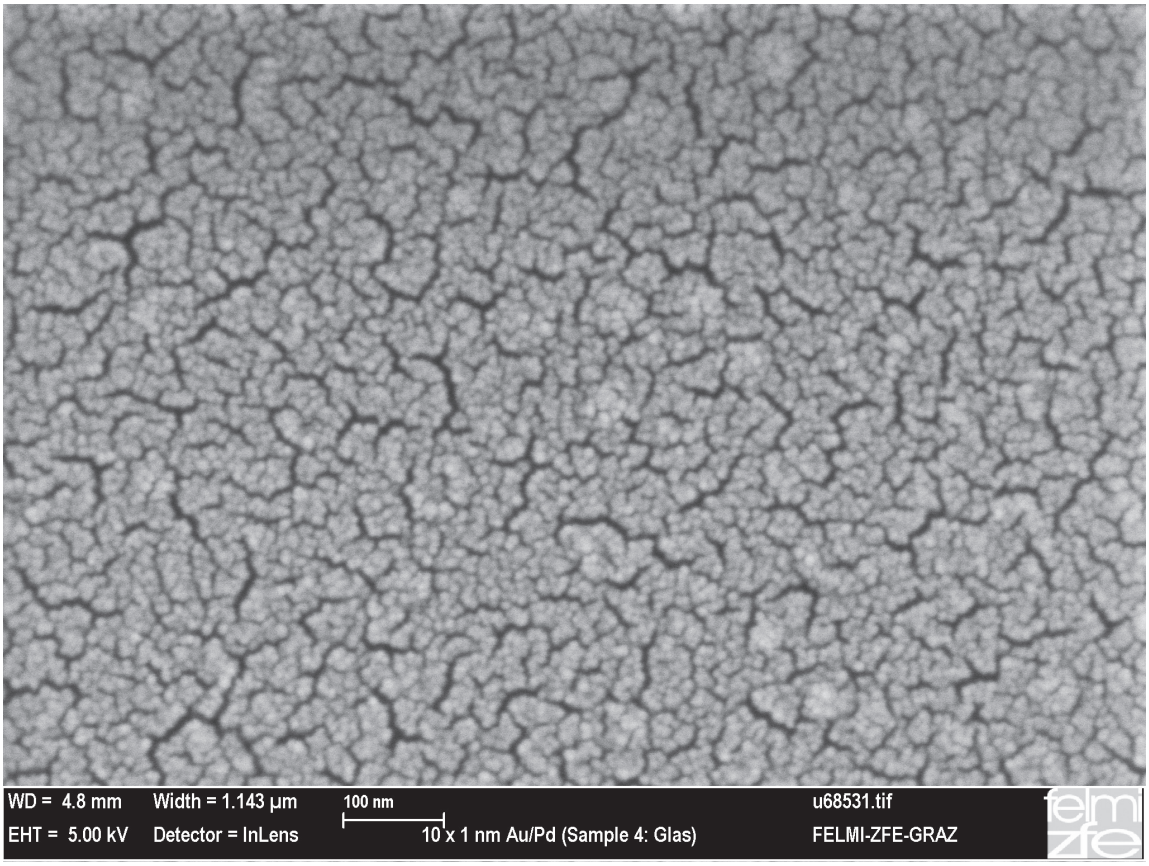

Figure 37: HR-SEM images (In-lens SE detector) with $100,000\times$ magnification. AuPd films with 10×1 nm thickness, sputtered with the parameters of Table 3.

Obviously the film growth cannot be restarted by stopping the sputtering process to start the film growth from the beginning again. If the sputtering process goes on, the film growth continues from that point where it has stopped.

5.2 WORKING DISTANCE

The working distance, which is the distance from the target to the substrate, can be varied within the range from 30 mm to 100 mm. All other parameters (see Table 3) are held constant like in the experiment before. Due to the results of the last section, the thickness is set to 10 nm, while the working distance varies along its whole range with four steps at $WD = \{30, 45, 75, 100\}$ mm.
In this experiment the expectation of getting a change in the morphology is bigger than in the preview experiment because the increasing of the working distance leads to a change of the interaction between the sputtered atoms and the environment. The mean free path of a sputtered particle is around $1 - 10$ cm in the used argon atmosphere, the number of collisions till the sputtered atom arriving the substrate gets higher by increasing the working distance or gets lower for smaller distances. Less collisions mean less transfer of energy to the surrounding argon atoms, the increased remaining energy could be used for moving adatoms on the surface of the substrate.
The result which is seen in Figure 38 and Figure 39 is quite a surprise. The HR-SEM images show broader ditches at working distances which are closer to the target than for those ones which are farer away. Expected was rather an opposite behaviour than the one which was depicted in the images. A higher kinetic energy should lead to a higher movement of the atoms on the surfaces reducing the ditches.
A closer look is taken at the comparison between both extrema - the HR-SEM image of the thin film which is sputtered at $WD = 30$ mm and the image which shows the film with $WD = 100$ mm. Besides the broadening of the ditches another difference can be found. The area of the aggregated grains between the ditches at $WD = 30$ mm are much bigger than those areas at $WD = 100$ mm.
The same analysis procedure as for the variation of thickness is performed for Figure 38 and Figure 39 and the results are shown in Table 5.

Table 5: Fraction of ditches area in percent of the HR-SEM images of Figure 38 and Figure 39

analysis method	material	working dist. WD [mm]	sputter rate R [$\frac{nm}{s}$]	area of ditches $A_{ditches}$ [%]
HR-SEM	AuPd	30	0.057	16.3
HR-SEM	AuPd	45	0.065	22.4
HR-SEM	AuPd	75	0.036	26.4
HR-SEM	AuPd	100	0.021	30.4

The values of the area for the ditches based on the number of pixels show that the assumption which is taken by the human eyes is wrong. The number of ditches increases and therefore the resulting area rises by increasing the working distance. In other words, the agglomeration of grains rises by decreasing of the working distance. The working distance is a parameter which is limited from the geometry of the sputter coater and therefore values which are smaller than 30 mm cannot be evaluated. Looking for another parameter which influences the kinetic energy and also the rate of sputtering atoms seems to be necessary to reach the aim of a texture-free film. The results look quite good for moving the experiments to this direction. The analysis technique for quantifying the ditches works also acceptable. The statements of this method suffice to interpret the images as objectively as possible and the human eyes cannot do.

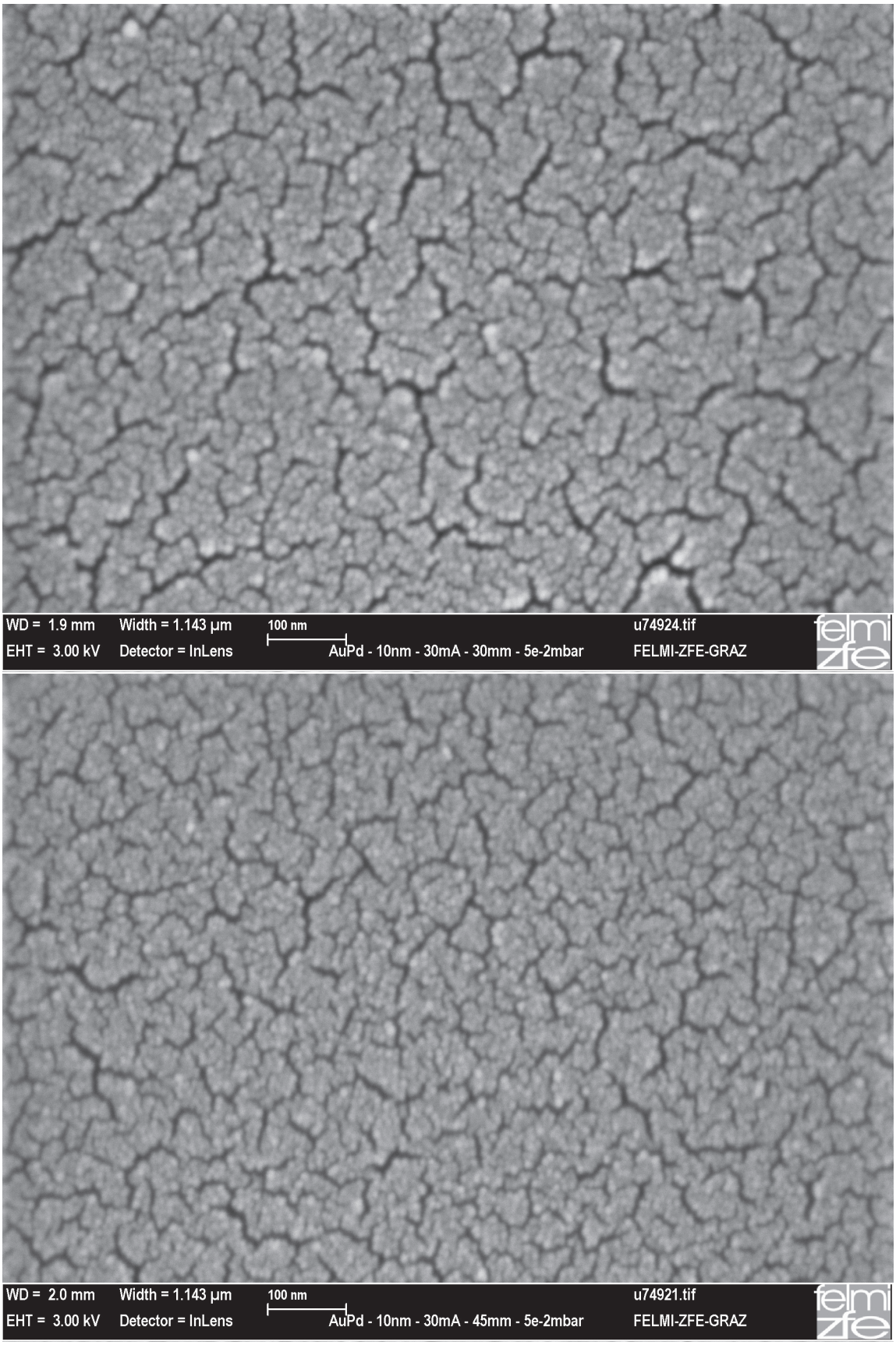

Figure 38: HR-SEM images (In-lens SE detector) with 100,000× magnification. AuPd films sputtered with a working distance of 30 mm (upper) and 45 mm (lower).

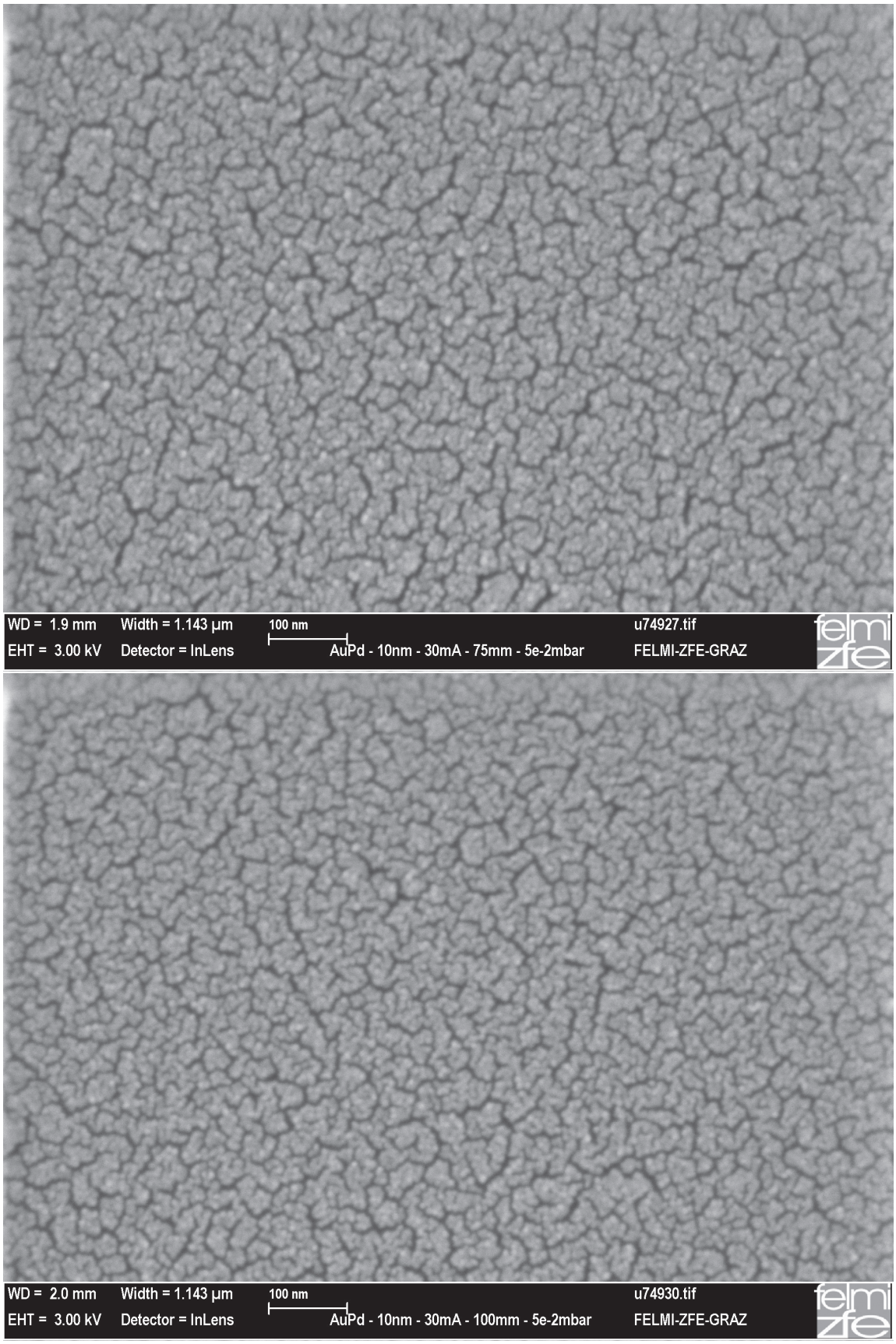

Figure 39: HR-SEM images (In-lens SE detector) with $100,000\times$ magnification. AuPd films sputtered with a working distance of 75 mm (upper) and 100 mm (lower).

5.3 VOLTAGE (CURRENT)

The next step to get a texture-free film is the variation of the applied electrostatic field between target and substrate by changing the value of the current, which is shown in the graphical user interface of the used sputter coater. The voltage changes the acceleration of the ionized Ar-atoms which impinge the surface of the target material.
An Ar-atom with high velocity transfers a higher impulse and leads to a higher emission of target atoms than an atom with slow speed. As written in Section 1.2.3 the energy distribution of the target atoms does not change significantly. The maximum of the distribution lies around a few eV. Therefore, this experiment can be used to observe the morphology by increasing the sputtering rate. The decrease in ditches cannot be assigned to a single physical effect in the measurement before. Either the increasing sputtering rate or the increasing of the kinetic energy were able to improve the surface structure.

Table 6: Sputtering parameters for varying the current parameter

sputter current $I_{sputter}$	[mA]	15, 40, 70, 140	working distance WD	[mm]	50
pre-vacuum $p_{pre-vac}$	[mbar]	$8e-5$	sputter-vacuum p_{Ar}	[mbar]	$5e-2$
rotation rot	[-]	3	tilt t	[–]	0
thickness d	[nm]	10			
substrate material	[–]	silicon	target material	[–]	AuPd

The following measurements which were performed by the parameters in Table 6, are an opportunity to separate the effect of the sputtering rate from the kinetic energy of the sputtered particles. The results are shown in Figure 40 and Figure 41. Without a precise analysis all HR-SEM images show nearly the same distribution of ditches. No drastically effects occur due to the change of the applied voltage.

Table 7: Fraction of ditches area in percent of the HR-SEM images of Figure 40 and Figure 41

analysis method	material	current [mA]	sputter rate R [$\frac{nm}{s}$]	area of ditches $A_{ditches}$ [%]
HR-SEM	AuPd	15	0.022	19.1
HR-SEM	AuPd	40	0.090	23.8
HR-SEM	AuPd	70	0.200	23.9
HR-SEM	AuPd	140	0.530	20.5

As assumed, the analysis with the histogram leads to the same result as expected from the HR-SEM images. The methode to quantify the area of the ditches is not very precise because the error of a single value amounts to $\Delta A_{ditches} = \pm 4\,\%$, but it suffices to notice a certain trend of the change of the morphology. Another fact which influences the precision of the analysis is the sharpness of the images. If the astigmatism of the HR-SEM image is not corrected as good as possible the percentage of the area of the ditches affects negatively, too. To sum up, the sputtering rate does not influence the growth of ditches as much as the working distance does. Therefore, one parameter is still left to try a change of the kinetic energy - the argon pressure, which is discussed in the next section.

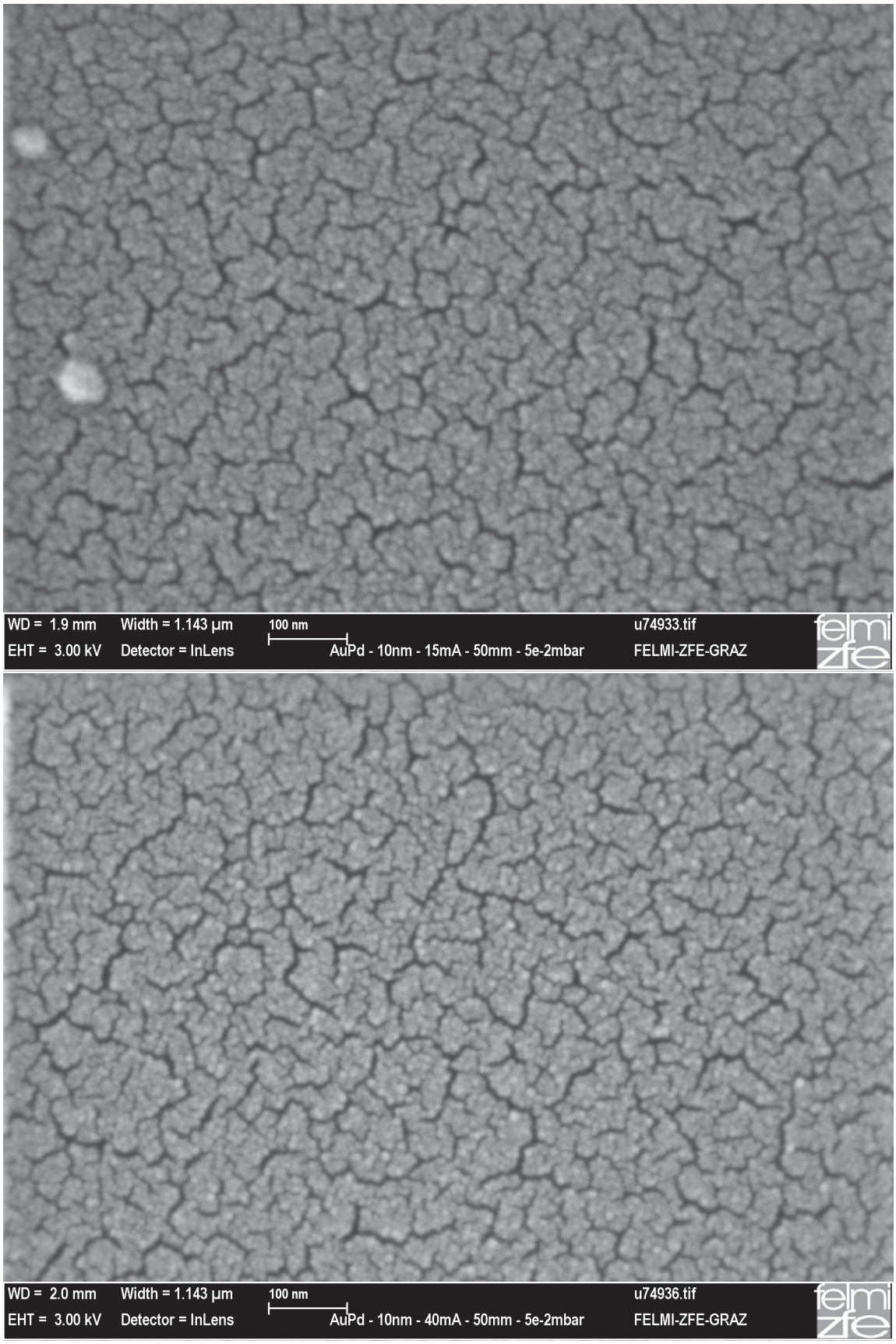

Figure 40: HR-SEM images (In-lens SE detector) with $100,000\times$ magnification. AuPd films sputtered with a sputtering current of 15 mA (upper) and 40 mA (lower).

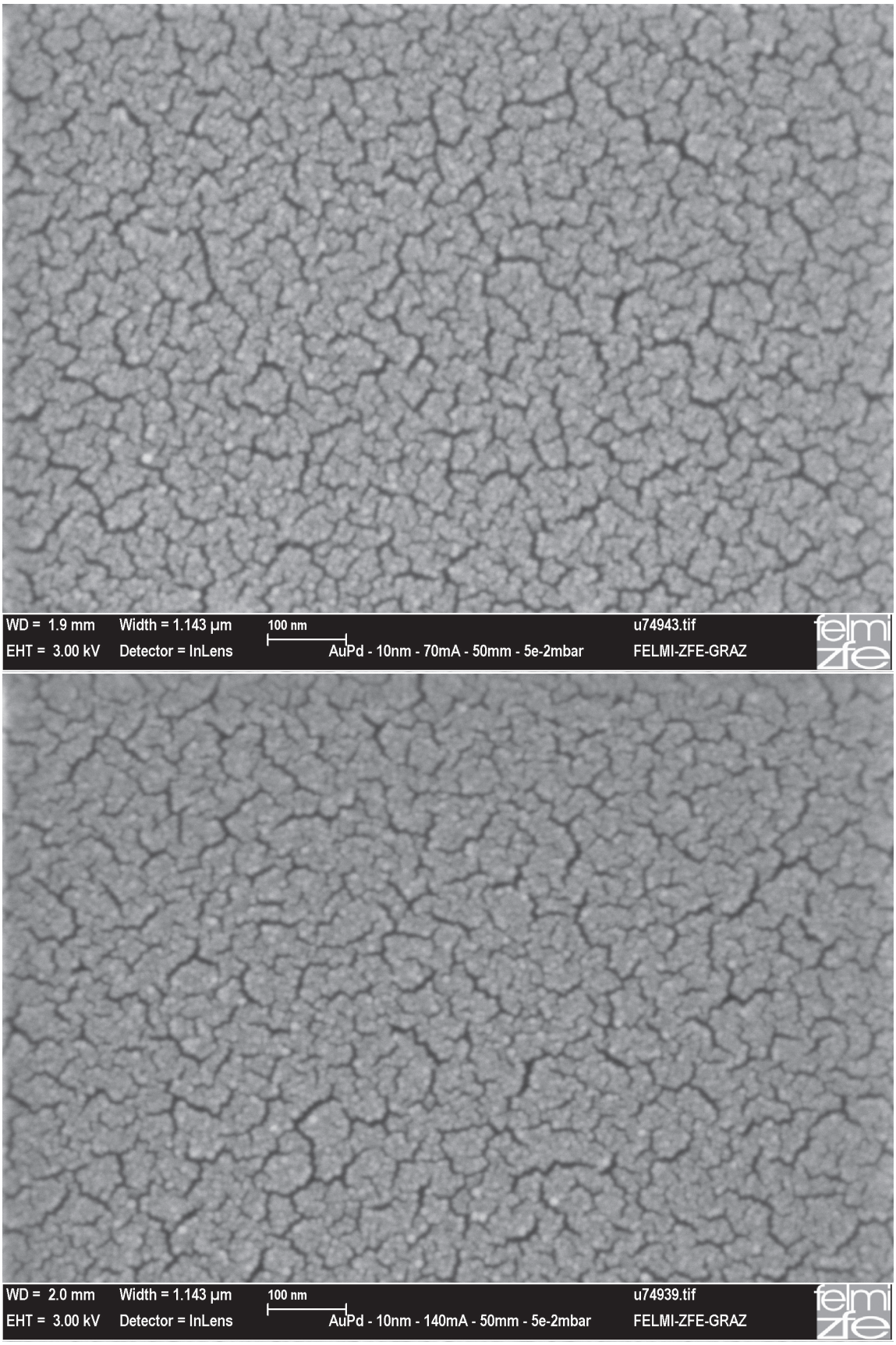

Figure 41: HR-SEM images (In-lens SE detector) with 100,000× magnification. AuPd films sputtered with a sputtering current of 15 mA (upper) and 40 mA (lower).

5.4 ARGON PRESSURE

The parameters are set like in the section before, the film is sputtered with default parameters from Table 1 and the variation of the argon pressure is split in four steps at $p_{Ar} = 6 \cdot 10^{-2}, 3 \cdot 10^{-2}, 1 \cdot 10^{-2}, 8 \cdot 10^{-3}$ mbar. The idea is that the variation of the argon pressure affects the amount of thermalisation effects. The mean free path of the sputtered atoms increases from several mm to some centimetres, estimated by $l = \frac{k_B \cdot T}{\sqrt{2}\pi d^2 p}$ from the kinetic gas theory by decreasing the argon atmosphere to the lower limit of the device. The increased mean free path leads to an increasing of the kinetic energy of the sputtered particles, a higher sputtering rate and a more directional sputtering behaviour than at higher argon pressures. The results of the experiment are depicted in Figure 42 and Figure 43 and the histogram analysis is tabulated in Table 8.

Table 8: Fraction of ditches area in percent of the HR-SEM images of Figure 42 and Figure 43

analysis method	material	argon pressure [mbar]	sputter rate R [$\frac{nm}{s}$]	area of ditches $A_{ditches}$ [%]
HR-SEM	AuPd	$6 \cdot 10^{-2}$	0.052	22.9
HR-SEM	AuPd	$3 \cdot 10^{-2}$	0.104	22.3
HR-SEM	AuPd	$1 \cdot 10^{-2}$	0.185	9.0
HR-SEM	AuPd	$8 \cdot 10^{-3}$	0.196	-

The analysis by the histogram of the grey values reveals a drop of the percentage from 22.9 % to 9.00 %. The result of the thin film which is sputtered with $p_{Ar} = 8 \cdot 10^{-3}$ mbar cannot be evaluated because the calculation fails for surfaces without ditches or with less contrast difference between grains and ditches (like in Figure 34 (upper)).
The HR-SEM image at $p_{Ar} = 8 \cdot 10^{-3}$ mbar shows a drastic improvement of the surface morphology. No ditches appear and the surface is smoother than all other sputtered thin films before. The SEM cannot resolve the single grains which form the continuous film. The difference in height is too small for the detection with secondary electrons. Now, it is important to know which effect of the enumerated ones is the reason for such a thin film like in Figure 43 (lower). The increasing sputtering rate is definitely not the main reason, otherwise the measurements by variation of the current would cause more affect on the surface morphology. Either the faster target atoms or the directional sputter behaviour lead to this result. But the measurement method itself reaches its limits and does not yield much more information to characterise the texture-free film.

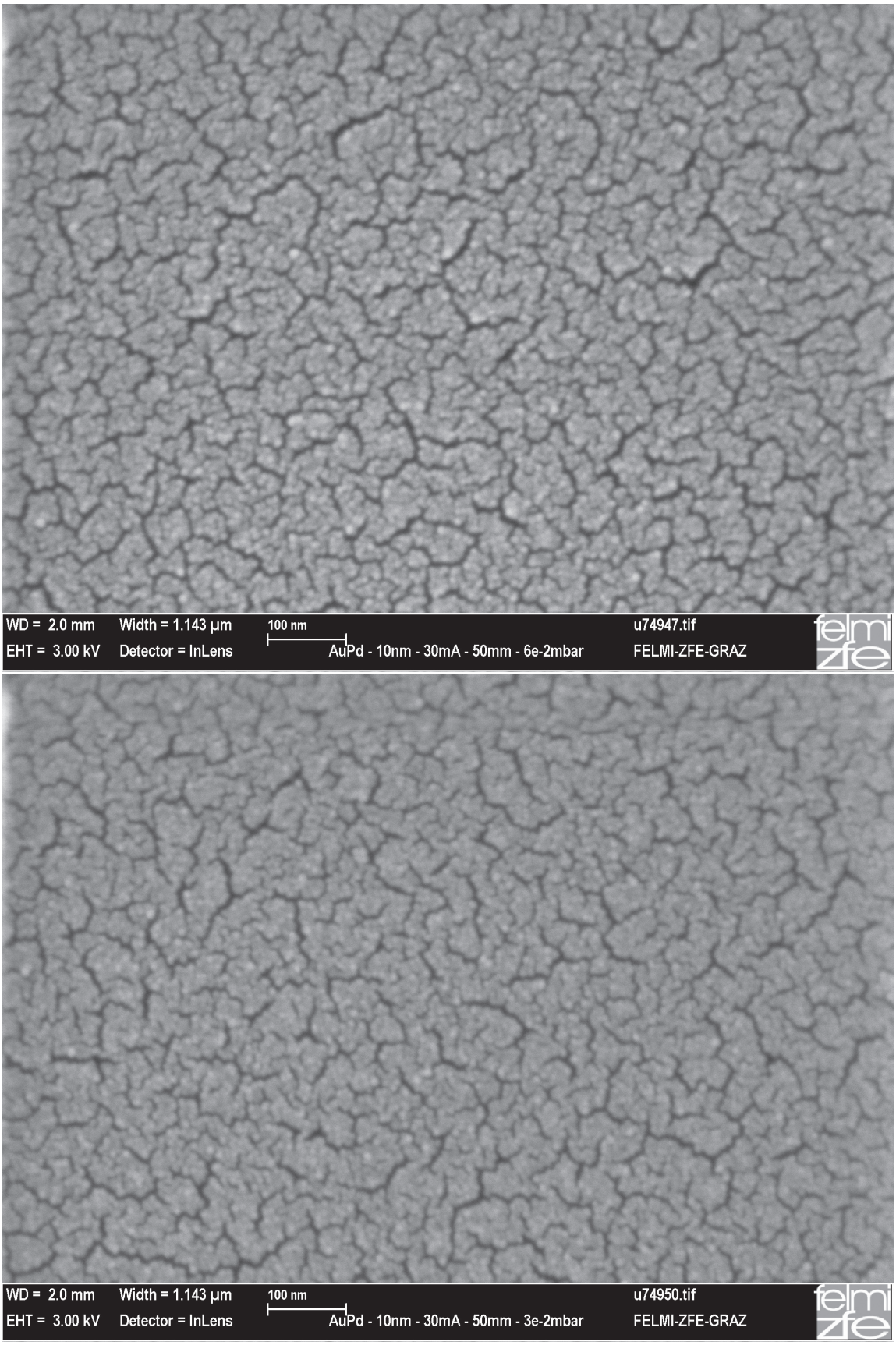

Figure 42: HR-SEM images (In-lens SE detector) with $100,000\times$ magnification. AuPd films sputtered with an argon pressure of $6 \cdot 10^{-2}$ mbar (upper) and $3 \cdot 10^{-2}$ mbar (lower).

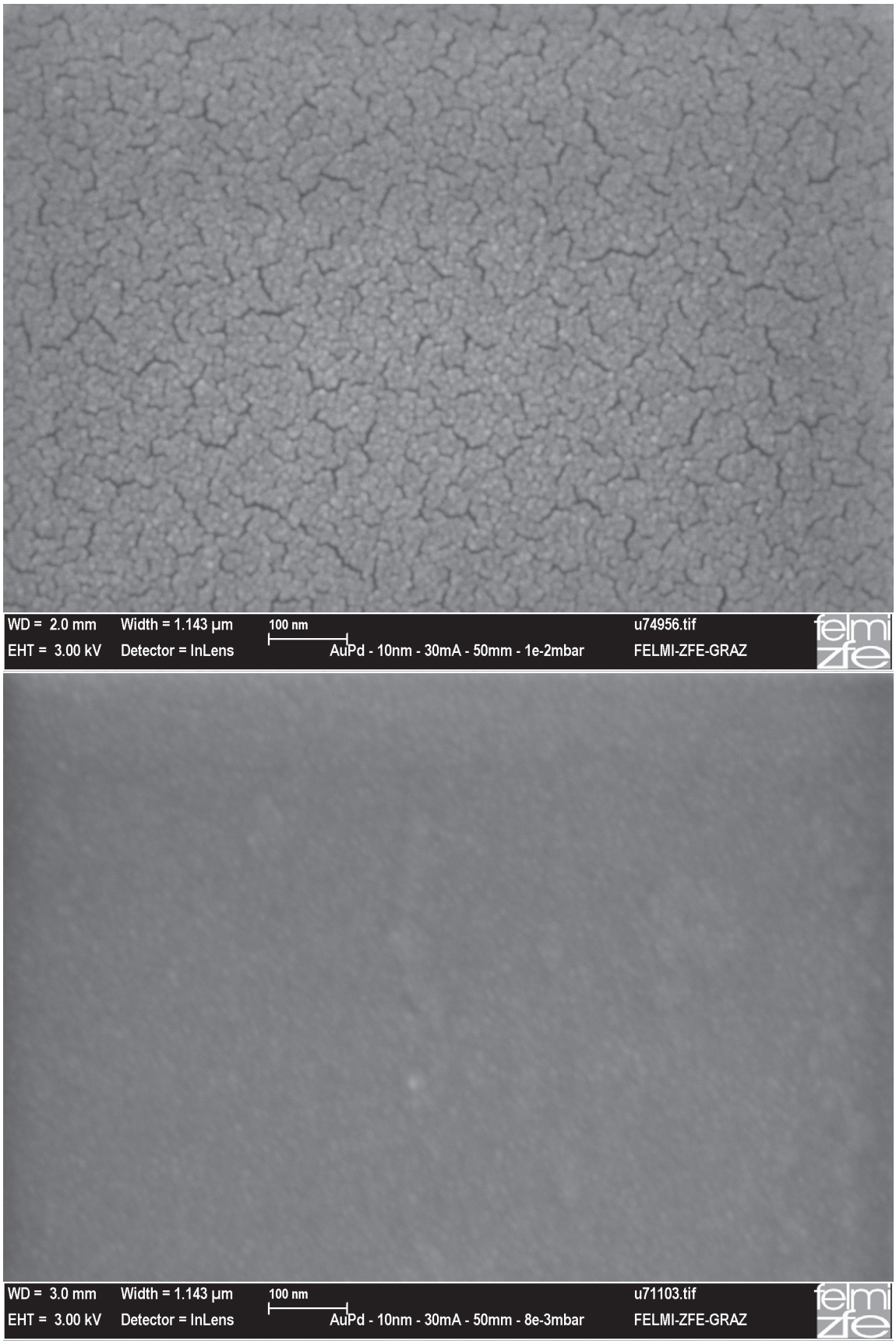

Figure 43: HR-SEM images (In-lens SE detector) with $100,000\times$ magnification. AuPd films sputtered with an argon pressure of $1 \cdot 10^{-2}$ mbar (upper) and $8 \cdot 10^{-3}$ mbar (lower).

5.5 SUBSTRATE

With the reduced argon pressure a metallic thin film free of ditches can be created. Now, a certain quality of the film is produced by a certain set of parameters. To get a statement about the usability the change of the quality of the film has to be investigated by changing some basic conditions like the substrate or the target material.
Before changing the target material, the effect of the surface morphology is observed by two methods. The first one is the HR-SEM, which was already used before, to characterise the surface structure and the resistance. The second method is the electron diffraction by the FEI Tecnai 12, a Transmission Electron Microscope. From this device, information about crystal orientation can be provided to find out a possibly preferred growth direction of the metallic crystal structure.
Several literatures which handle the growth of metallic thin films report of a substrate energy of crystalline substrates which forces thin films to grow along the same crystal orientation like the substrate consists of. A summery of this topic can be found in Section 2.4.
AuPd films with the same parameters of those in Figure 43 (lower) were examined with the HR-SEM. The difference between the measurements of Figure 43 and Figure 44 is that another substrates than silicon oxide was used - soda-lime glass and sodium chloride. Soda-lime glass is an amorphous material, as the name lets assume and sodium chloride is a crystal with preferred orientations of the crystallites. The typical NaCl crystal structure is a face centered cubic (fcc) lattice with a basis consisting of two atoms. Those preferred orientations which come from crystal are marked in Figure 45 (lower).As the images of the HR-SEM show, the surface smoothness retains and no further effect on the film growth can be seen. But to be sure, a second measurement was taken with the TEM. The substrates differ from the HR-SEM measurements because soda-lime glass or silicon oxide cannot be prepared to fulfil the recommendations for analysing samples with the TEM. The used transmission electron microscope was FEI Tecnai 12 for the diffraction patterns that is featured by an LaB_6 electron source at an acceleration voltage of $U_B = 120\,kV$ and reaches a point resolution of $0.34\,nm$. Instead of using soda-lime glass an ultra-thin electron transparent, amorphous polymer, called Formvar, was used for investigating metallic thin films grown on amorphous material in the TEM. The film can be sputtered directly on the polymer and no further preparation steps have to be done. The other substrate is NaCl. NaCl has the advantage that it is soluble in water. When the crystal is solved completely, just the metallic thin film swims on the surface of the water. The film is skimmed with a copper grid and is taken on the sample holder.
The resulting images of the HR-SEM measurement do not differ from the images of the thin films which are sputtered on a silicon oxide substrate, but the diffraction pattern shows a difference between both films. Obviously thin films which are sputtered on amorphous substrates have also amorphous behaviour during the growth process. Amorphous means, that all orientations of the crystallites are equally distributed along the planes perpendicular to the electron beam. The substrate energy of an amorphous material is as small as it could influence the growth process. In contrast, the diffraction pattern of the thin film which is sputtered on a NaCl shows a significant deviation from the amorphous diffraction pattern. Some certain crystal orientations are preferred. Those orientations which are depicted in Figure 45 stem from the NaCl crystal, although the NaCl crystal was completely dissolved in the water before the measurements began. The cause for this result is that a crystal like NaCl has enough energy to influence the growth process. However, the HR-SEM images of a thin film which is sputtered on a crystal looks the same like the thin film which is prepared on an amorphous substrate.

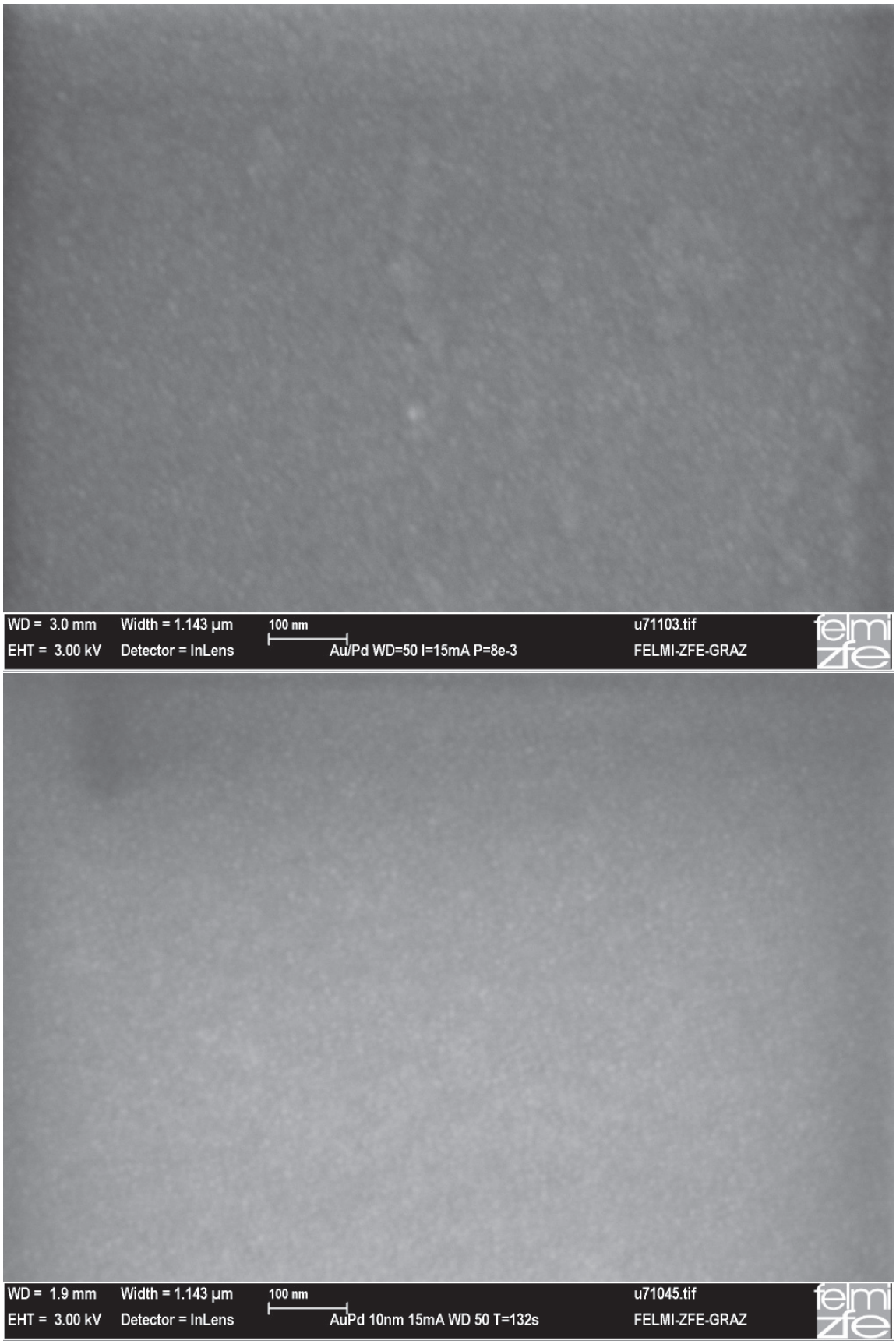

Figure 44: HR-SEM images (In-lens SE detector) with $100,000\times$ magnification. AuPd films sputtered with an argon pressure of $8 \cdot 10^{-3}$ mbar on a soda-lime glass (upper) and on a NaCl crystal (lower).

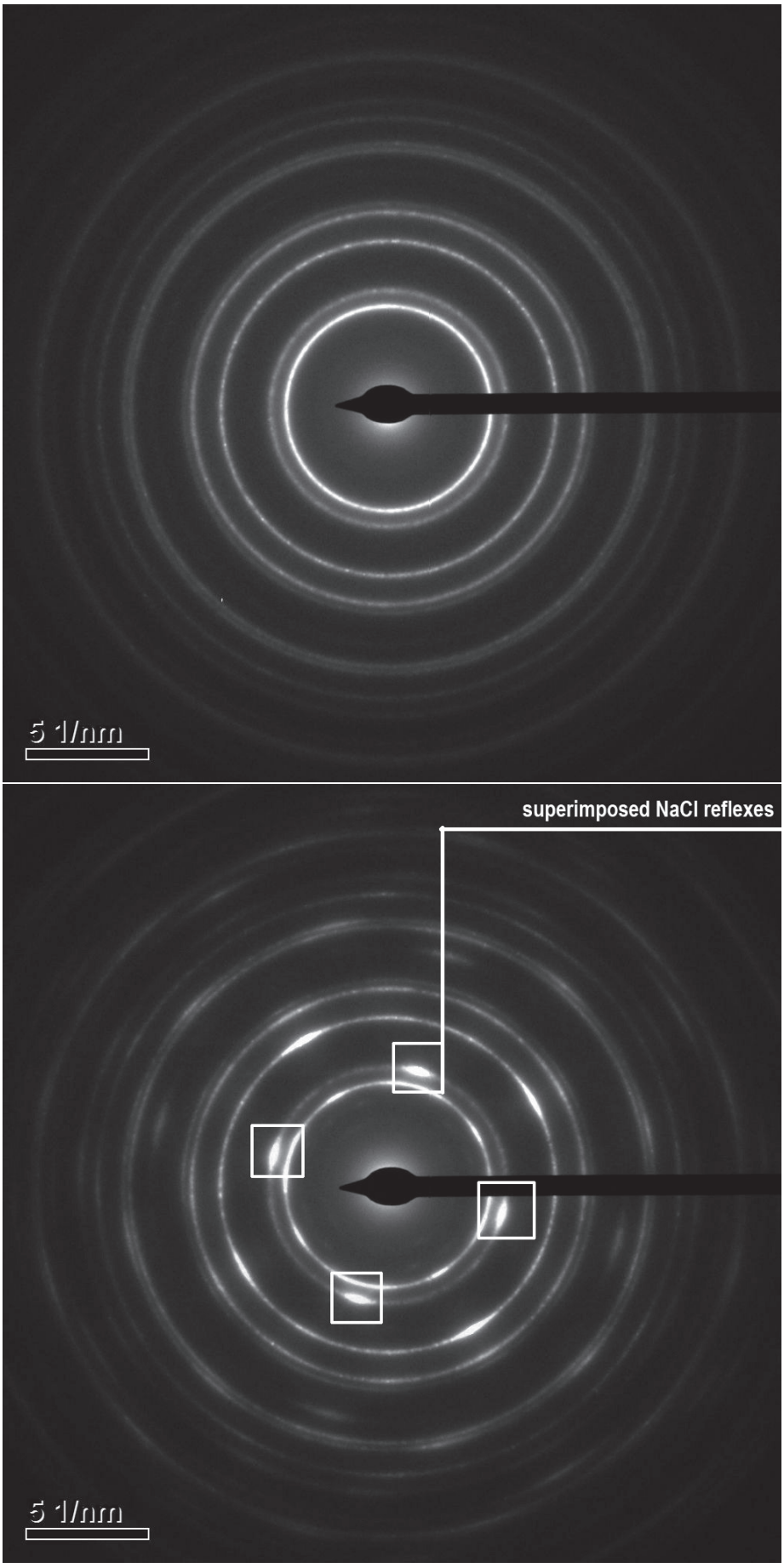

Figure 45: Electron diffraction pattern at $U_B = 120$ kV and Spotsize = 1. AuPd films sputtered with an argon pressure of $8 \cdot 10^{-3}$ mbar on Formvar (upper) and on a NaCl crystal (lower).

5.6 FURTHER ANALYSIS METHODS TO QUANTIFY DITCHES

During doing the first steps of the evaluation process to quantify such kind of structures a threshold technique of the image processing library of Matlab was used. The principle behind the threshold technique is described further in the Section 7.1 where this analytic tool was evaluated again for characterisation of island sizes. But setting an upper and lower limit of the ranges where ditches appear is quite subjective and depends strongly on the user who determines the boundaries of the ditches. Therefore, different characteristic lengths of the ditches will be detected which do not represent the real value.
Furthermore different contrast settings of the HR-SEM were investigated to reach greater contrasted ditches to get an image which can be further analysed by image processing tools like ImageJ [17] for detecting these ditches. Figure 46 shows the image of such kind of contrast settings. The white areas are the ditches which have to be characterised and all other contrasts are just inside a background signal, which ends up in black areas.

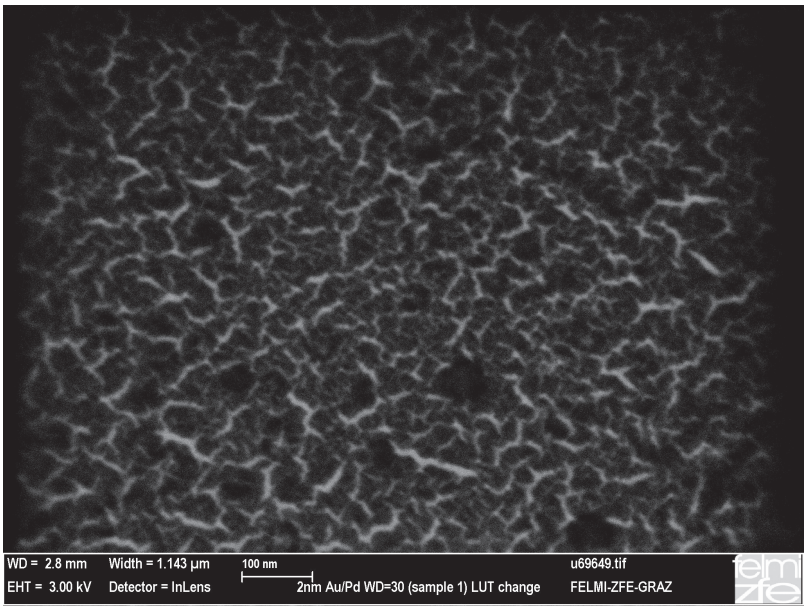

Figure 46: HR-SEM image where ditches are highlighted by adjusted contrast settings.

The result of this image is as subjective as the threshold technique before, because the range where ditches appear is not always the same contrast range for films with different sputtering settings. Another fact which limits this method is that the ditches have a fractal shape where a characteristic length is not easy to determine. A more precise look to the ditches in Figure 46 lets also assume that the length is probably randomly distributed, what makes a determination of one certain length more difficult.
In addition the power spectral density function (PSD) was evaluated, too. Further details of the PSD are written in Section 7.1, which especially deals with detailed information about different particle analysis procedures and algorithms. The result of the PSD function should be more objective than the methods described before, because there are no thresholds which have to be set to make the method work. But the result contains several peaks which could not be identified to the ditches and therefore no value could be found which represents the quality of the film.
Otherwise the number of ditches could give information about the quality of the continuity of the film surface, therefore the value which is expressed in percent in comparison to the whole area was chosen to quantify the quality of the film in Chapter 5.

6

CHARACTERISATION OF FILM GROWTH STAGES

After realising an continuously grown metallic film by decreasing the argon pressure, further experiments should lead to a deeper understanding of thin film growth stages. Investigations by increasing the thickness (see Section 5.1) showed that ditches are created from the beginning of the nucleation process and they keep staying at the end of the sputter process. Therefore, a closer look at the first seconds of the growth process is taken to consider possibly differences between the growth of both types of thin films - the highly structured film by ditches and the continuously grown film.
The analysis of such a kind of film which has not been nucleated to a conductive film poses a challenge. The need of high resolution is necessary to investigate differences in sub-nanometre-ranges, therefore the usage of electron microscopy cannot be avoided directly. In such a case, the HR-SEM does not reach the required resolution. Just the Transmission Electron Microscopes (TEM) can be taken into account because it yields the resolution as needed, also for less conductive samples, if the thickness is small enough and the charging effects are less than for HR-SEM.
The thin film is prepared like the samples for the experiment of the investigation of preferred crystallographic orientations sputtered on amorphous substrates. The amorphous substrate is given by a polymer which covers a TEM grid of copper, called Formvar. One of two sample is sputtered with the default parameters like in Table 1 and the other one is sputtered with the lowest argon pressure $p_{Ar} = 8 \cdot 10^{-3}$ mbar. The sputter process of both samples is stopped at certain thicknesses which are not measured with the build-in quartz, but the process ends after a certain time depending on the sputtering rate. This time is determined by a linear behaviour of the sputtering rate after a sputtering process of a 10-nanometer-thin film. The assumption of the linear relation is not 100 % accurate because the sputtering rate differs a lot in the first sub-seconds from the sputtering rate at the end of the process, but it suffices to compare the nearly same growth modes by different sputtering conditions.
The investigation was performed using the FEI Tecnai F20, with $U_B = 200$ kV and the results can be seen in Figure 47 to Figure 52. As written before, at very short sputtering times the comparison between films with different sputtering rates are quite difficult. With the assumption that both images in Figure 47 are in the same growth mode, the result shows a big difference between the film which is sputtered with highly structured thin film settings and settings which lead to a textured-free film. Although the sputtering time amounts just a few seconds. It can be seen that the number of adsorbed grains is higher on the right picture than on the left one. A precisely look at the grains shows also that the diameter of the grains on the right side (this film which results to a texture-free film) is smaller than the grains on the left image.

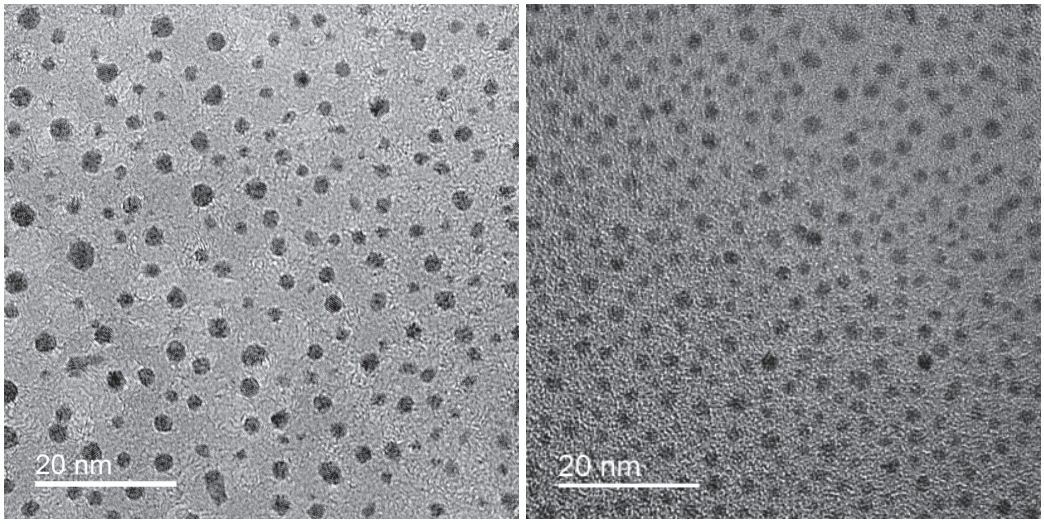

Figure 47: TEM images (bright-field) - AuPd films sputtered with $d < 0.25$ nm, $p_{Ar} = 5 \cdot 10^{-2}$ mbar (left) and $p_{Ar} = 8 \cdot 10^{-3}$ mbar (right) on Formvar.

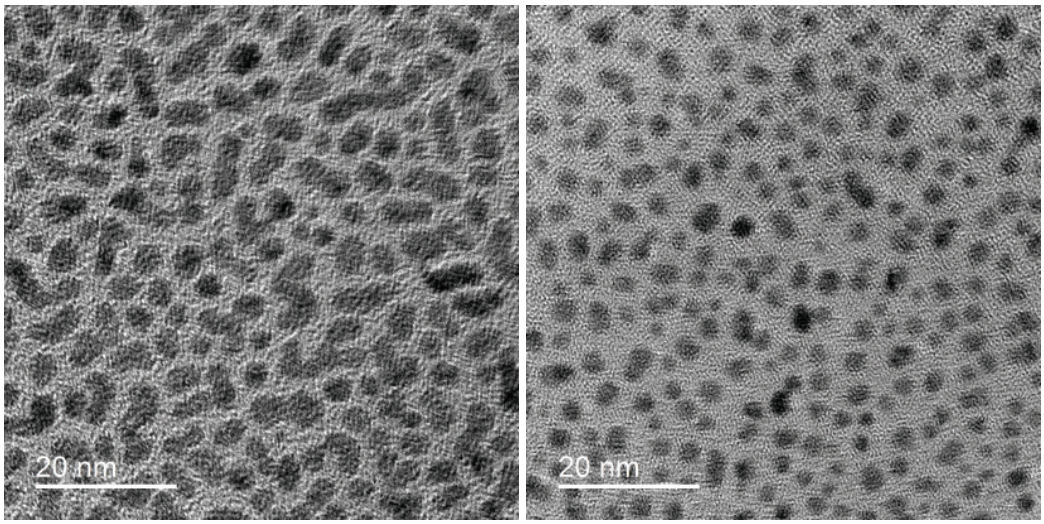

Figure 48: TEM images (bright-field) - AuPd films sputtered with $d = 0.25$ nm, $p_{Ar} = 5 \cdot 10^{-2}$ mbar (left) and $p_{Ar} = 8 \cdot 10^{-3}$ mbar (right) on Formvar.

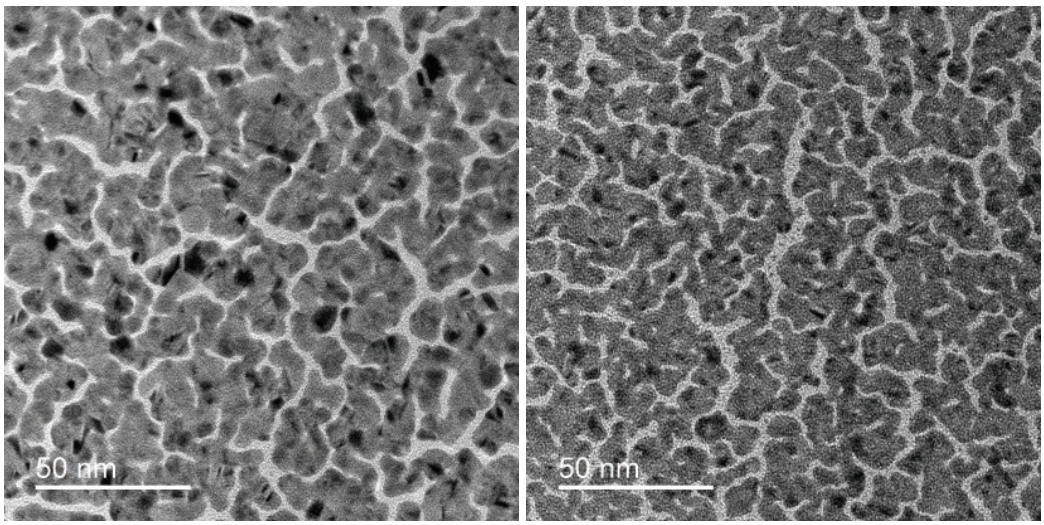

Figure 49: TEM images (bright-field) - AuPd films sputtered with $d = 1$ nm, $p_{Ar} = 5 \cdot 10^{-2}$ mbar (left) and $p_{Ar} = 8 \cdot 10^{-3}$ mbar (right) on Formvar.

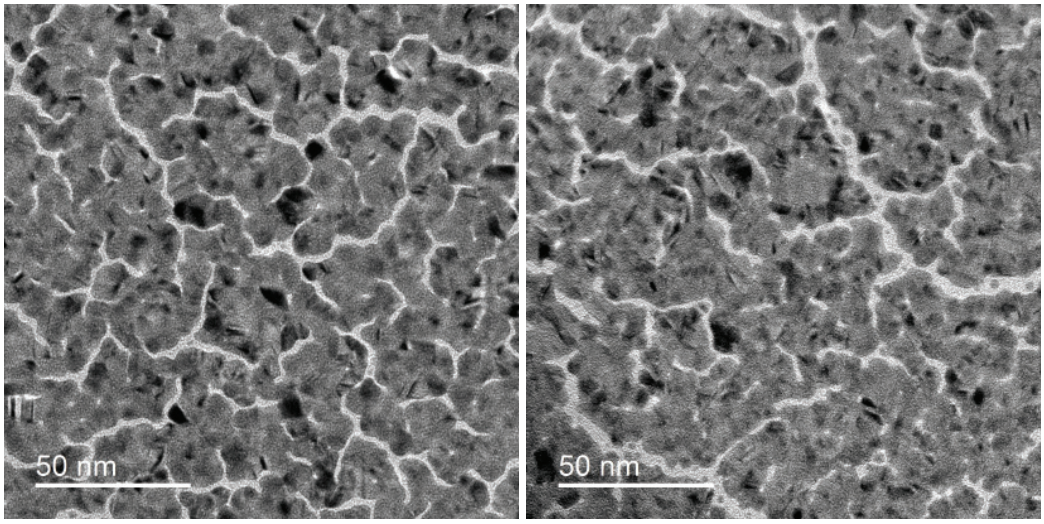

Figure 50: TEM images (bright-field) - AuPd films sputtered with $d = 1.5$ nm, $p_{Ar} = 5 \cdot 10^{-2}$ mbar (left) and $p_{Ar} = 8 \cdot 10^{-3}$ mbar (right) on Formvar.

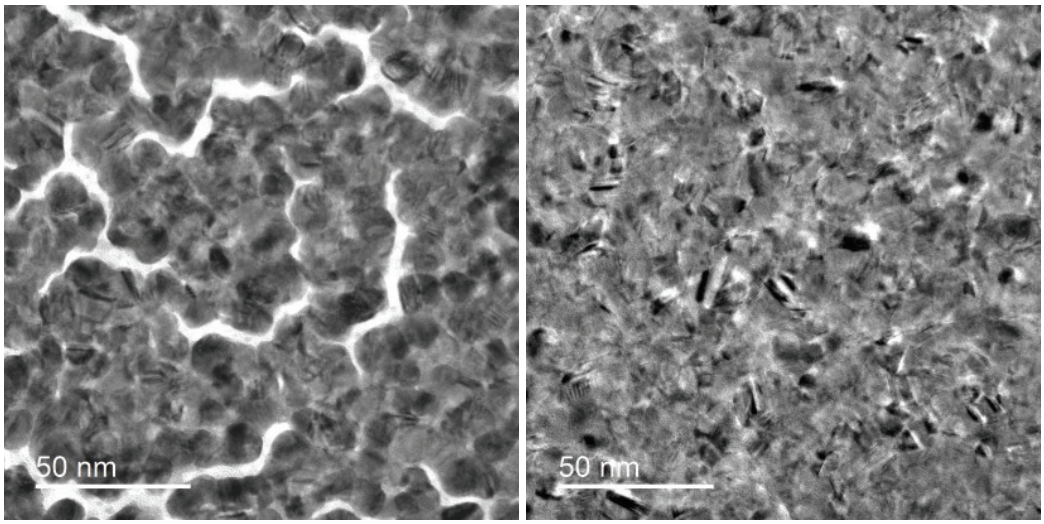

Figure 51: TEM images (bright-field) - AuPd films sputtered with $d = 5$ nm, $p_{Ar} = 5 \cdot 10^{-2}$ mbar (left) and $p_{Ar} = 8 \cdot 10^{-3}$ mbar (right) on Formvar.

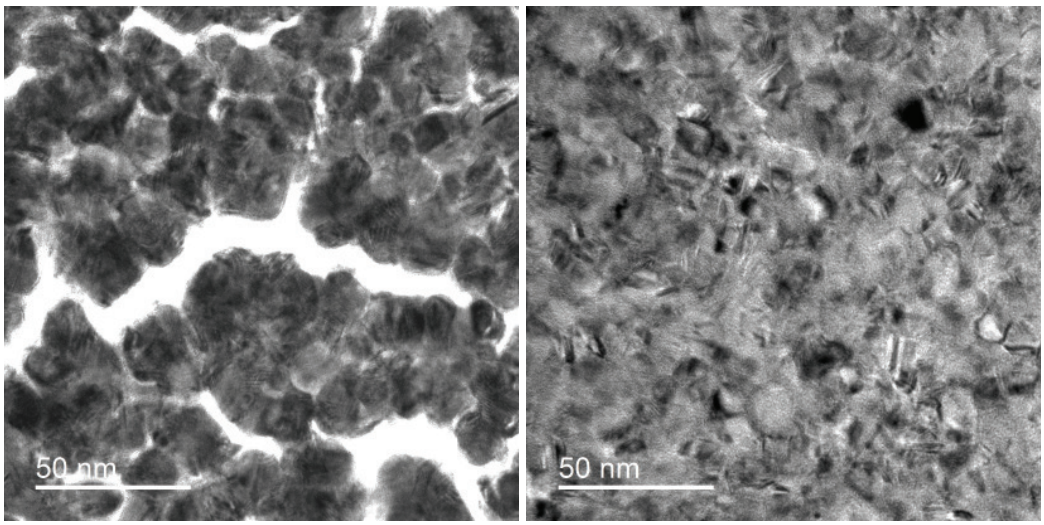

Figure 52: TEM images (bright-field) - AuPd films sputtered with $d = 10$ nm, $p_{Ar} = 5 \cdot 10^{-2}$ mbar (left) and $p_{Ar} = 8 \cdot 10^{-3}$ mbar (right) on Formvar.

The reason why the number of grains increases could be the higher sputtering rate due to the less argon pressure. Also the higher kinetic energy of the sputtered particle leads to more nucleation centres and therefore to a higher number of grains [33]. The consequences of these effects influence the further film growth. The next step of the growth process is the nucleation of the grains which reaches already the critical radius. The thin film which is sputtered with $p_{Ar} = 8 \cdot 10^{-3}$ mbar does not reach the critical radius shown in Figure 47 (right) because the size of the grains increases further which can be seen in Figure 48. On the other side, the grains of the thin film which are sputtered with $p_{Ar} = 5 \cdot 10^{-2}$ mbar lead to a highly textured film, grow together. They form agglomerates which include 3 to 4 single grains. Obviously the reduced sputtering rate forces the grains to prefer an extension of the capturing zone than to wait for incident particles to increase its grain size.
Afterwards both thin films with different sputtering conditions reach their critical grain size, the nucleation effect prevails and agglomerates are formed which include around 10 or more grains. Between the areas where grains grow together, there are channels which separate these regions. The growth mode at $d = 1\,nm$ occurs on both TEM images in Figure 49 and looks also similar to the other. Nevertheless one difference can be seen by taking a closer look to the ditches. In the ditches on the left image, no adatom or grain can be observed. In contrast, some growing up grains are found inside the ditches. This small difference seems to be the reason why the right thin film grows up to a continuously grown metallic film. Figure 50 shows the mode of the growth state some seconds apart from the image before. Small ditches disappear on both films, and the grains inside the ditches of the right image grow further until the film growth is finished at $d = 5\,nm$. Higher thickness values do not change the thin film which is sputtered with $p_{Ar} = 8 \cdot 10^{-3}$ mbar, but the comparison of the films which are sputtered with $p_{Ar} = 5 \cdot 10^{-2}$ mbar between $d = 5\,nm$ and $d = 10\,nm$ shows, that ditches expand but do not get filled - no matter how big the ditches are, no single adatom falls into them and forms a nucleation centre for a new grain.
Another statement out of this experiment can be made about the ditches. Images of the HR-SEM show the geometry of the ditches, too. But the height of the ditches could not be evaluated by analysing the hight distribution with 256 grey values. With the TEM images an exact value cannot be calculated out of the image either, because both tools are not made for this kind of analysis. But the TEM image has a major advantage through its transmitted behaviour. It can distinguish between ditches which are going through the whole cross-section of the film and ditches which have just passed the surface. Therefore, the image series shows that ditches arise from the first second of the sputter process and do not disappear at the end of the process if the settings of the argon pressure is too high.
Besides the TEM images, which show the different growth stages, the crystallographic behaviour of these films is investigated. The selected area electron diffraction (SAED) pattern leads to information about the orientation of the crystals. Like in Section 5.5, the NaCl reflexes were observed and could be assigned to the preparation method itself. Now, the film is sputtered on a neutral surface which does not influence the film during the sputter process. Therefore, a change of the SAED pattern would refer to a difference of the film growth due to the different sputter pressures. But Figure 53 does not show a difference. A homogeneous ring pattern means that the crystal orientations are uniformly distributed and no certain direction is preferred.
The comparison shows that the ring radii are always the same, thus the compound of AuPd does not distinguish from both sputtering process. Just the intensities which are greater than the first order between the left half of the merged images are different. This

can be explained by the fact that the ditches, which are areas without deflection, reduce the number of scattered electrons (especially for higher orders).

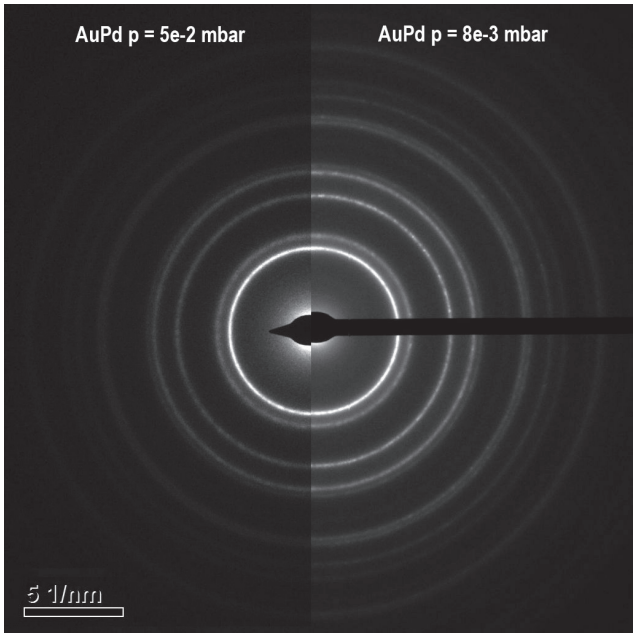

Figure 53: TEM electron diffraction images (SAED) of the last state of the growth process which is depicted in Figure 52. On the left side the diffraction pattern is shown of the film where ditches occur and on the right side the diffraction pattern of the ditches-free AuPd film can be seen.

This fact that no difference of the growth stages could imply that the formation of ditches is not a result of a chemical change or crystalline re-orientation. The reason is more likely based on the behaviour of the direction or the kinetic energy of the impinged target atom.
This analysis method with its high resolution is the ideal tool for observing the different growth states of a metallic thin film with small conductive behaviour. HR-SEM would not reach such a quality of images at this conditions. But even here, a precise characterisation of the continuously grown film is impossible to get a distribution for the grain sizes or other values which help to evaluate the quality of the film. Therefore, another method or analysis procedure has to be found to reach this goal.

7

CHARACTERISATION OF A CONTINUOUSLY GROWN METALLIC THIN FILM

A continuously grown metallic film grows in a reduced argon atmosphere. Investigations with SEM and TEM show the morphological behaviour and the difference of the growth between textured and non-textured metallic films, respectively. Both methods do not reach a resolution for measuring the dimension of an island on the surface of a film. Islands are compounds of grains which form agglomerates. Figure 44 and Figure 52 (right) depict the problem for the analysis to quantify the quality of the film. The contrast of the HR-SEM image is too weak for further image processing and the information from the orientation contrast of the TEM image is also too low to get a sufficient statistic for determining a quantity.
Another measurement method is evaluated to get such an information like an island size distribution - the atomic force microscopy (AFM). Bruker-Dimension FastScan Bio is used for characterising continuously grown metallic thin films. More details about the device is written in Section 2.5.2.
First, the pixel resolution and the range of interest have to be determined. Therefore, some measurements were performed with different scanning windows and pixel resolutions. For getting meaningful results at such small dimensions some aspects were considered and important for the further analysis procedures by image processing tools:

- pixelsize: The diameter of a single island is about 10 nm, for instance. To measure small deviation of the diameter the pixelsize has to be smaller than at least 0.5 nm to detect a change of the starting situation.
- islands per scanning window: More islands per scanning window lead to higher statistics which influence the error analysis of the resulting distribution positively.

But both quantities are limited and they are often contradictory. An image with a high number of islands by a high pixel resolution is very difficult to achieve, because the higher the number of pixels the higher is also the time which is needed per scanning line. Some fundamental effects like local thermal instabilities or rising wear of the AFM tips cause drift phenomena which result in distortion of the islands and influence the island distribution negatively.
Figure 54 shows such effects. The upper image is an AFM measurement at a scanning window of 1 µm × 1 µm by 2048 px × 2048 px. In contrast, the lower image is recorded by 250 nm × 250 nm and 1024 px × 1024 px. A 2D-Fast-Fourier-Transformation (FFT) figure for showing the symmetrical behaviour of the islands is inset in both images. Due to the long scanning time per line these fundamental effects occur in the upper image and make the measurement useless (the FFT is distorted along the vertical axis), although the statistic would be acceptable. The measurement setting of the lower image is also a bad choice because the number of depicted islands is too small to give a meaningful statement about general behaviours along the whole film, but the resulting drift effect is small enough and can be neglected because the circular form of the FFT means that the islands are not distorted strongly. Another reason for changing the settings is that the signal to noise ratio becomes smaller at such a small scanning window and worsens the image quality. Therefore a compromise has to be made for getting a statistically significant statement at an acceptable resolution.

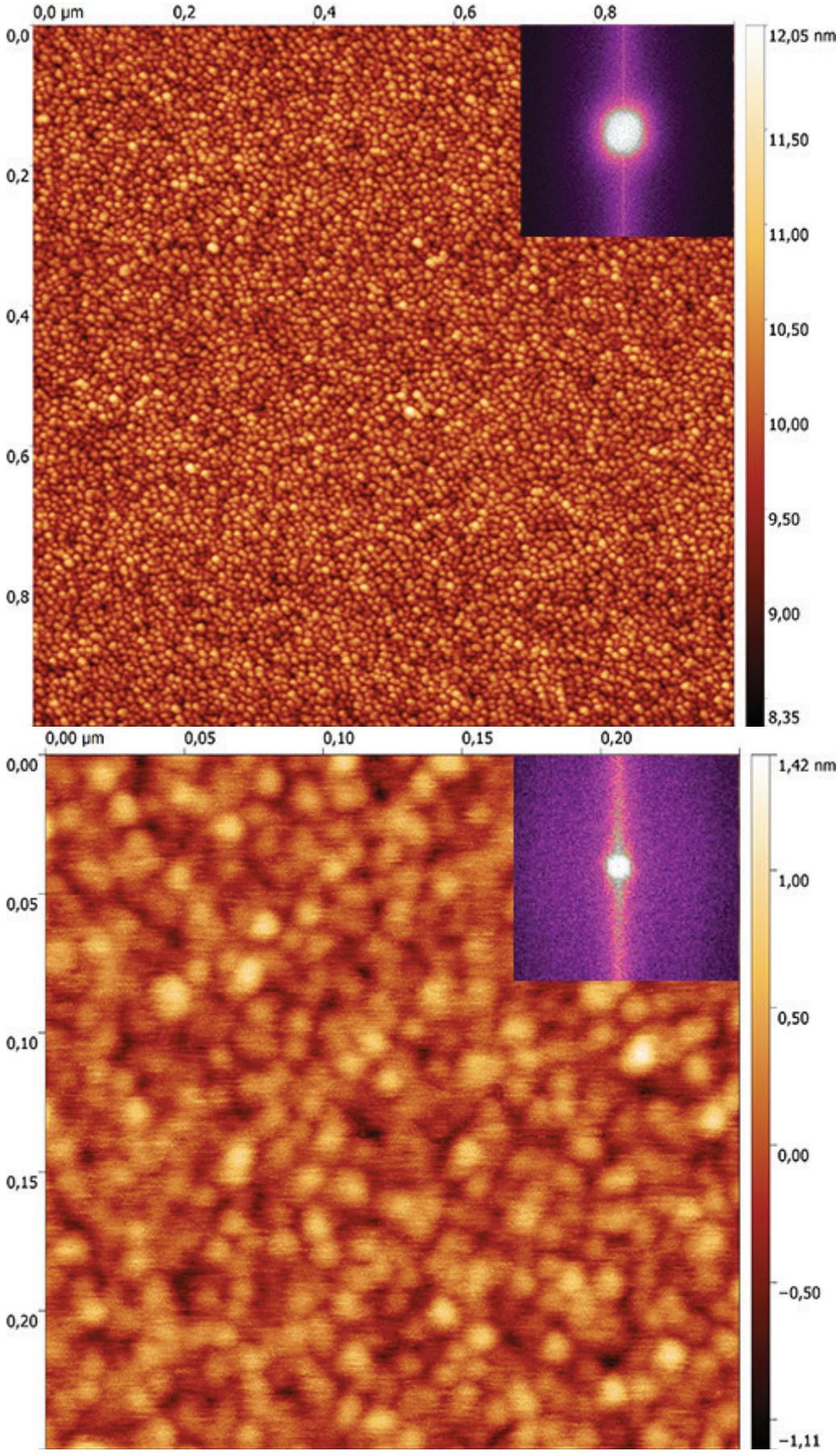

Figure 54: AFM images of a 10-nanometre-thin, texture-free AuPd film with different scanning parameters. Upper image shows a image resolution of 2048 px × 2048 px and the lower image has a resolution of 1024 px × 1024 px

A good choice for this is an image with a scanning window of 500 nm × 500 nm by 1024 px × 1024 px, which is shown in Figure 55. The lateral length of one pixel is approximately about 0.5 nm. The mentioned effects before, which influence the quality of the image negatively, are quite small in comparison to all other resolutions and the statistic of about more than hundreds of islands suffices to give a general statement.

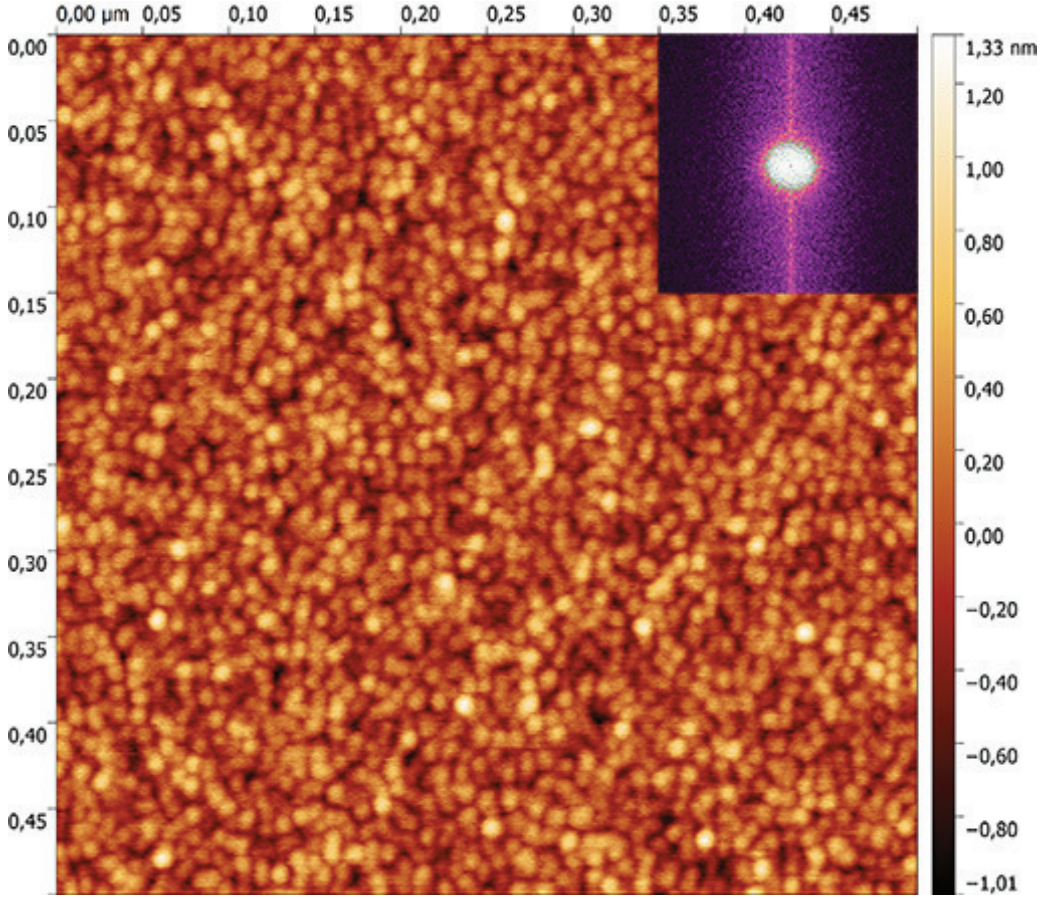

Figure 55: AFM images of a 10-nanometre-thin, texture-free AuPd film with a scanning window of 500 nm × 500 nm and a resolution of of 1024 px × 1024 px

The inset FFT image shows no certain preferred orientation except the vertical line which refers to the scanning direction of the AFM measurement. A circular pattern of the FFT is caused by a nearly distortion-free scan of a surface. Often small distortions are not avoidable due to a small amount of wear of the tip and have to be taken into account by the error analysis. But in general, the mathematical formalism of an AFM image is represented by a convolution of the object that has to be measured and the needle tip. Therefore, a tip which is much bigger than the smallest artefact of the sample does not collect all details. And otherwise the real value of an object cannot be measured directly without a deconvolution correction.

7.1 PARTICLE ANALYSIS

There are several methods for determining dimensions of islands. Whereas determinations of island sizes of polymers are managed much easier because they have a large distance between their neighbours. Determination of a continuously grown thin film is quite challenging for image processing tools. Particle analysis out of SEM or TEM images are mostly impossible because the resolution of the z-axis is mostly too less to separate one single island of a whole cluster, although the lateral resolution would suffice.

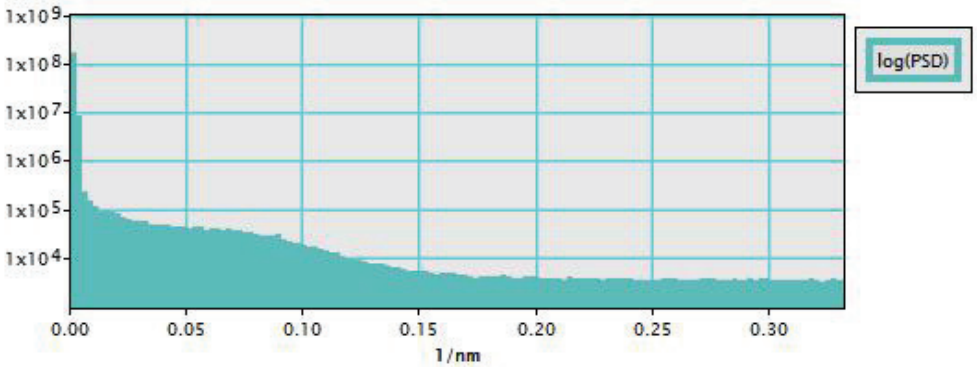

Figure 56: Logarithmic power spectral density function of HR-SEM image which can be seen in Figure 44 (lower).

The SEM images were analysed by the power spectral density function (PSD), for instance, which is often used in the AFM measurements to compare morphological parameters of the observed films [9], [26]. Films with surfaces like in the HR-SEM images of Figure 44 were used for evaluation the PSD to quantify islands. PSD can be written as the Fourier transformation of the autocorrelation function [6] and yields information about roughness and correlation length. There are existing several models like the Gaussian model or the ABC of k-correlation model to get out parameters depending on the shape of the PSD.

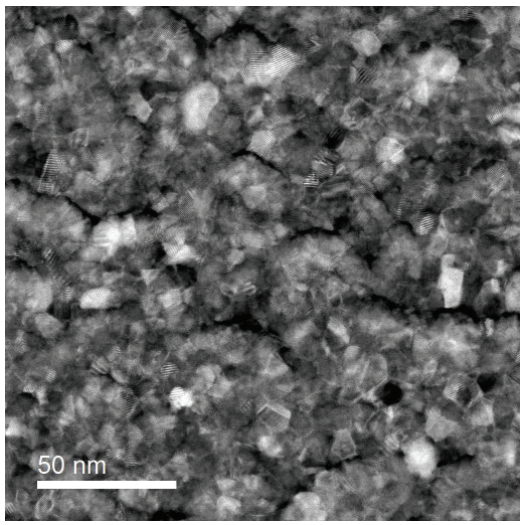

Figure 57: TEM darkfield image of an metallic film like Figure 44 shows.

In Figure 44 (lower) a high resolution image of a gold-palladium film is depicted, some islands can be seen clearly and the PSD function was used to quantify these islands (like in Section 5.6 to quantify the ditches) which is shown in Figure 56.
The first part in the low frequency range of the PSD should include several maxima of

the most likely occurring island sizes. But there is a spread shoulder of values which cannot be identified as a distribution of sizes.
The TEM image would lead to bigger contrast of an island, at least more contrast than a SEM image of the gold-palladium film. Figure Figure 57 shows a darkfield image of the same thin film of Figure 44, which is measured with the SEM. The reason of the resulting contrast occurs from a different physical cause than in the SEM. Regions with the same grey value are crystallites with the same crystal orientation. To quantify the islands this regions are of special interest. But the boundaries to the neighbour islands are too weak to separate single ones from the neighbourhood. No image processing tool can handle this image to get information about sizes. The shape is also different than in the SEM. They look like more cornered than in the SEM where the islands can be assumed as round objects.
Therefore the AFM measurement method would be evaluated for characterising metallic thin films. It has a lot of advantages in comparison to the already observed methods. One of these is the high z-resolution that is depicted in Figure 55. Single islands inside the agglomeration can be easier separated as for other measurement methods. But it remains a challenge.
A quantification of island distribution is necessary to evaluate the optimum sputter parameters and the best sputter target for HR-SEM.

7.1.1 *Threshold*

The threshold method is a very simple technique to separate islands from underground. If the islands are far apart from each other and the height difference between underground and island is big, this method will apply. The detection of island boundaries is made by setting of threshold at a certain slope value, height value or a certain curvature. But if the distance between the island is as close as in Figure 55 and the islands are also flat, the result of a particle analysis by threshold techniques is insufficient because the technique comes close to its limits.
The island size would depend on the threshold which would be set. Therefore, a meaningful statement of the real island size distribution cannot be expected by this analysis method.

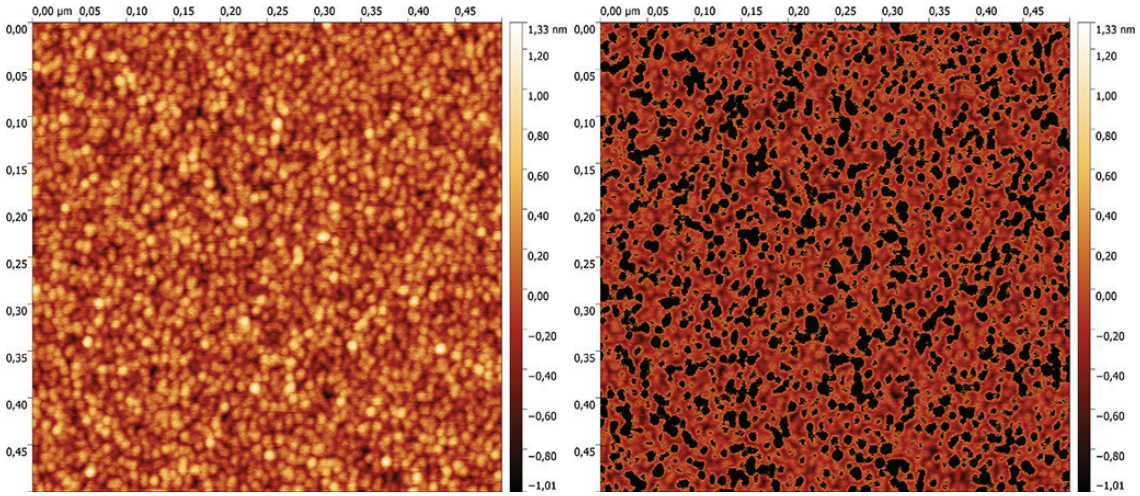

Figure 58: Detection of single islands by threshold techniques. Left image is the origin AFM measurement and the black areas at the right image depict the detected islands.

The problem with detection of islands within a continuously grown film is depicted in Figure 58. The detection of the islands is made by setting a threshold value for the height. The relative height value is set to $h_{th} = 49.4\,\%$, all height values above h_{th} are taken for the detection of an island. A lower value cannot be used because it would cause just a detection of noise. Additional setting for curvature and slope does not lead to a better detection either.

7.1.2 *Watershed*

The watershed algorithm [3] is more complex than the threshold technique. Therefore, the results are more valuable, too. The watershed particle analysis is part of the used AFM analysis software tool Gwyddion [25]. This algorithm is divided into two phases. The island location phase and the segmentation phase. During the island location phase the algorithm is looking for local minima (in the case of an AFM image, the detection of local maxima is mainly used) by placing a virtual water droplet on the surface. The size of the droplet can be set by the parameter *drop size*. As soon as the droplet found a local minimum (minimum of its potential energy), it rests on this position on the surface. This procedure can be repeated several times, which is controlled by the parameter *number of steps*. Afterwards the image consists of small lakes. The smallest lakes (set by the parameter *threshold*) can also be removed to reduce the detection of noise peaks.
The location phase is finished and the segmentation phase begins by setting a new *drop size* and a new value at *number of steps*. The located islands are filled with droplets further until the number of steps is reached. If a droplet falls on a region where more than one island is located, the position is marked as island boundary. Otherwise if just one island is located at a position where the droplet falls down, the droplet is associated to this island. The last case, which is important for the understanding of the algorithm, is that a droplet falls down at a position where no island is located and also no island can be found in the neighbourhood of this position. Then the droplet is rejected by the algorithm.

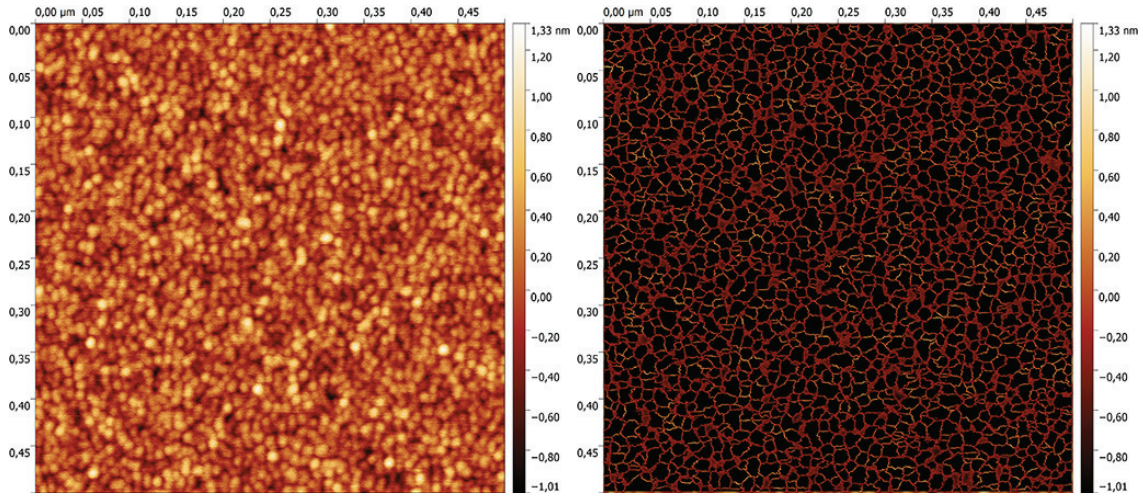

Figure 59: Detection of single islands by watershed technique. Left image is the origin AFM measurement and the black areas at the right image depict the detected islands.

In comparison to the threshold technique the parameter settings of the watershed algorithm are chosen less subjectively. All following analysis for AuPd were done with the same settings. This procedure is nearly impossible for the threshold technique. The difference is that the upper or lower limit of the peaks which are detected by the AFM

Table 9: Parameters of the watershed algorithm for AuPd films

island location	
number of steps	10
drop size	3.71 %
threshold	26 px^2
separation	
number of steps	198
drop size	3.71 %

are individual for every measured surface.
The resulting particle analysis is shown in Figure 59 (right). The number of detected islands increases significantly in comparison to the threshold technique. The used parameter for droplet size, number of steps and the threshold are improved by variation of all parameters to get the maximal value for the number of detected islands. The resulting values for the parameter of the watershed method which is used for AuPd films are tabulated in Table 9.
The value for *threshold* is set to 26 px^2 and it is not varied. The reason for choosing the value is based on the assumption that a perfect island depicts a circle on the horizontal projection. 26 px^2 corresponds to a circle area with the radius of $r = 1.4\,\text{nm}$. The radius of the islands which are assumed for AuPd is around $r_{AuPd} = 6\,\text{nm}$, therefore the lower limit for detection of a single island is an island with $r_{i,min} = 1.4\,\text{nm}$. All islands which have dimensions less than $r_{i,min}$ are assigned to noise.

7.1.3 *Radial Autocorrelation Function*

Fekete et al. [7] described the determination of size distributions of nanoparticles which surface is measured with the AFM. They used the radial autocorrelation function (rACF) to generate a lateral size distribution depending on the slope, zero-crossing and the shape of the rACF. In the report the method is described and evaluated for densely packed nanoparticles of which sizes are between 20 nm and 1.5 µm. In general, the 2D-ACF is defined as $ACF\{h(x,y)\}(\Delta x,\Delta y) = \langle\langle h(x+\Delta x, y+\Delta y)h(x,y)\rangle\rangle$ and an example is depicted in Figure 60 (left). All relevant information of the measured film is located between the centre $(0,0)$ and the first minimum of the 2D-ACF. If the studied objects are radial symmetric the 2D-ACF can be transformed to polar coordinates $(\Delta x,\Delta y) \rightarrow \Delta R, \Delta\varphi$. Then the 2D-ACF will be summed up over all angles to project the 2D problem to one dimension. The rACF is then defined as $rACF\{h(r,\varphi)\}(\Delta r) = \int_0^{2\pi} ACF\{h(x,y)\}(\Delta r,\Delta\varphi)\,d(\Delta\varphi)$. To not get too deep into the mathematical formalism the theoretical part ends here and the practical usage is now described further.
Without further calculations Fekete et al. [7] defined a rule of thumb for the first estimation of the mean island size value. This expression depends on the inflection point of the rACF Δr_{ip} and is defined as

$$d_{mean} = 2.6 \times \Delta r_{ip}\ . \tag{16}$$

For getting out the lateral size distribution the following algorithm has to be performed:

- Measuring the topography of the object which has to be studied by using AFM. Thereby several requirements have to be fulfilled for applying the determination of the lateral size distribution by the ACF technique. First, the AFM image has to have

a pixelsize which is small enough to get enough pixels per islands. Then the mean height of the whole image have to be zero (image flattening). And no artefacts (like thermal drifts, effects of tip sizes, contaminations) may be present.

- Calculating the rADF out of the radial symmetric 2D-ACF
- A range of diameters has to be set for generating a model histogram. A good initial guess for determining the range of the histogram will be the d_{mean}, which is introduced above.
- Using a least-square fitting procedure between the deviation of the model histogram and the measured rACF. With the values of the fit parameters the distribution of sizes can be calculated.

A model rACF is defined by a function which is called modified Chinese Hat Function (modChat) and represents the shape of the main part of the rACF. To get a histogram out of the result of the fitting procedure the distribution of sizes has to be roughly estimated before the fitting can be done. The final least-square fit shows the accordance between model and reality.

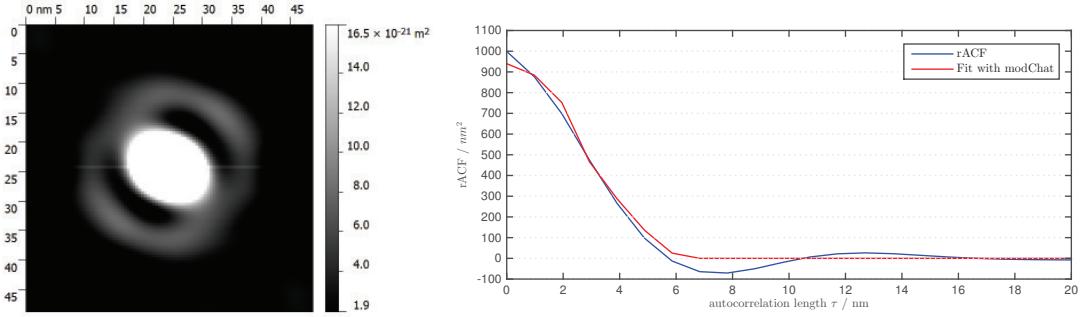

Figure 60: A 2D-ACF (left) and the rACF (right) with the fitted modChat function of a continuously grown thin AuPd film. Besides distortion effects, a minimum of the rACF below zero is detected and leads to less applicability of the method.

Several calculations and measurements were done to evaluate this technique on the topography of continuously grown metallic thin films. But the calculation out of the rACF did not fit to the present surfaces. Even the rough estimation calculation does not lead to the expected values. The problem was isolated to the AFM measurement. The smallest mean value of the islands of the presented method by Fekete [7] is 20 nm but the island sizes of the studied AuPd film is approximately around the half dimension. Therefore, an AFM measurement with the sufficient resolution is necessary to lead to success with this method. The effects of thermal drifts and the influence of the tip increase by decreasing dimensions of the islands, what is definitely the reason why no radial symmetrically 2D-ACF can be produced. In correspondence to the lead author of this report, another effect was found to get an explanation why the method failed. Besides the asymmetric behaviour of the 2D-ACF which is depicted in Figure 60 (left), the resulted rACF shows the first minimum below zero. This behaviour is an indication that there will be no correlation to the island dimensions and the rACF fitted with the modChat function. Fekete is working on this problem by applying several torque function to a new model rACF to get a size distribution out of methods with lower lateral resolutions like SEM, for instance [31]. But in the meanwhile the determination of island size distribution with the rACF is not applicable on thin films which means that the island size is lower than 20 nm.

7.2 PARTICLE ANALYSIS BY VARIATION OF THE WORKING DISTANCE

It was already observed that the argon pressure influences the growth behaviour. A compact growth can be reached in a reduced argon atmosphere. Other parameters like working distance or current have no significant effect on the morphology and the growth process, which is shown in Chapter 5. The effect of these parameters on a continuously grown film is investigated by atomic force microscopy and numerical analysis based on the watershed algorithm in this chapter.
The parameters which are used for sputtering the metallic thin film are depicted in Table 10.

Table 10: Sputtering parameters for varying the working distance by a continuously grown film

sputter current $I_{sputter}$	[mA]	30	working distance WD	[mm]	30, 45, 60, 75, 90
pre-vacuum $p_{pre-vac}$	[mbar]	$8e-5$	sputter-vacuum p_{Ar}	[mbar]	$8e-3$
rotation rot	[-]	3	tilt t	[–]	0
thickness d	[nm]	10			
substrate material	[–]	silicon	target material	[–]	AuPd

No big differences of the dimensions were expected, therefore a precise analysis and a precise handling of the devices are necessary for getting a meaningful result. The dimensions of a single island of AuPd is also measured manually because it is better to know about the conditions at the beginning of the measurement before the numerical analysis starts. The resulting island radius of a AuPd sample, sputtered with the parameters of Table 10, is tabulated and compared in Table 11. But a manual determination of an island diameter is not an efficient way and costs a lot of time for getting a result which depends also on the exactness of the user, therefore a numerical island size analysis is performed additionally.
The algorithm is described in the section before. If the choice of the parameter for the algorithm is done well, the identification of the islands is as good as in Figure 59 (right). Now, three radii can be extracted:

- mean radius: This radius is referred to the center of gravity, all radii to the boundaries of the island are arithmetically averaged.
- minimum circumcircle radius: As the name lets assume, a circumcircle is fitted on a single island and the radius with the smallest circumcircle counts. Figure 61 (right) shows an island with a drawn circumcircle.
- maximum inscribed radius: The radius of the biggest circle which fits inside the island. Figure 61 (left) depicts an island with an inscribed circle.

A horizontal projection of an ideal island has the shape of a circle and all three radii would have the same value. The projection of a real island does not have to be a circle. Therefore, all three values are observed during the analysis to get an idea which shape is preferred by a AuPd alloy.
Out of the detected islands, an island size distribution is generated and is repeated for each thin film with varied working distances. The island size distribution for each radius is fitted by a Gaussian curve and compared amongst themselves. The resulting values are shown in Table 11.
Besides the island size analysis, information about the height values of the islands are of special interest. Therefore, the arithmetic mean roughness parameter R_a and the average

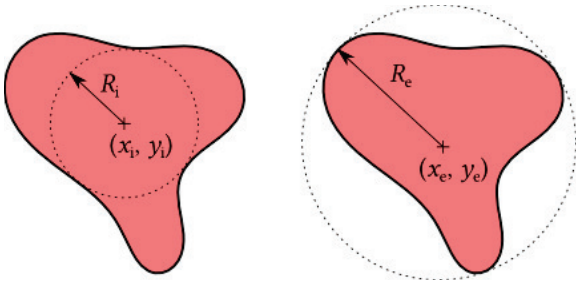

Figure 61: An island which is quantified by a maximum inscribed radius (left) and an island quantified by a minimum circumcircle radius (right). [24]

depth of roughness parameter R_Z of the whole AFM topographic image are taken to extract the height information of the measured surface. R_a is defined as

$$R_a = \frac{1}{n}\sum_{i=1}^{n}|y_i| \tag{17}$$

where $|y_i|$ is the surface profile height of the measured topographical image at the i-th position and is an ISO standard which refers to ISO 4287-1997. R_Z defines the arithmetic mean of the distance between the five highest maxima and the five lowest minima (Y_i) per evaluation length (in this case a single scanning line) and is also a part of the ISO standard of ISO 4287-1997.

$$R_Z = \frac{1}{5}\sum_{i=5}^{n}|Y_i| \tag{18}$$

If both values are the same, the sample is nearly flat. Otherwise R_Z depicts a value of the averaged height of the detected islands. These values are shown and compared in the following table:

Table 11: Resulting island dimensions of a continuously grown AuPd film by variation of the working distance

current	30 mA	argon pressure	$8e-3$ mbar	thickness 10 nm
WD / mm	$r_{mean,\,wat}$ / nm	$r_{min,\,circ}$ / nm	$r_{max,\,insc}$	$r_{mean,man} \pm \Delta r$ / nm
30	6.1	8.0	4.4	5.9 ± 2.1
45	6.2	8.2	4.3	6.1 ± 1.7
60	5.8	7.8	4.0	6.4 ± 1.6
75	5.8	7.6	4.1	6.2 ± 1.7
90	5.6	7.4	5.0	6.0 ± 1.7
WD / mm	$R_a \pm \Delta R_a$ / nm	$R_Z \pm \Delta R_Z$ / nm		
30	0.23 ± 0.02	1.3 ± 0.1		
45	0.23 ± 0.02	1.2 ± 0.1		
60	0.23 ± 0.03	1.1 ± 0.1		
75	0.28 ± 0.03	1.4 ± 0.1		
90	0.26 ± 0.03	1.4 ± 0.1		
		$\bar{r}_{mean,\,wat}$	(5.9 ± 0.3) nm	
		$\bar{r}_{mean,\,man}$	(6.1 ± 1.8) nm	
		$R_{a,mean}$	(0.25 ± 0.03) nm	
		$R_{Z,mean}$	(1.3 ± 0.1) nm	

Regarding to the values of the radii by increasing the working distance, all radii are slightly falling down and the height tends to increase. The difference is in the sub-nanometre range and the analysis method by the watershed algorithm undertakes an error which is greater than 0.5 nm, therefore it is no meaningful statement but a small tendency can be assumed. Therefore, the analysis is compared by the results of the manually measured evaluation of the island sizes. At this analysis hundred different islands are measured to get a mean island radius and the the errors are calculated from the standard deviation. Due to the high errors of both methods, no significant tendency can be observed.
Another fact is that the different radii which can be extracted from the image processing analysis by the watershed algorithm have a difference between 1 to 2 nm, which would be regarded as a non circular behaviour of the island. But in this case the deviant tend to be an artefact of an error-prone analysis, where the detection of non-separated islands is taken into account.
Out of this analysis an averaged radius (from the data of the watershed and of the manually done measurement) and an averaged R_Z over all working distances are generated and amount to

$$\bar{r}_{\text{mean, AuPd}} = (6.0 \pm 1.8)\,\text{nm and } R_{Z,\text{mean, AuPd}} = (1.3 \pm 0.1)\ \text{nm}. \tag{19}$$

The roughness values which are extracted from the AFM measurements cannot be identified directly to the height values of the islands which are formed on the surface of metallic films. This is caused by the finite tip diameter of the AFM needles and the surface of the metal films does not form separated islands. These islands grow together and make the evaluation of the island height and also of the lateral dimensions quite difficult. But the combination of the roughness parameters R_a and R_Z is a good choice for estimating the height value which is a property of a high quality thin film for HR-SEM.

7.3 PARTICLE ANALYSIS BY VARIATION OF THE CURRENT

The same measurements are performed by increasing the current of the Leica sputter coater from 15 mA to 115 mA in five steps at a working distance of WD = 50 mm. The resulting AFM images evaluated with the human eyes look similar to Figure 59, therefore no significant difference is expected. The islands are detected by the watershed algorithm. They are evaluated by the histogram of the island size distribution and manually. A summary of all values are depicted in Table 12.

Table 12: Resulting island dimensions of a continuously grown, AuPd film by variation of the set current

Working distance	50 mm	argon pressure	$8e-3$ mbar	thickness 10 nm
I / mA	$r_{mean,\,wat}$ / nm	$r_{min,\,circ}$ / nm	$r_{max,\,insc}$	$r_{mean,man} \pm \Delta r$ / nm
15	5.4	7.3	3.7	6.1 ± 1.7
40	5.5	7.2	4.0	5.9 ± 1.8
65	5.4	7.5	3.5	6.2 ± 1.6
90	5.6	7.3	3.9	5.9 ± 1.9
115	5.9	8.3	3.5	6.1 ± 1.7
I / mA	$R_a \pm \Delta R_a$ / nm	$R_Z \pm \Delta R_Z$ / nm		
15	0.24 ± 0.02	1.2 ± 0.1		
40	0.24 ± 0.02	1.3 ± 0.1		
65	0.23 ± 0.02	1.2 ± 0.1		
90	0.28 ± 0.03	1.3 ± 0.1		
115	0.19 ± 0.03	0.9 ± 0.1		
		$\bar{r}_{mean,\,wat}$	(5.6 ± 0.2) nm	
		$\bar{r}_{mean,\,man}$	(6.1 ± 1.7) nm	
		$R_{a,mean}$	(0.24 ± 0.2) nm	
		$R_{Z,mean}$	(1.2 ± 0.1) nm	

The results shown in Table 12 do not differ significantly from the results of the measurement before. Just the evaluated radii and also the height value processed with a sputter current of 115 mA vary more than all other values. In contrast to the measurement before, a really slight tendency for an increasing of the radius of the islands could be recognized by the watershed evaluation, however, the tendency is inside the error of the measurement. Thus, the values are used to determine an averaged island radius and an averaged island height. The results are given below:

$$\bar{r}_{mean,\,AuPd} = (5.8 \pm 1.7)\,\text{nm} \text{ and } R_{Z,mean,\,AuPd} = (1.2 \pm 0.1)\,\text{nm}. \tag{20}$$

The AFM images in combination with the watershed algorithm yield good results, but the precision is on its limits. The resolution of the AFM is the highest in comparison to all other used methods. However, it does not suffice to quantify a single island with an error below 1.8 nm at island radii for AuPd between 5.8 nm and 6.0 nm. For sure, the error is caused by averaging the mean radius generated by watershed and the mean radius of the manually done measurements, but it is not able to get exact values at this small dimension. For a really precise statement of the island radius, the watershed algorithm is not the best choice, but it is feasible in comparison to other analysis tools. The method would work more accurate if the pixelsize of the AFM measurement was smaller. As mentioned in the introduction of this chapter, distortion effects and hopping of atoms

between scanning tip and object occur if the pixelsize is too small. However, a statistic of more than hundred detected islands was able to be reached for an evaluation of the film quality.

8 DEPENDENCIES OF TARGET MATERIALS

All experiments before were based on the target material AuPd. But not only AuPd leads to a strong textured film under default conditions, target materials like gold (Au), Platinum (Pt) and PtPd show the same behaviour. Therefore, this chapter deals with the creation of thin films made of different materials with a similarly smooth surface based on the newly acquired knowledge about the textured-free film of AuPd.
However, a major point is the behaviour of the mainly used parameter, the argon pressure, depending on the target material. The morphological change by variation of the argon pressure is described in Chapter 5 and it was found out that a textured-free thin film can be generated by $p_{Ar} = 8 \cdot 10^{-3}$mbar, but is not depicted when the ditches disappear. The pressure where the morphology changes from textured to textured-free is defined as critical argon pressure p_{cr}. After finding out this quantity, the film growth of another material will be compared and characterisations of the islands by evaluation of AFM images will be performed to determine island sizes of different materials.

8.1 CRITICAL ARGON PRESSURE

The same method for observing ditches formations is used in Chapter 5. With the HR-SEM the surface of thin films is depicted and compared with different argon pressures. The target materials PtPd, Pt, Au, tungsten (W) and iridium (Ir) are used to evaluate the critical argon pressure depending on the materials. The institute possesses also other materials like chromium (Cr) and aluminium (Al), but the oxidation reactions for these materials are too big to handle the evaluation without vacuum transfer to avoid oxidation effects on the surfaces after the exchange process between sputter coater and HR-SEM.
The starting point of this experiment is that a textured-free film can be generated at $p_{Ar} = 8 \cdot 10^{-3}$ mbar, the ditches begin to close at $p_{Ar} = 1 \cdot 10^{-2}$ mbar shown in Figure 43 for AuPd. Therefore, the pressure starting from $p_{Ar} = 2 \cdot 10^{-2}$ mbar has successively decreased till the ditches are nearly disappeared. If a transition region exists, this region is associated to the textured film.
The ditches-free films cannot be depicted in the HR-SEM. The lateral resolution is not high enough to separate a single island from each other, therefore just HR-SEM images of thin films with ditches are investigated. They are shown in Figure 62 and Figure 63. For AuPd the texture is already well-known. Some other materials which are also depicted in these figures look similar to AuPd, but materials like Au, Pt and W look differently. The major point is that every material can be sputtered by certain parameters which lead to the same effect in which ditches appear, like for AuPd, for instance.
Pt distinguishes strongly from all other materials, the ditches are very long and great terraces has been formed at an argon pressure of $p_{Ar} = 2 \cdot 10^{-2}$ mbar.
W forms ditches just at a higher argon pressure than other materials, these ditches are really short and nearly point-like. With successive decreasing of the pressure the critical argon pressure can be found for each material and is summarised in Table 13.

All denoted values for p_{cr} are around $p_{Ar} \approx 1 \cdot 10^{-2}$ mbar except tungsten. One difference between tungsten and other materials is shown in Chapter 4 where a cross-sectional EDX line scan shows that the amount of build-in oxygen is much higher than for gold.

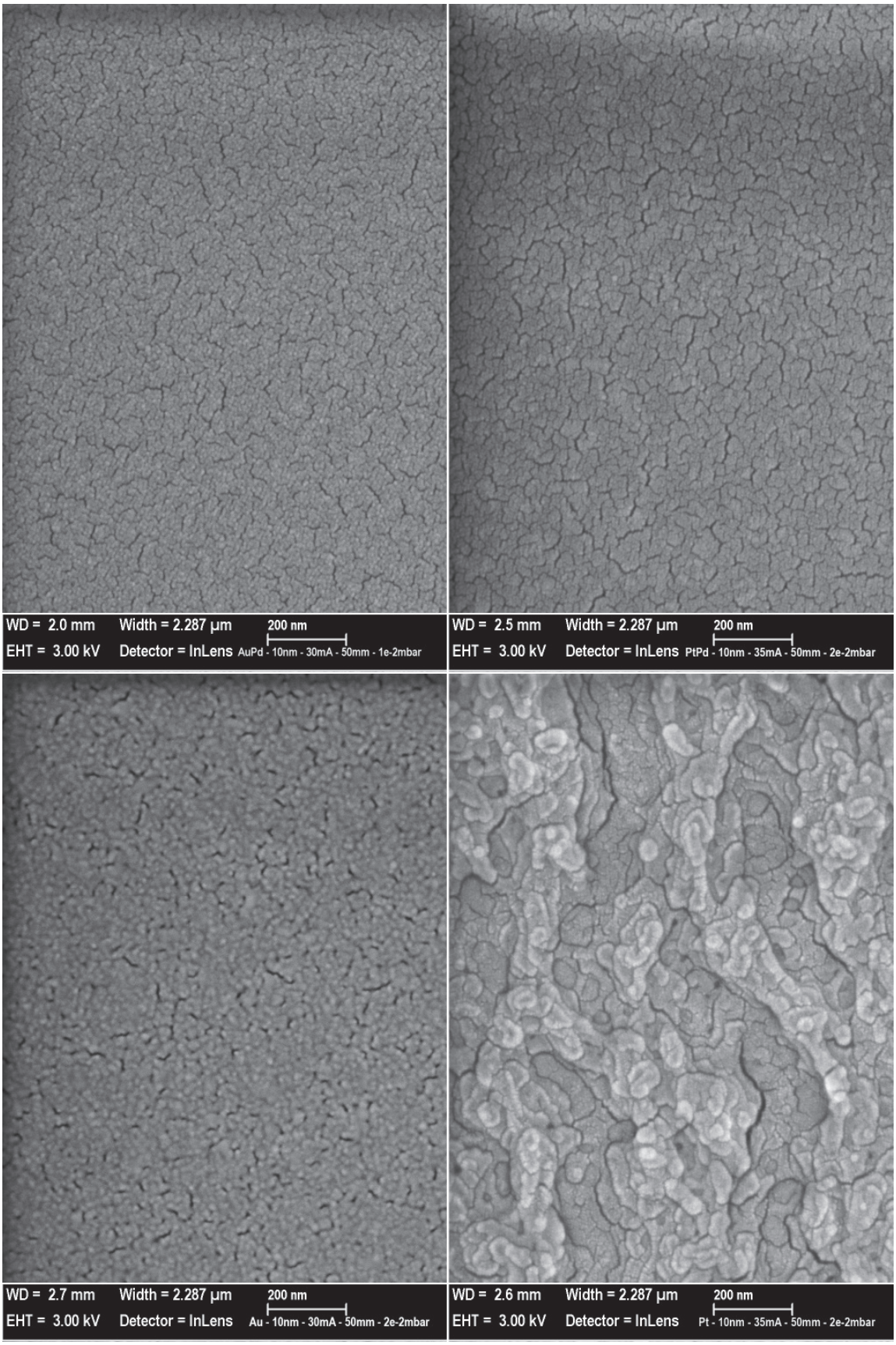

Figure 62: HRSEM image of textured thin film surfaces for different materials. The most important sputter parameters are written in the caption of each HR-SEM measurement.

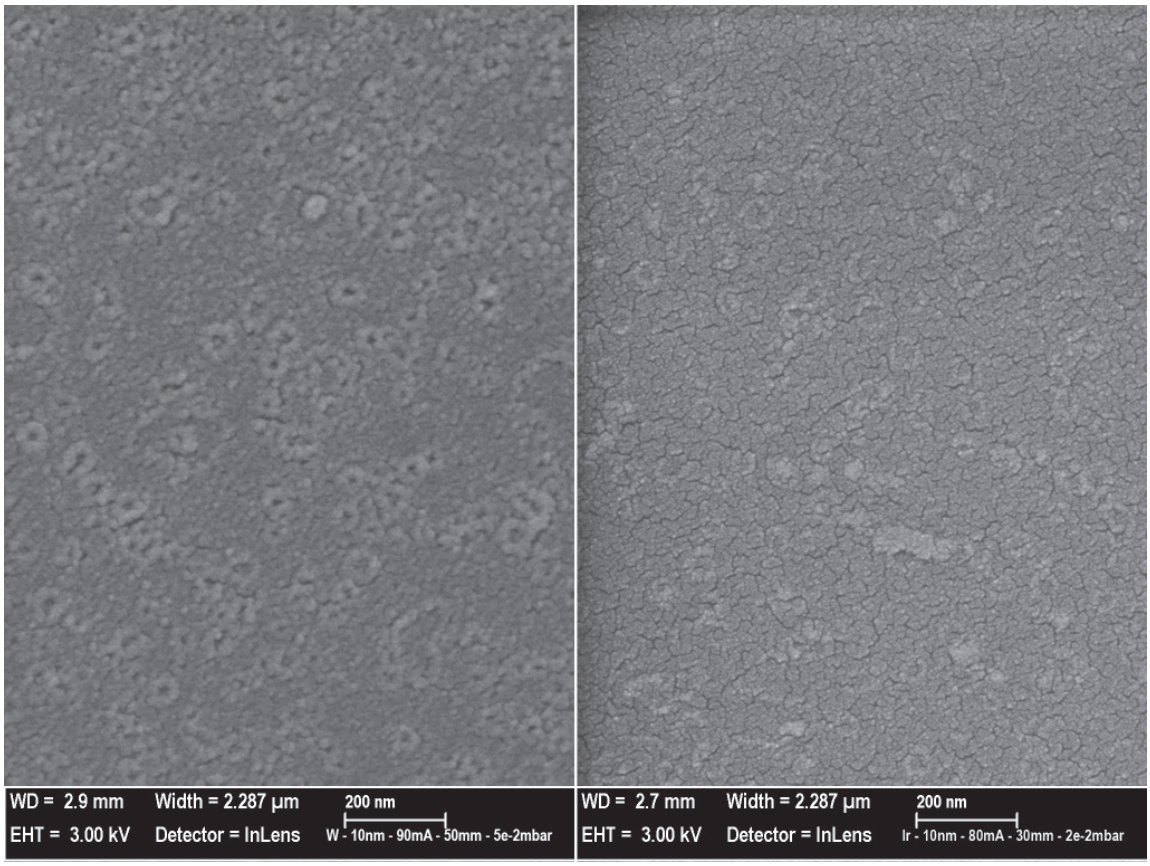

Figure 63: HRSEM image of textured thin film surfaces for different materials. The most important sputter parameters are written in the caption of each HR-SEM measurement.

Table 13: Sputtering parameters and critical argon pressure of different materials

Material	d / nm	$I_{sputter}$ / mA	WD / mm	p_{cr} / mbar
AuPd	10	30	50	$\leqslant 9.6 \cdot 10^{-3}$
PtPd	10	35	50	$\leqslant 1.0 \cdot 10^{-2}$
Au	10	30	50	$\leqslant 9.5 \cdot 10^{-3}$
Pt	10	35	50	$\leqslant 1 \cdot 10^{-2}$
W	10	90	50	$\leqslant 2 \cdot 10^{-2}$
Ir	10	80	30	$\leqslant 1.2 \cdot 10^{-2}$

Probably this is the reason why W has a longer texture-free pressure range than other materials. No other difference could be found during the SEM investigations.

8.2 THIN FILM GROWTH OF IR

Besides studying the effects of parameter variations on the surface of the film, the growth processes are investigated by TEM measurements. The growth process gives indication of the current state of growing adatoms and the resultant film surface. In Chapter 6 the growing metallic film of AuPd was compared with a resultant texture-free parameter setting and a set of parameter which causes a thin film surface with deep ditches. Now, the same comparison for Ir was done and is depicted from Figure 64 to Figure 67.
Ir was chosen because the scientific community prefers it for covering samples with a conductive thin film. The reason for this is that the dimensions of islands are much smaller than for other materials, therefore no relevant height information of the film can be visualised in a HR-SEM, and it does not exist any oxidation effects of the surface. That the islands are smaller can be assumed by looking at the ditches in Figure 63 which occur due to the argon pressure higher or equal to $p_{Ar} = 1.2 \cdot 10^{-2}$ mbar. These ditches are thinner and smaller in size than for AuPd, for instance.
The figures of the TEM measurements show exactly the same behaviour of the growth process by comparing the films between texture-free and textured sputtering at different growth steps as AuPd. The lower argon pressure leads to more nucleation centres with a smaller size of the nucleated adatom-agglomerations. But at both images of Figure 64 the number of islands is higher than at AuPd in Figure 48. In general, that would mean that there does not exist a critical number of nucleation centres per area to create a continuously grown film unless the critical number of nucleation centres would have been a material dependency.

Table 14: Sputtering parameters for investigating the film growth of Ir

sputter current $I_{sputter}$	[mA]	30	working distance WD	[mm]	50
pre-vacuum $p_{pre-vac}$	[mbar]	$8e-5$	sputter-vacuum p_{Ar}	[mbar]	$5e-2, 8e-3$
rotation rot	[-]	3	tilt t	[–]	0
thickness d	[nm]	varies			
substrate material	[–]	silicon	target material	[–]	Ir

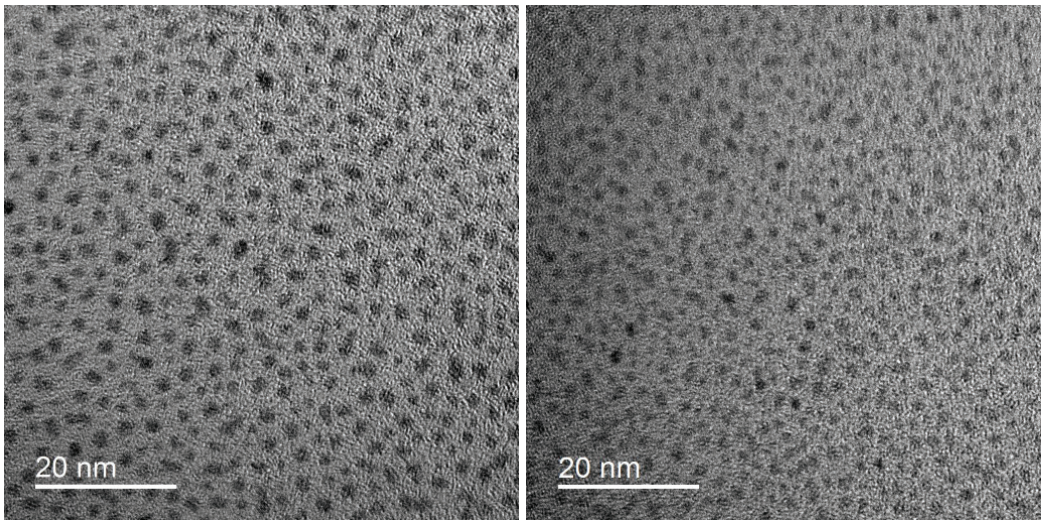

Figure 64: TEM images (bright-field) - Ir films sputtered with $d < 0.25$ nm, $p_{Ar} = 5 \cdot 10^{-2}$ mbar (left) and $p_{Ar} = 8 \cdot 10^{-3}$ mbar (right) on Formvar.

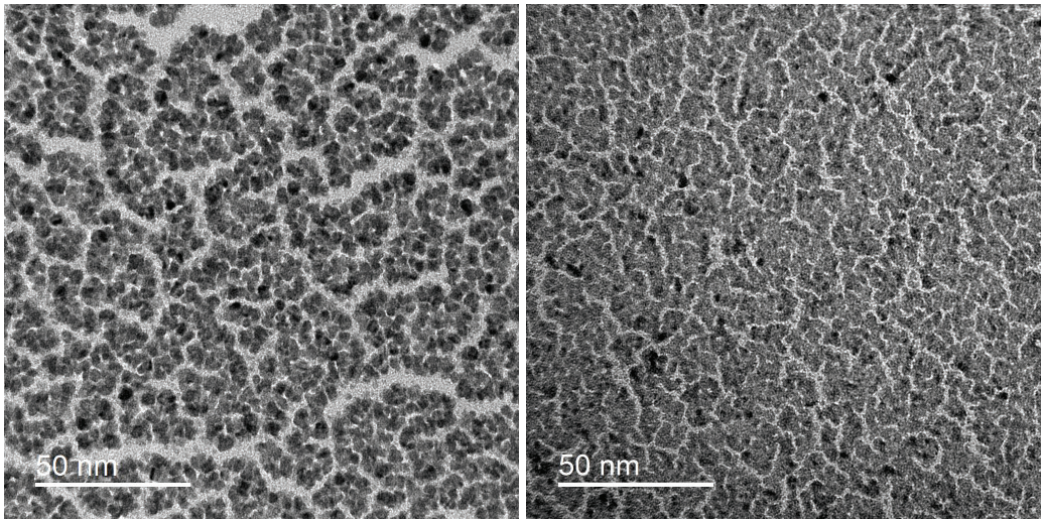

Figure 65: TEM images (bright-field) - Ir films sputtered with $d = 1$ nm, $p_{Ar} = 5 \cdot 10^{-2}$ mbar (left) and $p_{Ar} = 8 \cdot 10^{-3}$ mbar (right) on Formvar.

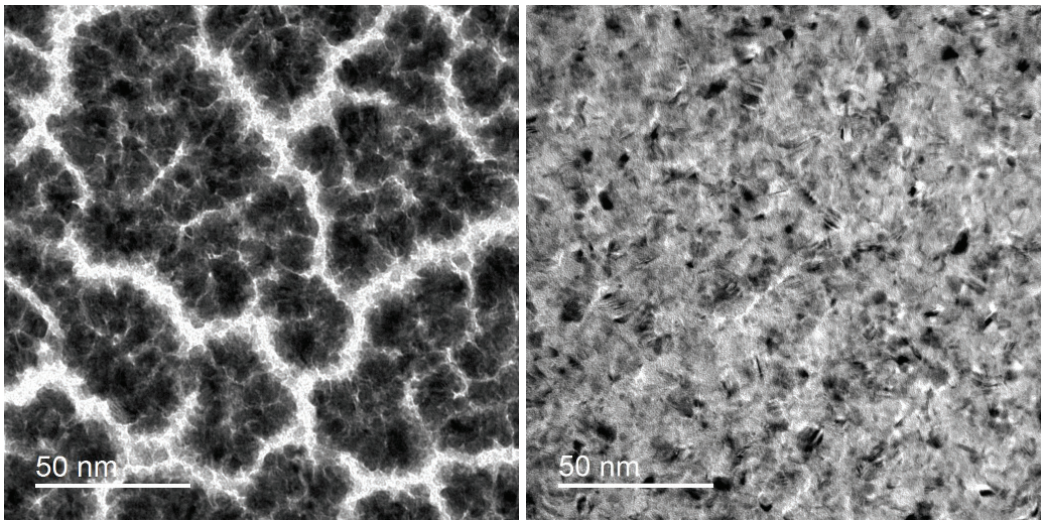

Figure 66: TEM images (bright-field) - Ir films sputtered with $d = 5$ nm, $p_{Ar} = 5 \cdot 10^{-2}$ mbar (left) and $p_{Ar} = 8 \cdot 10^{-3}$ mbar (right) on Formvar.

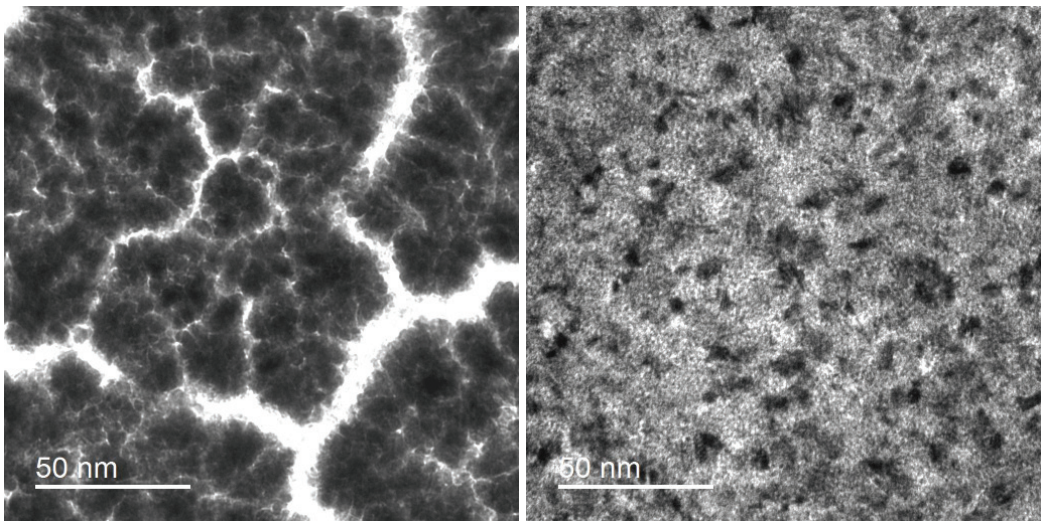

Figure 67: TEM images (bright-field) - Ir films sputtered with $d = 10$ nm, $p_{Ar} = 5 \cdot 10^{-2}$ mbar (left) and $p_{Ar} = 8 \cdot 10^{-3}$ mbar (right) on Formvar.

8.3 CHARACTERISATION OF FILM MADE OF OTHER MATERIALS

Before a precise particle analysis for a film which is made of a different material than AuPd can be done, a study about the general surface behaviours of the materials has to be performed to check the applicability of the used algorithm. Therefore, the first AFM measurements were done by 512 px × 512 px at a scan window of 500 nm × 500 nm. These measurements do not fulfil the recommendations for the watershed algorithm, for instance, but the results show how the last step of the growth mode affects the single islands. The size of these islands has to be analysed. The films are sputtered with their default parameters excepting the argon pressure, which is set to the lower limit of the device for getting a continuously grown metallic film. The surfaces, shown in Figure 68 to Figure 70, of these films distinguish from each other, which makes the decision easier to find the right material for the further analysis procedure.

In general the AFM images show that all films which are made of pure metals seems to have the tendency to grow together, but they do not form strong boundaries between the islands. The pure Au film shows this behaviour clearly. Au forms the biggest islands in comparison to all other films and the surface looks worm-like nucleated islands. A definition of the size of a single island is not possible with the used algorithm.

W and Ir, are also pure metals, but this does not let assume that they have a worm-like surface, too. The reason for that is that the island sizes are much smaller than those of all other materials. The resolution of the AFM is on its limits and the tool is not able to separate two islands from each other, what leads to areas which look blurred and grown together. Especially W causes problems for each measurement tool. The HR-SEM and also TEM are not able to measure a sample which is sputtered with W as high resolved as for other materials. The same phenomena is now shown in the AFM images. Probably the built-in oxygen which is found by the EDX investigation of the FIB lamella leads to such kinds of problems. Therefore, the bondings between the islands are weaker than for other materials which do not build in oxygen atoms. At the AFM a higher mobility of the islands would lead to such effects and could be the reason for the big blurred areas that are shown Figure 69 (left).

Pure Pt is the only exception of the non-alloy materials. It seems that single islands appear and do not form agglomerates of more than one island, like Au. But a precise look at the AFM image in Figure 68 (right) exhibits areas which form chains not as long as Au (with 4 to 5 islands per agglomerate), but also 2 to 3 islands are involved. These chains of islands falsify the result of the particle analysis.

AuPd and PtPd are both materials which are very often used for sputtering non-conductive samples for SEM experiments. Obviously, the fraction of Pd causes islands which grow higher and wider, therefore they form strongly pronounced boundaries between each one.

A solution for the problem of measuring island dimensions for Ir or W would be a more precise measurement with the AFM by using a finer or harder/softer needle tip. The used tip has an diameter of around 5 nm, and is called *Fastscan C* needle with a 300 kHz resonant frequency. C is assigned to a hardness factor. Every material has another behaviour and therefore another type of tips should be used. But this experiment is used for a fast evaluation of the surfaces to analyse the island diameter with the watershed algorithm by existing equipment and measurement configuration.

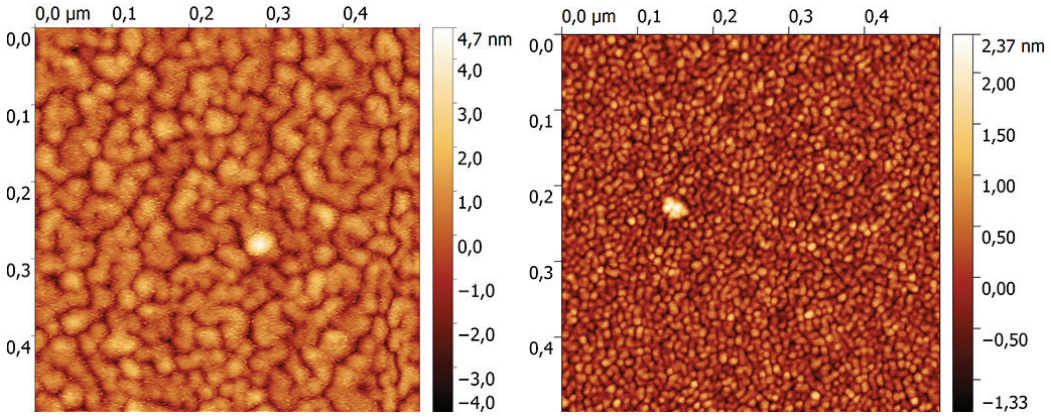

Figure 68: AFM images of a 10-nanometre-thin Au film (left) and Pt (right) sputtered with parameters of Table 13 and an argon pressure of $p_{Ar} = 8 \cdot 10^{-3}$ mbar.

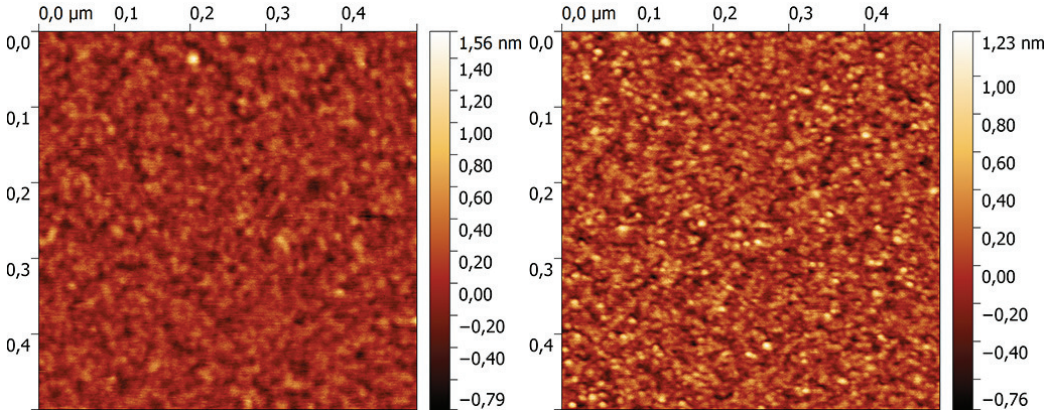

Figure 69: AFM images of a 10-nanometre-thin W film (left) and Ir (right) sputtered with parameters of Table 13 and an argon pressure of $p_{Ar} = 8 \cdot 10^{-3}$ mbar.

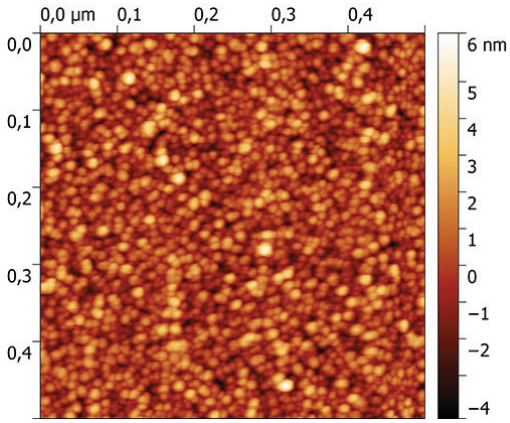

Figure 70: AFM images of a 10-nanometre-thin PtPd sputtered with parameters of Table 13 and an argon pressure of $p_{Ar} = 8 \cdot 10^{-3}$ mbar.

8.3.1 *Further Characterisation of PtPd Film*

More precise characterisation of PtPd is useful, because the comparison to AuPd can be made to check whether the variation of the working distance and the current have as small impact on the dimensions of the islands as AuPd. Another reason is the determination of the island dimensions. As written in the section before other materials are not measurable with the used equipment for getting really precise results.
In the case of AuPd, some tests with parameters of the watershed algorithm had to be made before the particle analysis could start. The optimised parameters are the ones which lead to the maximal detected islands inside a certain range. The first assumption, which is shown in Figure 70, is that the islands of PtPd have nearly a similar size but the height distinguishes between both. Therefore, the size of the droplets keeps still the same and the amount of droplets varies. The resulting values are depicted in Table 15.

Table 15: Parameters of the watershed algorithm for PtPd films

island location	
number of steps	10
drop size	3.71 %
threshold	26 px^2
separation	
number of steps	400
drop size	3.71 %

The procedure for the particle analysis for PtPd is equal to the analysis of AuPd. Therefore, three radii and the height values were evaluated and compared to get an idea how the shape of the particle is distributed. Additionally, the island radius is also measured manually. The next step is to find a statistically significant tendency of the radii in respect of the working distance or the current, if a certain tendency exists, which is associated with the applied voltage between substrate and target. If there are no tendencies between the dimensions of the islands and the mentioned sputter parameters, the data is used to express the mean radius and the mean height of the island over all collected datasets.
The working distance is increased from $WD = 30\,\text{mm}$ to $WD = 90\,\text{mm}$ in five steps and the particle analysis of the results is shown in Table 16.

The result is a bit surprising, a precise look of all values by increasing the working distance lets assume that there could be a certain tendency, at the evaluation by watershed. For instance, the difference of the values of the mean radius between both extrema at $WD = 30\,\text{mm}$ and $WD = 90\,\text{mm}$ is near 1 nm and falls continuously. The watershed algorithm for this kind of material works better, although all dimensions of the islands including radius and height are smaller than for AuPd. During the particle analysis with the watershed algorithm a better separation of islands was noted and a quite good statistic of detected islands was reached.
The ratios between each type of radius are also similar to those of AuPd. This means that the form of an island does not vary a lot, what is in agreement with the observation of the PtPd surface by the human eyes. To compare the deformation of the island by varying the distance of the sample to the target, the average value of all three radii $\bar{r}$ is taken because the real island radius has to lie anywhere in between. Of course, the error which occurs through the arithmetic operation is around 1.4 nm, but the shapes of the islands are also not constant. Besides the irregular form of the islands, an error of the measurement method has to be also considered and is included in this quantity. However, the analysis method and also the measurement technique are on their possible

Table 16: Resulting island dimensions of a continuously grown PtPd film by variation of the working distance

current	35 mA	argon pressure	$8e-3$ mbar	thickness 10 nm
WD / mm	$r_{mean,\,wat}$ / nm	$r_{min,\,circ}$ / nm	$r_{max,\,insc}$	$r_{mean,man} \pm \Delta r$ / nm
30	5.9	8.0	3.9	4.6 ± 1.6
45	5.4	7.3	3.7	4.4 ± 1.2
60	5.2	7.1	3.6	4.4 ± 1.3
75	5.0	6.7	3.4	4.1 ± 1.5
90	5.1	7.1	3.3	4.4 ± 1.5
WD / mm	$R_a \pm \Delta R_a$ / nm	$R_Z \pm \Delta R_Z$ / nm		
30	0.17 ± 0.02	0.9 ± 0.1		
45	0.21 ± 0.02	1.1 ± 0.1		
60	0.22 ± 0.03	1.1 ± 0.1		
75	0.22 ± 0.02	1.2 ± 0.1		
90	0.22 ± 0.02	1.2 ± 0.1		
		$\bar{r}_{mean,\,wat}$	(5.4 ± 0.4) nm	
		$\bar{r}_{mean,\,man}$	(4.4 ± 1.4) nm	
		$R_{a,mean}$	(0.21 ± 0.02) nm	
		$R_{Z,mean}$	(1.1 ± 0.1) nm	

limits and a variation of the radius which is less than 1 nm can not be determined precisely to specify a radius per working distance with an error less than a half nanometre, which corresponds to the length of one pixel. Out of the particle analysis by watershed, a certain tendency can be determined, even if the error is quite big, but the measurements of the island radius which are done manually, do not confirm this behaviour. Dimensions of about 1 nm would also observable by manual measurements.

The comparison between AuPd (blue graph) and PtPd (green graph), which island sizes are evaluated by watershed and manually, is shown in Figure 71. The increasing of the working distance shows that there could be a tendency. But due to the fact that the error is much higher than the less pronounced negative slope, the resulting data is used to express an averaged mean radius of the islands for PtPd.

Besides the evaluation of the island radius, the comparison between the evolution of the height by variation of the WD seems to be quite constant and no tendency can be observed.

In summary, PtPd forms smaller islands as AuPd and the influence of the working distance looks like the same.

Exactly the same experiment was performed for a PtPd film by variation of the sputter current. The compared values are shown in Figure 72. The data of the PtPd film is depicted in Table 17.

During the particle analysis two datasets are noticed through a worse amount of detected islands than during the other AFM images, especially the data of $I = 90$ mA for the values of $I = 115$ mA for PtPd. They rapidly fall down of around 1 nanometre is probably caused from bad statistics and should not be identified as a significant change of the island radius.

First of all, the comparison of the results seems to be a slightly increasing behaviour of the island radius by increasing the current (evaluated by watershed) for a continuously grown AuPd film, whereas the behaviour of the island height is quite constant independent from the sputtering material. But this behaviour could not be detected by the

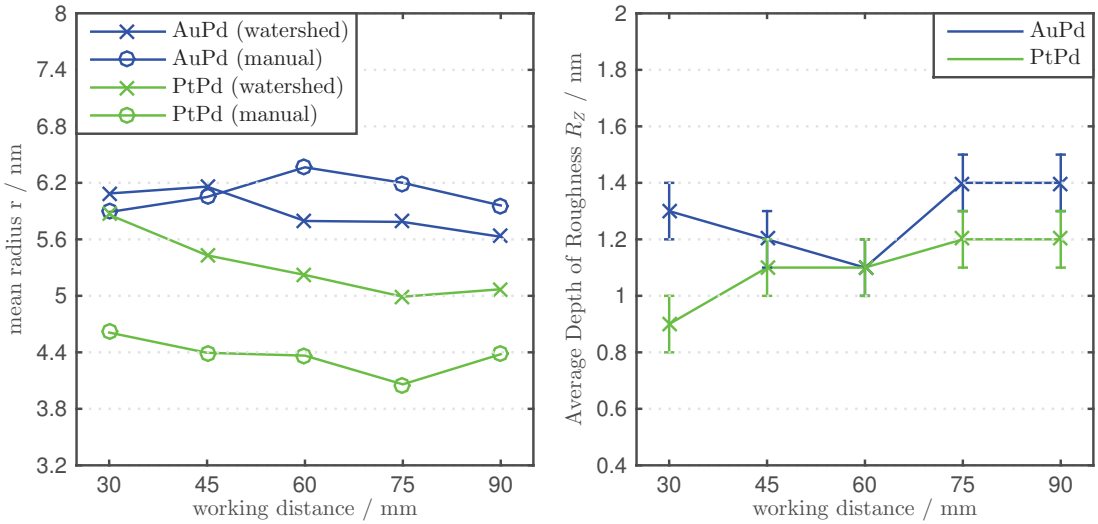

Figure 71: Results, shown in graphs, of the particle analysis of AuPd (values from Table 11) and PtPd. The left graph shows the comparison between the mean radius of the islands and the right graph depicts the height distribution. The error for the determination of the mean radius by watershed is estimated with 1 pixel and corresponds to $\Delta r_{mean,wat} = 0.5\,nm$, the error of the manual measurement is $\Delta r_{mean,man} = 1.7\,nm$. Furthermore the error of the height is estimated with $\Delta R_{Z,AuPd} = 10\,\%$, which is in accordance to the calibration error of the height detection of the AFM and the error of roughness measurement.

Table 17: Resulting island dimensions of a continuously grown PtPd film by variation of the current

Working distance	50 mm	argon pressure	$8e-3$ mbar	thickness 10 nm
I / mA	$r_{mean,\,wat}$ / nm	$r_{min,\,circ}$ / nm	$r_{max,\,insc}$	$r_{mean,man} \pm \Delta r$ / nm
15	6.5	9.5	3.9	5.2 ± 1.5
40	6.2	9.2	3.7	5.5 ± 1.6
65	6.4	9.0	3.6	5.1 ± 1.7
90	5.3	7.6	3.4	5.3 ± 1.6
115	5.8	8.2	3.3	5.5 ± 1.5
I / mA	$R_a \pm \Delta R_a$ / nm	$R_Z \pm \Delta R_Z$ / nm		
15	0.16 ± 0.03	0.7 ± 0.1		
40	0.14 ± 0.02	0.7 ± 0.1		
65	0.15 ± 0.02	0.7 ± 0.1		
90	0.16 ± 0.02	0.8 ± 0.1		
115	0.16 ± 0.02	0.8 ± 0.1		
		$\bar{r}_{mean,\,wat}$	$(6.1 \pm 0.5)\,nm$	
		$\bar{r}_{mean,\,man}$	$(5.3 \pm 1.6)\,nm$	
		$R_{a,mean}$	$(0.15 \pm 0.02)\,nm$	
		$R_{Z,mean}$	$(0.7 \pm 0.1)\,nm$	

manual measurements.
As written before, the interpretation of data with such kind of errors is more or less a hypothesis than an exact physical observation, therefore the data is used to express

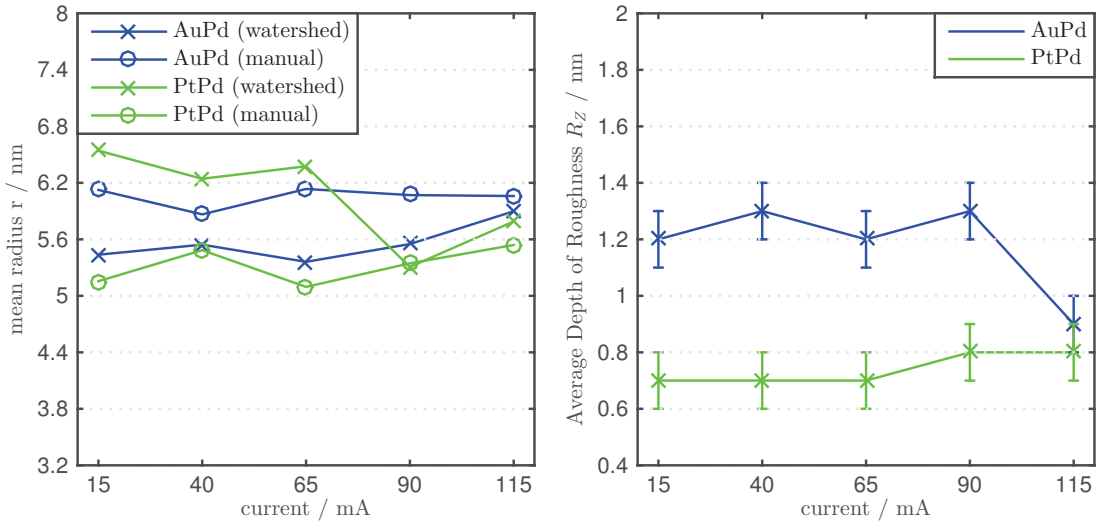

Figure 72: Results, shown in graphs, of the particle analysis of AuPd (values from Table 12) and PtPd. The left graph shows the comparison between the mean radius of the islands and at the right graph depicts the height distribution. The error for the determination of the mean radius by watershed is estimated with 1 pixel and corresponds to $\Delta r_{mean,wat} = 0.5\,nm$, the error of the manual measurement is $\Delta r_{mean,man} = 1.6\,nm$. Furthermore the error of the height is estimated with $\Delta R_{Z,AuPd} = 10\,\%$, which is in accordance to the calibration error of the height detection of the AFM and the error of roughness measurement.

an averaged island size, again. The averaged mean values by variation of the working distance for PtPd amounts to

$$\bar{r}_{mean,\,PtPd} = (4.9 \pm 1.5)\,nm \text{ and } R_{Z,mean,\,PtPd} = (1.1 \pm 0.1)\,nm\,, \tag{21}$$

and the mean values for the variation of the current are

$$\bar{r}_{mean,\,PtPd} = (5.7 \pm 1.6)\,nm \text{ and } R_{Z,mean,\,PtPd} = (0.7 \pm 0.1)\,nm. \tag{22}$$

Table 18: Overview of all mean island radii and mean height from different materials

Material	$r_{mean,\,man}$ / nm	$R_a \pm \Delta R_a$ / nm	$R_Z \pm \Delta R_Z$ / nm
Au	13.5	0.74 ± 0.08	3.7 ± 0.4
W	8.3	0.14 ± 0.03	0.7 ± 0.1
Pt	5.9	0.37 ± 0.07	1.6 ± 0.1
AuPd	5.7	0.24 ± 0.03	1.3 ± 0.1
PtPd	5.3	0.18 ± 0.02	0.9 ± 0.1
Ir	4.2	0.20 ± 0.04	0.7 ± 0.1

A further point of the limits of this method has to be noticed, too. The detection of the particles works quite good, when the AFM topography leads to an adequate quality of the image. No effect of the sputter parameters current and working distance could be identified to a change of the island dimensions. Probably this parameters would have an effect, but it was not measurable with the present methods. Nevertheless, manual measurements of the island radius were performed for all other targets except chromium and

aluminium and also height distribution of this materials was done to get a ranking of the material sorted by the island radius. The values are depicted in Table 18. The comparison shows that the materials with the smallest radii are PtPd and Ir. From iridium is known that the islands are very small, but it is a surprise that PtPd forms islands with similar dimensions. Besides the evaluation of the radii, the height of these islands plays an important role, especially at applications of such thin film for HR-SEM. The topographical image of a surface depends on the height distribution strongly. Therefore, the best material for HR-SEM is iridium, because it forms islands with very small heights and the radii.

Part III

CONCLUSION

9

IMPROVING OF THE SURFACE OF METALLIC THIN FILMS BY REDUCING MICRO-STRUCTURES

The starting situations showed a highly structured metallic thin film with deep ditches generated by a DC magnetron sputter coater. A systematic variation of single parameter leads to a big improvement of the film surface. The leading parameter which causes the main improvement is the argon pressure inside the chamber of the sputter coater. A low argon atmosphere, lower than $1 \cdot 10^{-2}$ mbar, leads to a surface which is completely free of ditches. The critical argon pressure is almost material independent - the only exception forms tungsten, which has a critical argon pressure of $2 \cdot 10^{-2}$ mbar. But this deviation can be neglected due to the fact that the error of the pressure measuring unit is around 30 %.

There are two explanations why the low argon pressure leads to this result. First, a low argon pressure reduces the thermalisation process of the ejected target atom from the solid material to the sample surface. These lower number of argon atoms leads to less collisions with the target atoms which means that the kinetic energy of the target atoms cannot be transferred to other particles. The atom of the target material impinges the surface with much more energy as it would have at a higher argon pressure. Besides dependencies of temperature, diffusion processes are also correlated to the energies of the particles. And if the energy of the particles is high enough, a three dimensional diffusion is possible. The barrier which has to be achieved to move outside of a plain is called Ehrlich-Schwoebel-barrier [13] and would explain why adatoms cannot be found in ditches during the film growth investigations of Chapter 6 sputtered at high argon pressure.

Besides the transfer of energy to the argon atoms, less collisions also lead to a less scattering angle. This causes a highly directed flow of target atoms down to the substrate. Figure Figure 73 (left) shows the TEM image of a thin AuPd film which is sputtered by default conditions.

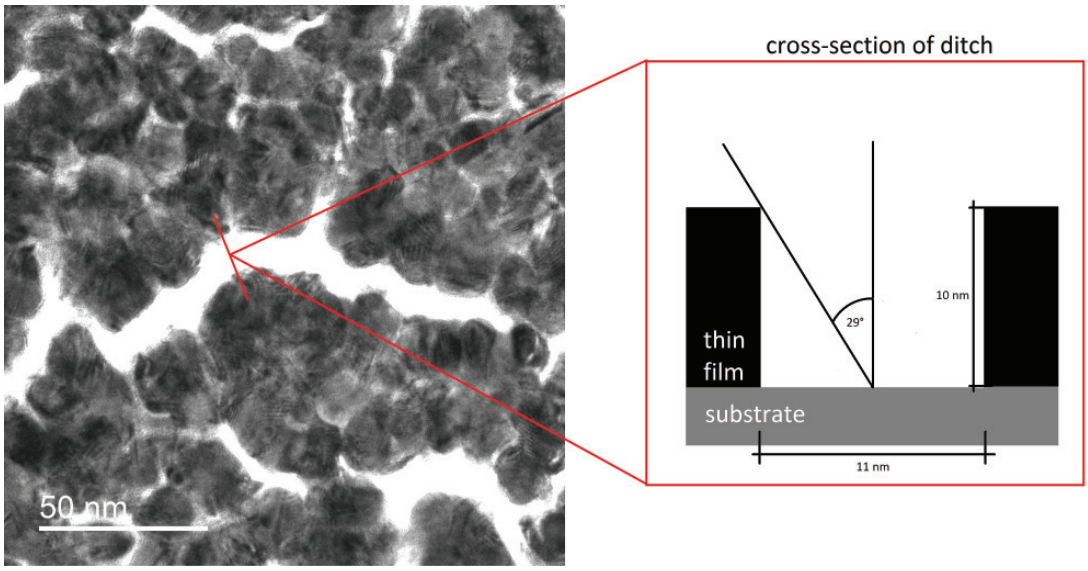

Figure 73: TEM image of Chapter 6 where the film growth was observed (left) and a cross-section of the ditches where the critical half angle is depicted (right)

No clusters of adatoms could be found inside the ditch, which depth is approximately the thickness of the film because the TEM investigations showed that ditches appear from the beginning of the film growth. Simple trigonometry calculation shows that a certain angle is necessary for getting target atoms inside the ditch, which is shown in Figure 73 (right). Therefore, diffusively moving target atoms exceed this angle and the ditches cannot be closed. Otherwise, atoms which move in straight trajectories to the sample can arrive the bottom of the ditch easier.
Both theories are plausible and probably both effects affect the resulting thin film surface, but it was not possible to prefer one of these.
Out of all information which were collected in the experiments within this thesis, an optimised set of parameters for the sputter coater can be found to produce a smooth and featureless surface for high resolution scanning electron microscopy depending on the type of the sample. AFM investigations in Chapter 7 and Chapter 8 show the mean island radius and the mean height of two different materials AuPd and PtPd.

$$r_{mean,AuPd} = (5.7 \pm 1.5)\,\text{nm},\ R_{Z,mean,AuPd} = (1.3 \pm 0.1)\,\text{nm} \tag{23}$$

$$r_{mean,PtPd} = (5.3 \pm 1.5)\,\text{nm},\ R_{Z,mean,PtPd} = (0.9 \pm 0.1)\,\text{nm} \tag{24}$$

The values are calculated from the average of all collected data got from the AFM images. The quantification of the islands was done by the watershed algorithm which is obviously on its limits. Additionally, manual measurements of islands were performed to check the correctness of the data. An error of 0.5 nm by watershed is the accuracy of measuring a single radius and is assigned to the size of one pixel. But a greater error of 1.5 nm is estimated to include small distortion of the islands during the measurement and the detection of clustered islands.
A such small distortion cannot be identified by the human eyes, just the 2D-ACF in Figure 60 lets assume, that the measurements underlie a very small drift. The separation of a single island is quite difficult for the method by this pixelsize of 0.5 nm, but lower pixelsizes are not applicable due to the increasing drift effects during the scan. Therefore, no certain tendency could be found. The influence of the working distance and the current is depicted in Figure 71 and Figure 72 for two different materials.
The watershed algorithm was not applicable to the other materials, therefore the island dimensions are measured manually and tabulated in Table 18. Besides the island radius, the height information is of special interest, too, because the topographical contrast of the SEM depends mainly on the height distribution of the observed surface.
Hence, the best material for SEM is the one with the lowest island radius and the lowest height to get a thin film which structure does not influence the topography of the sample. This film is just responsible for preventing the charging effect by making the sample conductive and for generation of secondary electrons, especially for surface investigation by HR-SEM.
Besides decreasing the argon pressure, Figure 71 and Figure 72 show that the island size is not affected by the current and the working distance. Therefore to minimise the structure, another material has to be chosen. Out of the island dimensions which are tabulated in Table 18 for each material, the best material for HR-SEM is iridium because it has the smallest island size and also a very low mean value of the island height, which corresponds to the smoothest surface which is obtainable. Chromium and aluminium are not verified because these materials are very sensitive for oxidations. Therefore, no precise measurements were possible without vacuum, especially during the AFM measurements.

Now, the optimal sputter settings can be generated due to all informations of this work. The recommended settings for featureless thin films are tabulated in Table 19.

Table 19: Optimised sputter parameter of thin films for HR-SEM

Material	p_{Ar} / mbar	WD / mm	I / mA
Au	$< 1 \cdot 10^{-2}$	$30 - 100$	$\geqslant 15$
Pt	$< 1 \cdot 10^{-2}$	$30 - 100$	$\geqslant 15$
AuPd	$< 1 \cdot 10^{-2}$	$30 - 100$	$\geqslant 15$
PtPd	$< 1 \cdot 10^{-2}$	$30 - 100$	$\geqslant 15$
Ir	$< 1 \cdot 10^{-2}$	$30 - 100$	$\geqslant 80$
W	$< 1 \cdot 10^{-2}$	$30 - 100$	$\geqslant 90$
Al	$< 1 \cdot 10^{-2}$	$30 - 100$	$\geqslant 100$
Cr	$< 1 \cdot 10^{-2}$	$30 - 100$	$\geqslant 110$

The argon pressure has to be lower than the critical argon pressure of $p_{cr} = 1 \cdot 10^{-2}$ mbar, the working distance depends on the sample and the current is specific for the used material. Especially, the working distance depends on the temperature impact on the sample. In Chapter 4 it is shown that the working distance has the most influence of the temperature impact on the sample. Therefore, big working distances have to be used for highly temperature-sensitive samples. If the temperature impact is not important, low working distances can be used. This increases the sputtering rate slightly. But if the time of the sputter process is of special interest, the sputter current has to be varied. The current increases the sputtering rate drastically. A too low adjusted sputtering

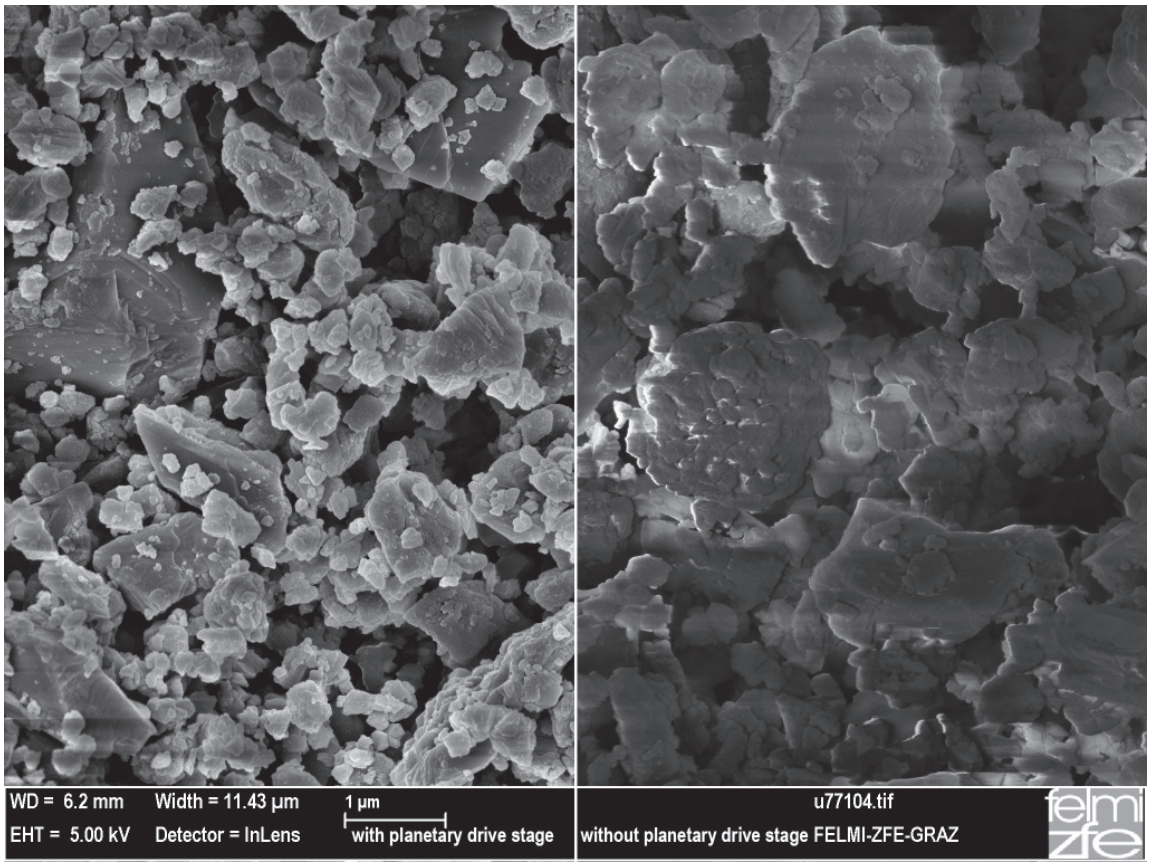

Figure 74: HR-SEM image of a highly structured sample (calcium carbonate) sputtered with planetary drive stage (left) and without planetary drive stage (right).

current leads to an unstable sputter process, due the secondary electron emission and also the target emission depend on the binding energy of the surface atoms of the target material. If the sputtering current is higher than the minimal current which is depicted in Table 19 the resulting plasma is stabilised during the whole sputter process. The sputter current cannot be increased to its upper limits because it influences the temperature impact on the surface of the sample and the temperature at the target material increases, too.

As written before, the argon pressure leads to a higher directed trajectory of the target atoms. This causes a continuously grown metallic film, but if a highly structured sample has to be sputtered, the film does not get homogeneously distributed along the whole film surface. An example is shown in Figure 74. A sample of calcium carbonate is sputtered by a 10-nanometre-thin film of AuPd, with the recommended parameters of Table 19. Due to the low argon pressure and the resulting low scattering angle of the target atoms, charging artefacts occur during the investigations by HR-SEM (Figure 74 (right)). Especially, the In-Lens detector is used to be sensitive for charging artefacts. To prevent this effect, the thin film is sputtered with a planetary drive stage. Besides the rotation around its own centre, this stage consists of six smaller stages, which are called planets, and rotate around their own centres, but in the reverse direction. In Figure 74 (left) the same material is sputtered by this stage where the additional rotational movements increase the homogeneously coverage of the surface to reach also a higher conductivity and a decreasing of the charging effects occurs. Therefore, also highly structured samples can be sputtered by the Leica DC magnetron sputter coater and can be used for HR-SEM.

BIBLIOGRAPHY

[1] Ayache, Jeanne: *Sample preparation handbook for transmission electron microscopy techniques*. New York : Springer, 2010. – ISBN 9781441959744

[2] Bauer, E.: Phaenomenologische Theorie der Kristallabscheidung an Oberflaechen. I. In: *Zeitschrift fur Kristallographie* 110 (1958), S. 372–394. http://dx.doi.org/10.1524/zkri.1958.110.1-6.372. – DOI 10.1524/zkri.1958.110.1–6.372

[3] Belaid, Lamia J. ; Mourou, Walid: Image Segmentation: A watershed transformation algorithm. In: *Image Analysis and Stereology* 28 (2011), Nr. 2, 93-102. http://www.ias-iss.org/ojs/IAS/article/view/852. – ISSN 1854–5165

[4] Chu, Jinn P. ; Jang, J.S.C. ; Huang, J.C. ; Chou, H.S. ; Yang, Y. ; Ye, J.C. ; Wang, Y.C. ; Lee, J.W. ; Liu, F.X. ; Liaw, P.K. ; Chen, Y.C. ; Lee, C.M. ; Li, C.L. ; Rullyani, Cut: Thin film metallic glasses: Unique properties and potential applications. In: *Thin Solid Films* 520 (2012), Nr. 16, 5097 - 5122. http://dx.doi.org/10.1016/j.tsf.2012.03.092. – DOI 10.1016/j.tsf.2012.03.092

[5] Eisenmenger-Sittner, Christoph: Physik und Technologie duenner Schichten / Institut fuer Festkoerperphysik, TU Wien. Wiedner Hautstrasse 8-10, A-1040 Wien, WS 2006 (LVA 133.463). – Vorlesungsskript

[6] Elson, J. M. ; Bennett, Jean M.: Calculation of the power spectral density from surface profile data. In: *Appl. Opt.* 34 (1995), Jan, Nr. 1, 201–208. http://dx.doi.org/10.1364/AO.34.000201. – DOI 10.1364/AO.34.000201

[7] Fekete, L ; Kusova, K ; Petrak, V ; Kratochvilova, I: AFM topographies of densely packed nanoparticles: a quick way to determine the lateral size distribution by autocorrelation function analysis. In: *Journal of Nanoparticle Research* 14 (2012), Nr. 8, S. 1–10

[8] Garcia, Ricardo: *Amplitude Modulation Atomic Force Microscopy*. Weinheim : Wiley-VCH, 2011. – ISBN 978–3–527–64394–3

[9] Gavrila, R ; Dinescu, A ; Mardare, D: A power spectral density study of thin films morphology based on AFM profiling. In: *Raman J Inf Sci Technol* 10 (2007), S. 291–300

[10] Goehlich, A. ; Gillmann, D. ; Doebele, H.F.: Angular resolved energy distributions of sputtered atoms at low bombarding energy. In: *Nuclear Instruments and Methods in Physics Research Section B: Beam Interactions with Materials and Atoms* 164-165 (2000), Nr. 0, 834 - 839. http://dx.doi.org/10.1016/S0168-583X(99)01106-4. – DOI 10.1016/S0168–583X(99)01106–4. – ISSN 0168–583X

[11] Goldstein, Joseph: *Scanning electron microscopy and x-ray microanalysis*. New York : Kluwer Academic/Plenum Publishers, 2003. – ISBN 0306472929

[12] Hoogvliet, J.C. ; Bennekom, W.P. van: Gold thin-film electrodes: an EQCM study of the influence of chromium and titanium adhesion layers on the response. In: *Electrochimica Acta* 47 (2001), Nr. 4, 599 - 611. http://dx.doi.org/10.1016/S0013-4686(01)00793-9. – DOI 10.1016/S0013–4686(01)00793–9. – ISSN 0013–4686

[13] Johansen, Christopher G. ; Huang, Hanchen ; Lu, Toh-Ming: Effects of three-dimensional Ehrlich-Schwoebel barrier on texture selection during Cu nanorod growth. In: *Applied Physics Letters* 91 (2007), Nr. 12, -. http://dx.doi.org/10.1063/1.2771525. – DOI 10.1063/1.2771525

[14] Kelly, P.J ; Arnell, R.D: Magnetron sputtering: a review of recent developments and applications. In: *Vacuum* 56 (2000), Nr. 3, 159 - 172. http://dx.doi.org/10.1016/S0042-207X(99)00189-X. – DOI 10.1016/S0042–207X(99)00189–X. – ISSN 0042–207X

[15] Lieberman, M. A.: *Principles of plasma discharges and materials processing*. Hoboken, N.J : Wiley-Interscience, 2005. – ISBN 0471720011

[16] Mahan, John: *Physical vapor deposition of thin films*. New York : Wiley, 2000. – ISBN 0471330019

[17] National Institutes of Health in Maryland, US: *ImageJ v1.48 (Image Processing And Analysis in Java)*. http://imagej.nih.gov/ij/index.html. Version: February 2015

[18] Pfeiffer Vacuum GesmbH: *Data sheet of Pfeiffer PKR 251 Compact Full-Range Gauge*. http://www.pfeiffer-vacuum.com/productPdfs/PTR26001.de.pdf. Version: February 2015

[19] Pfeiffer Vacuum GesmbH: *Operating Instructions of Pfeiffer PKR 251 Compact FullRange Gauge*. http://www.idealvac.com/files/brochures/Pfeiffer_PKR_251_Pirani_ColdCathode.pdf. Version: February 2015

[20] McCracken, G M.: The behaviour of surfaces under ion bombardment. In: *Reports on Progress in Physics* 38 (1975), Nr. 2, 241. http://stacks.iop.org/0034-4885/38/i=2/a=002

[21] Meyer, Kevin ; Schuller, Ivan K. ; Falco, Charles M.: Thermalization of sputtered atoms. In: *Journal of Applied Physics* 52 (1981), Nr. 9, 5803-5805. http://dx.doi.org/10.1063/1.329473. – DOI 10.1063/1.329473

[22] Neger, Theo: Experimentelle Plasmaphysik / Institut fuer Experimentalphysik, TU Graz. Petersgasse 16, A-8010 Graz, WS 2013/2014 (LV 511.123). – Vorlesungsskript

[23] Orloff, Jon: *High Resolution Focused Ion Beams: FIB and its Applications the Physics of Liquid Metal Ion Sources and Ion Optics and Their Application to Focused Ion Beam Technology*. Boston, MA : Springer US Imprint Springer, 2003. – ISBN 978–1–4615–0765–9

[24] Petr Klapetek, Christopher A. David Necas N. David Necas: *Gwyddion user guide: Chapter 4. Data Processing and Analysis (Grain Analysis)*. http://gwyddion.net/documentation/user-guide-en/grain-analysis.html. Version: January 2015

[25] Petr Klapetek, David N.: *Gwyddion v2.40 (free AFM data analysis software)*. http://gwyddion.net. Version: February 2015

[26] Senthilkumar, M. ; Sahoo, N.K. ; Thakur, S. ; Tokas, R.B.: Characterization of microroughness parameters in gadolinium oxide thin films: A study based on extended power spectral density analyses. In: *Applied Surface Science* 252 (2005), Nr. 5, 1608 - 1619. http://dx.doi.org/10.1016/j.apsusc.2005.02.122. – DOI 10.1016/j.apsusc.2005.02.122. – ISSN 0169–4332

[27] Slavcheva, E. ; Ganske, G. ; Topalov, G. ; Mokwa, W. ; Schnakenberg, U.: Effect of sputtering parameters on surface morphology and catalytic efficiency of thin platinum films. In: *Applied Surface Science* 255 (2009), Nr. 13, 6479-6486. http://dx.doi.org/10.1016/j.apsusc.2009.02.033. – DOI 10.1016/j.apsusc.2009.02.033

[28] Smith, Henry I. ; Flanders, D. C.: Oriented crystal growth on amorphous substrates using artificial surface relief gratings. In: *Applied Physics Letters* 32 (1978), Nr. 6, 349-350. http://dx.doi.org/10.1063/1.90054. – DOI 10.1063/1.90054

[29] Stuart, R. V. ; Wehner, G. K.: Energy Distribution of Sputtered Cu Atoms. In: *Journal of Applied Physics* 35 (1964), Nr. 6, 1819-1824. http://dx.doi.org/10.1063/1.1713748. – DOI 10.1063/1.1713748

[30] Thornton, John A.: Magnetron sputtering: basic physics and application to cylindrical magnetrons. In: *Journal of Vacuum Science and Technology* 15 (1978), Nr. 2, 171-177. http://dx.doi.org/10.1116/1.569448. – DOI 10.1116/1.569448

[31] Torquato, S. ; Stell, G.: Microstructure of two phase random media. I. The n point probability functions. In: *The Journal of Chemical Physics* 77 (1982), Nr. 4, 2071-2077. http://dx.doi.org/10.1063/1.444011. – DOI 10.1063/1.444011

[32] Venables, John: *Introduction to surface and thin film processes*. Cambridge, UK New York : Cambridge University Press, 2000. – ISBN 9780521785006

[33] Wei, Helin ; Liu, Zuli ; Yao, Kailun: The influence of the incidence energy of deposited particles on the growth morphology of thin films. In: *Vacuum* 57 (2000), Nr. 1, 87 - 97. http://dx.doi.org/10.1016/S0042-207X(00)00112-3. – DOI 10.1016/S0042–207X(00)00112–3. – ISSN 0042–207X

[34] Williams, David: *Transmission electron microscopy a textbook for materials science*. New York : Springer, 2009. – ISBN 038776500X